

⑨ Semi-Annual technical rep't. no. 3 1 Nov 75-30 Apr 76  
11735

UNCLASSIFIED

SECURITY CLASSIFICATION OF THIS PAGE (When Data Entered)

REPORT DOCUMENTATION PAGE		READ INSTRUCTIONS BEFORE COMPLETING FORM
1. REPORT NUMBER	2. GOVT ACCESSION NO.	3. RECIPIENT'S CATALOG NUMBER
Semi-Annual Technical Report No.3		AD-A103 410
4. TITLE (and Subtitle) Earthquake Characteristics and Earthquake- Explosion Discrimination		5. TYPE OF REPORT & PERIOD COVERED 1 Nov 1975 - 30 Apr 1976
6. AUTHOR Carl L. Kisslinger, E. R. Engdahl, P. Luh, M. L. Smith W. Gauthrop, T. Hewitt, G. Lundquist R. Herrmann		7. PERFORMING ORG. REPORT NUMBER
8. CONTRACT OR GRANT NUMBER(s) AFOSR-75-2775 ARPA Order-1827		9. PERFORMING ORGANIZATION NAME AND ADDRESS CIRES University of Colorado Boulder, Colorado, 80309
10. CONTROLLING OFFICE NAME AND ADDRESS Advanced Research Projects Agency/NMR 1400 Wilson Boulevard Arlington, VA 22209		11. PROGRAM ELEMENT, PROJECT, TASK AREA & WORK UNIT NUMBERS ARPA Order-1827 Program Code 5F10 Program Element 62701E
12. MONITORING AGENCY NAME & ADDRESS (if different from Controlling Office) Air Force Office of Scientific Research/NP Bolling Air Force Base, Bldg. 410 Washington, D. C. 20332		13. REPORT DATE 130 April 1976
14. DISTRIBUTION STATEMENT (of this Report) Approved for public release; distribution unlimited.		15. NUMBER OF PAGES 121
16. DISTRIBUTION STATEMENT (of the abstract entered in Block 20, if different from Report)		17. SECURITY CLASS. (of this report) UNCLASSIFIED
18. SUPPLEMENTARY NOTES		19. DECLASSIFICATION/DOWNGRADING SCHEDULE
20. KEY WORDS (Continue on reverse side if necessary and identify by block number) Travel-time inversion SRO response Ray tracing Phase resolution Lateral heterogeneity Band-pass filtering Seismograph response Multiple event discrimination Seismograph calibration Focal depth		
21. ABSTRACT (Continue on reverse side if necessary and identify by block number) A synthetic travel-time data set for a heterogeneous earth model has been calculated. It is used for testing methods of travel-time inversion for structure. Methods for calculating seismograph response characteristics, for use in seismogram synthesis, from limited experimental data have been developed. The known band-limited amplitude response can be parameterized and the phase calculated or the conventional calibration pulse can be properly analyzed. A criterion for determining the minimum time separation of two recorded phases that will be resolved by a given bandpass filter		

DD FORM 1 JAN 73 1473 EDITION OF 1 NOV 68 IS OBSOLETE

UNCLASSIFIED

SECURITY CLASSIFICATION OF THIS PAGE (When Data Entered)

FILE COPY

406887

JSC

**UNCLASSIFIED**

SECURITY CLASSIFICATION OF THIS PAGE(When Data Entered)

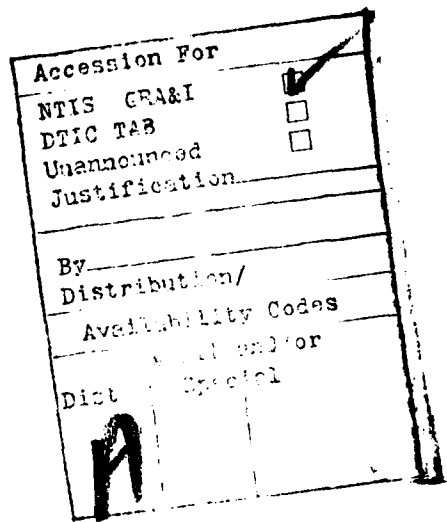
19. **Focal mechanism**

P-wave synthesis

Source parameters

Event classification

20. has been developed. The technique for determining focal depth and focal mechanism by matching synthetic long-period P waves to observed ones has been further tested and improved. A review of source theories has led to some conclusions about which source parameters can be derived from spectral properties, and what spectral parameters are useful for classification purposes.



SECURITY CLASSIFICATION OF THIS PAGE(When Data Entered)

Sponsored by  
Advanced Research Projects Agency  
ARPA Order No. 1827

ARPA Order 1827

Program Code 5F10

Name of Grantee: University of Colorado

Effective Date of Grant: 1 November 1974

Grant Expiration Date: 31 October 1976

Amount of Grant: \$173,016

Grant Number: AFOSR-75-2775

Principal Investigator: Carl Kisslinger (303) 492-7943

Program Manager: William J. Best

Title of Work: Seismic Wave Propagation and Earthquake  
Characteristics in Asia

Semi-Annual Technical Report No. 3

1 November 1975 - 30 April 1976

C. Kisslinger, E. R. Engdahl, P. Luh, M. L. Smith

R. Herrmann, W. Gawthrop, T. Hewitt, G. Lundquist

Approved for public release; distribution unlimited.

Table of Contents

Technical Report Summary	1
1. Inversion of Travel-Time Data for Upper Mantle Structure E. R. Engdahl and M. L. Smith	4
2. Determining Response Characteristics of Seismograph Systems P. C. Luh and R. B. Herrmann	11
3. A Resolving Criterion for Band-Limited Filtration P. C. Luh	66
4. Determination of Focal Depth and Focal Mechanism by Synthetic Seismograms W. Gawthrop and T. Hewitt	93
5. Classification of Seismic Events G. Lundquist	103

Technical Report Summary

1. The inversion of teleseismic travel time data to obtain local or regional velocity structure is one approach to acquiring local information needed for accurate event location. A variety of inverse techniques is available for this application, but we have needed a rigorous standard against which to measure the effectiveness of these. A synthetic, error-free data set was generated by tracing rays through a selected model of the earth which included a region of inhomogeneity. 5200 arrival times were calculated for 400 randomly-located sources, received at an array of 13 stations. One widely used inverse technique (Aki, Christoffersen, and Husebye) was applied as the first experiment on this data set. The inverse calculation picked out the axis of the anomalous structure well and revealed the general features, but the overall results are not impressive. A number of other experiments are planned, and the techniques found to be most effective will be applied to the Hindu Kush data.

2. The use of time domain techniques for determining seismic source properties requires knowledge of the amplitude and phase responses of the seismographs through which the data were acquired. Two approaches to this problem have been developed. In one, the amplitude response determined by experiment is extended by assuming asymptotic slopes at the low- and high-frequency ends of the pass-band. The amplitude response is then parameterized by a polynomial curve-fitting procedure. The minimum-phase response curve is then calculated by means of the Hilbert transform. Experimental phase response curves can be fit very closely by this technique for those cases in which they have been determined.

The other approach depends on the use of the calibration pulse on the

seismogram. Although this pulse contains all of the desired information about this region, in principle, there are severe practical difficulties in using it. The effects of background noise on the trace displaying the calculation pulse, and the ways in which limited experimental information about the amplitude and phase response can be used to improve the results of the pulse analysis have been investigated.

The most important result of this work is an amplitude and phase response curve, or equivalently, an impulse response in the time domain, for the Seismic Research Observatory (SRO) system.

3. The separation of seismic wave arrivals from several events close to each other in space and time is one of the tasks of event detection and identification. It has been suggested that application of band-pass filtering to the seismograms is one way of achieving this objective. A criterion for judging the resolving power of a filter in terms of the minimum time separation of phases required for resolution has been developed and tested for a limited data set.

4. The technique previously developed for simultaneously solving for focal depth and focal mechanism by matching synthetic seismograms to observations has been applied to a number of earthquakes. A well-recorded  $m_b = 5.8$  event off the California coast provided an especially good test case. The focal depth is resolved to about 2 km, but the focal mechanism for this thrust-type earthquake is not well-determined. Improvements to the method, including the addition of SH waves to the analysis and a water-layer in the model for submarine earthquakes are being developed.

5. The correlation of the spectral characteristics of Asian earthquakes with physical or geological characteristics of the source region is one of the goals of this research program. A systematic review of seismic source

theories has been undertaken, with the goal of determining the extent to which parameters (low frequency levels, corner frequencies, asymptotic slopes) derived from the spectra can be interpreted in a meaningful way in terms of source parameters. Conventional interpretations yield average values of important source quantities, but there are serious problems in relating these averages to the dynamics of the earthquake in a meaningful way. Carefully calculated spectra in themselves provide a useful tool for the classification of the sources.

## 1. Inversion of Travel-Time Data for Upper Mantle Structure

Martin L. Smith and E. R. Engdahl

An essential tool for the efficient development of travel-time-to-Earth-structure inverse algorithms is a realistic and effective means of assessing the limitation of any particular inverse algorithm. As an integral part of our efforts to devise (and validate) travel-time inverse techniques, we have sought to develop a reasonably rigorous standard against which to measure various methods.

We generated a large synthetic data set by utilizing ray-tracing techniques to compute point-to-point travel times for a selected three-dimensionally inhomogeneous model of the Earth. The resultant data set is error-free and, more importantly, arises from a known Earth model. (Ray theory, as we use it, is asymptotic and not exact. That the propagation of elastic energy in the Earth is modified by effects ignored here such as imperfection is elasticity, is not important to this discussion; we only require that the same theory be used in the forward and inverse calculations.) We utilize this data set by performing an inverse calculation with it and comparing the results with the known starting model.

Specifically, we suppose the Earth to be spherically symmetric except for a region extending from the surface to approximately 180 km depth and about 250 km x 250 km horizontally, centered on the equator at 0° Longitude. Inside this volume, the velocity of compressional waves varies both with depth and with one of the two local horizontal Cartesian coordinates. The resultant inhomogeneity is truly three-dimensional, but the value of the local compressional wave velocity is constant along one of the two local horizontal Cartesian coordinates (say, the one directed due north). A receiver array consisting of 13 stations having a geometry corresponding to the subarray distribution of

LASA is centered over the inhomogeneity, and 400 randomly located sources with uniform areal distribution are placed in the distance range  $30^\circ$  to  $90^\circ$ . Ray-tracing calculations for all source-receivers pairs thus generated 5200 individual arrival times.

Figure 1.1 shows a cross-section of the compressional-wave velocity anomaly we used. The quantity shown is percent deviation of the local compressional-wave velocity above the background, radially-varying velocity structure of the Earth model as a whole. The perturbation is everywhere continuous. We chose this particular anomaly (called SYNANOM I) to have appreciable horizontal and vertical structure.

The first application of the SYNANOM I data set has been to a relatively simple but rather widely used inverse technique developed by Aki, Christoffersson, and Husebye (1976). This technique uses a blockwise representation of crust and upper mantle structure, a simple but very fast form of approximate ray-tracing and a formal approach to solving the inverse problem which is, again, simple but quite effective. Only a single pass is performed on the model; i.e., travel-times through the perturbed model are not recomputed and used as the basis for a second iteration. The authors have graciously supplied a copy of the inverse program which we utilized to produce the results below.

In order to be sure that the limitations on the interpretation of this exercise are clear, we point out that this, or any other, inverse calculation requires a priori selection of the tradeoff point between data variance (or fitting variance) and model variance. We show here results for a single value of this tradeoff. Conclusions based on these results are not necessarily applicable to other calculations using this same technique.

For the inverse calculation, the inhomogeneous region was divided into six horizontal layers of 30 km thickness each. Each layer in turn was

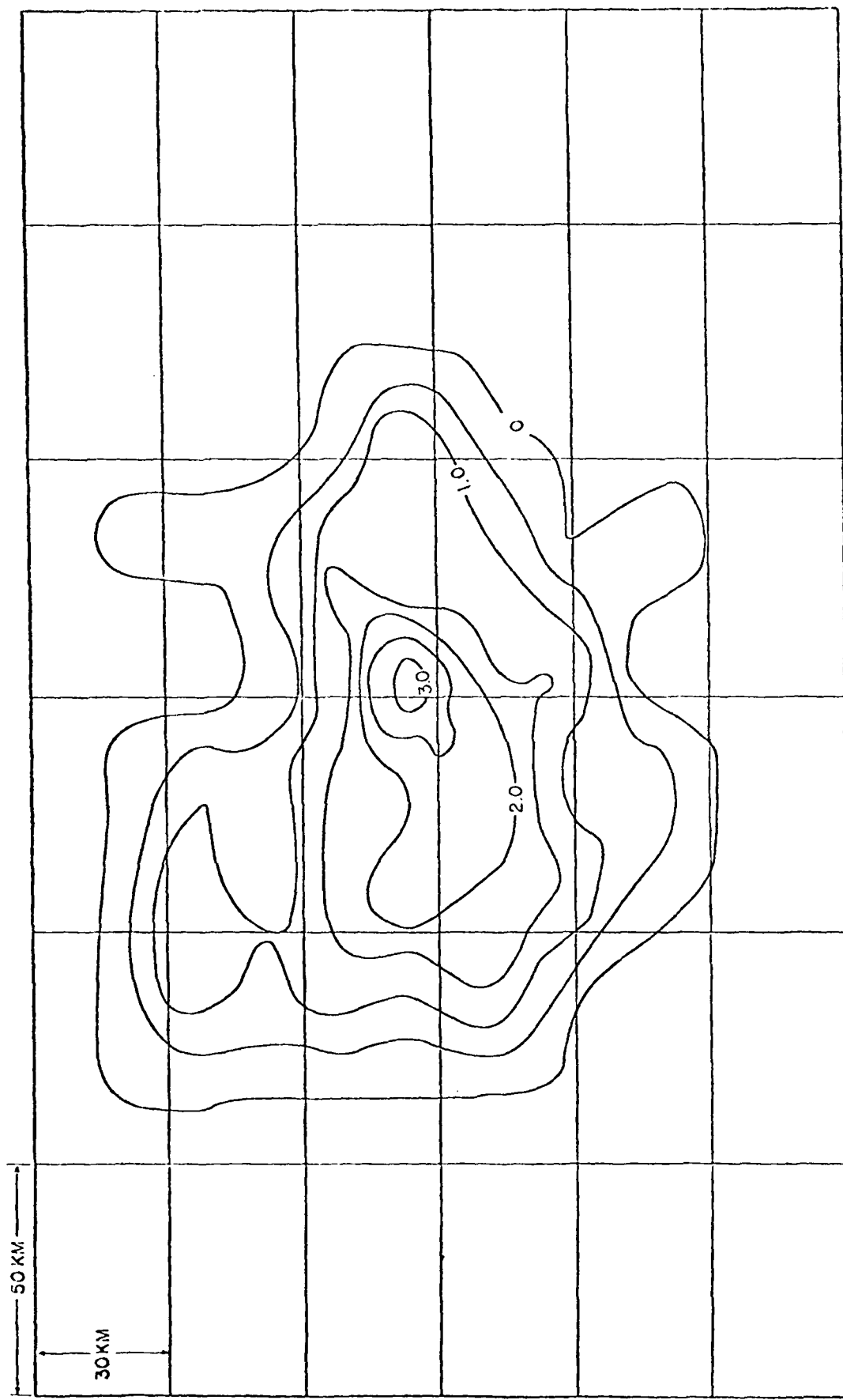


Figure 1.1: Vertical cross-section of the synthetic three-dimensional velocity anomaly SYNANOM I. Contours are percentage deviation of the local compressional wave velocity from the radially varying structure of the background spherically symmetric earth model. The superimposed grid shows the geometry of the  $\pi$  constant-velocity block structure assumed by the inverse algorithm.

horizontally partitioned into a  $6 \times 6$  array of squares 50 km on a side. The dimensions were chosen to encompass the known anomalous region.

The first-order computed perturbations were linearly estimated to reduce the observed travel-time variance by 96%, clearly a useful improvement. Figure 1.2 is a contour map of the smoothed velocity perturbation in layer 2 ( $30 \leq d \leq 60$  km). The numbers represent percent deviation from the background velocity structure. (The average deviation cannot be determined by this technique so only differences are significant in Figure 1.2.) Note that the inverse calculation has determined the axis of the structure rather well. Contour closing at the left and right of the figure occurs in regions through which no rays passed.

Figure 1.3 shows cross-sections through SYNANOM I and the corresponding inverse results. (The SYNANOM I velocity structure was appropriately integrated and averaged to make the comparison as useful as possible.) Results are shown for the top three layers. The inverse results are the arithmetic average of the two central rows of blocks. It appears that the inverse calculation is picking up the structure in a general way but the results, in this one case, are not particularly impressive. It also appears, not surprisingly, that increasing depth tends to mask the anomaly.

It is possible that these results could be substantially improved by altering the tradeoff point. Even if this is so for the SYNANOM I data set, we do not know if such a change would be feasible for an imperfect, noisy real data set. We have yet to look into, among other things, the resolution predicted by inverse theory for both perfect and noisy data sets and the possible advantage of more flexible (and more complex) representations of the anomaly's structure. Eventually we hope to apply these techniques to real data in the Hindu Kush region.

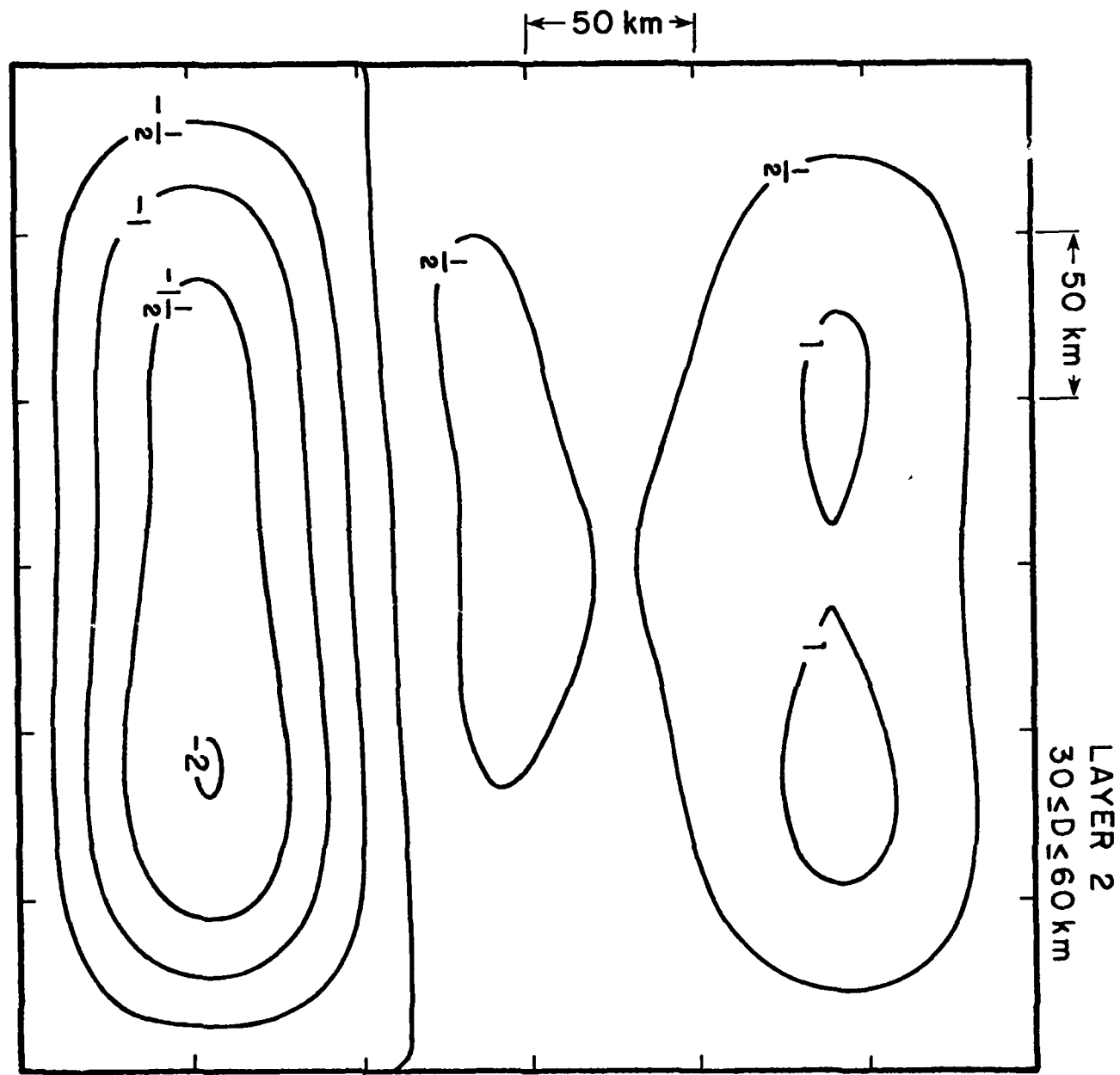


Figure 1.2: Horizontal variation of inverted compressional velocity in layer 2. Variations are shown as percent of background velocity. The continuous structure contoured here was gotten from the blockwise result of the inverse calculation by a spline smoothing process.

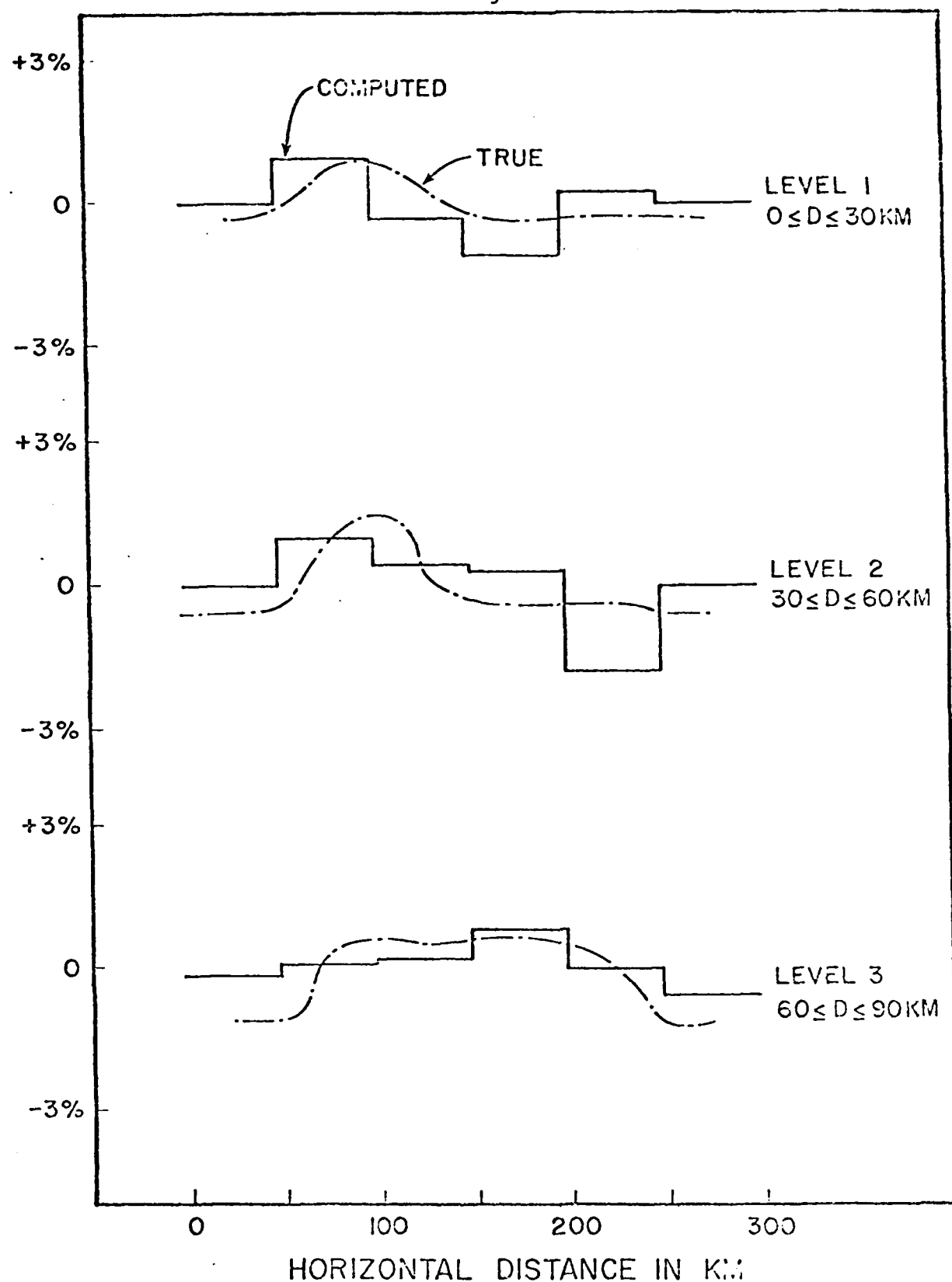


Figure 1.3: Comparison of horizontal velocity variations in SYNANOM I with the variations inferred by the inverse algorithm for each of the top three layers. The curves labelled "computed" are arithmetic averages of the two central horizontal rows of constant-velocity blocks produced by the inverse calculation. The curves labelled "true" are appropriate volume averages from SYNANOM I.

Reference

Aki, K., A. Christoffersson, and E. Husebye (1976). Determination of the three-dimensional seismic structure of the lithosphere, submitted for publication to J. Geophys. Res.

2. Determining Response Characteristics of Seismograph Systems

P. C. Luh and R. B. Herrmann

One of the primary objectives of contemporary theoretical seismology is the formulation of accurate descriptions of the time histories of earthquake ground motion, both at teleseismic and regional distances. A technique currently used to judge the adequacy of a particular theoretical source and transmission model is the comparison of observed and theoretically predicted seismograms, in the time domain, for the particular event. The model parameters are adjusted to provide the best agreement between the two seismograms (Helmberger and Malone, 1975). A prerequisite for the application of this comparison is the knowledge of the impulse response of the seismograph system.

To synthesize the impulse response, the amplitude and phase response must be known as a function of frequency. The exact frequency band over which this information is required depends upon the frequency band of the synthesized signal. Various methods have been developed for the determination of the frequency response of a seismograph system. If the particular system, such as an electromagnetic seismograph, can be parameterized, then the response can be easily determined, given the constants of the system (Mitchell and Landisman, 1969; Jarosch and Curtis, 1973).

For other systems which cannot be easily parameterized or for which the intrinsic system constants are not known, alternate approaches to determining the system response are required. Two such approaches are investigated here: the parameterization of a measured empirical amplitude response wave and the calculation of the phase response on the assumption that the system is linear and minimum-phase; and the analysis of a calibration pulse on the seismogram.

## 2.1 Parameterized Responses of Seismic Instruments.

The first approach is based on a parameterization of amplitude responses of band-limited seismic instruments, and a calculation of phase response, on the minimum-phase assumption, from the parameterized amplitude response. The main object is to provide a unified approach by which empirically determined instrumental responses can be readily incorporated into analytical or digital computations, and which avoids the need for interpolating empirical amplitude responses from data at a limited number of frequencies. The underlying assumption is only that system response as a whole behaves as a linear system (ELS or equivalent linear system), at least over its response range.

Parameterization, though slightly more involved than curve interpolation, allows an efficient and economical computation of amplitude response once a set of parameters is determined. It furthermore renders a more numerically stable calculation of minimum-phase, as described below. The only constraint other than that the system belongs to ELS is that the slopes of the parameterized expressions also vary most smoothly, thereby ensuring parameterization to be a smoothest approximation to a given empirical curve. Because such parameterization is strictly aimed at producing a simplified representation of response curves, a set of parameters, though ultimately linked to instrumental constants, in general should not be assigned a significance in terms of those constants.

Parameterized responses of a theoretical WWSSN long-period, actual WWSSN long-period, short-period, SRO long-period, short-period, USGS short-period, and LASA short-period instruments have been computed. Agreement in the theoretical example is exact within the accuracy of amplitude *inp\_t* for amplitudes, and within 1% for phases. Agreement in actual examples with empirical phase information where available is highly satisfactory, though never exact nor unique. That sufficient agreement exists at all for the phase response reflects the utility of the scheme.

Parameterized Amplitude Responses. Associated with band-limited amplitude responses on log-log scales are usually two characteristic slopes (say,  $\alpha$  at low frequency end,  $\beta$  at high frequency) outside of the response bands. Within the bands, or at least about the center of the bands, responses almost always vary smoothly. One of the simplest functions approximating these properties is

$$F(s) = s^\alpha \frac{P(s)}{Q(s)} = s^\alpha \frac{\sum_{j=0}^m a_j s^j}{\sum_{j=0}^n b_j s^j} \quad (2.1)$$

where  $P(s)$  and  $Q(s)$  are polynomials of degrees  $m$  and  $n$ , respectively, in  $s$  with real coefficients, and  $a_0 \neq 0$ ,  $b_0 \neq 0$ . That  $\beta$  does not appear in equation (2.1) and may in general not be always equal to  $\alpha+m-n$  should not cause concern, because the slopes near both ends of response bands often are uncertain on empirically calibrated curves. What is important is  $P(s)/Q(s)$  is in a classical form of transfer functions, and thus would be a reasonable representation of ELS. Moreover, as shown below,  $(\alpha, \beta)$  of ELS for all practical purposes can be taken to be integers.

The well-known property of  $P(s)/Q(s)$  for stable systems is that  $Q(s)$  have no zeros for  $\text{Re}(s) \geq 0$ . Equivalently, the  $b_j$ 's are all positive, such that roots of  $\text{Re}[Q(i\omega)] = 0$  and  $\text{Im}[Q(i\omega)] = 0$  are all real and are interlaced between each other (Hurwitz's problem). A sufficient condition for such a  $Q(s)$  is for  $b_j$ 's to be monotonically either increasing or decreasing with respect to  $j$ 's.

Because we are attempting to parameterize values of  $F(s)$  along the imaginary axis, it is more convenient to consider a variation of equation (2.1):

$$G(u) = |F(i\omega)|^2 = u^\alpha \frac{\sum_{j=0}^m c_j u^j}{\sum_{j=0}^n d_j u^j} \quad (u \geq 0) \quad (2.2)$$

where  $u = \omega^2$ , and  $c_j$ 's and  $d_j$ 's are all derived from  $a_j$ 's and  $b_j$ 's, respectively. Provided we require  $Q(s)$  to be free of zeros for  $\text{Re}(s) \geq 0$ , zeros of  $\sum_{j=0}^n d_j u^j$  cannot be positive real.

Because  $\beta$  depends on two parameters  $m$  and  $n$ , parameterization in the form of equation (2.2) would be nonunique. Thus, parameters in general ought not to be associated with instrumental constants unless equation (2.1) coincides with correct transfer function of instrument.

The simplest case of equation (2.2) is for  $m = 0$ , and  $n$  is the smallest integer no less than  $\alpha - \beta$ . This case, however, lacks the versatility of  $m \neq 0$ .

One further requirement on the parameterization is for slopes of equation (2.2) to vary the least. This would not only ensure one single smoothest approximation to an empirical curve within its response band, but also render a more accurate calculation of minimum-phases. Roots of  $\sum_{j=0}^m c_j u^j = 0$  thus cannot lie along the positive real axis.

Hence, subject to above conditions, the task is to find those  $c_j$ 's and  $d_j$ 's for a set of  $m$  and  $n$  such that a smoothest  $G^{\frac{1}{2}}$  approximates a given empirical amplitude curve best in the least-square sense. It should be pointed out also that non-integral  $\alpha$  and  $\beta$  for strictly ELS would be inappropriate. Except for one case, all  $(\alpha, \beta)$  pairs considered are integers.

Minimum-Phases. Bolduc, et al. (1972) gave a useful technique for computing minimum-phases via a Hilbert transform. This technique, summarized briefly below, is adopted here.

Let  $A(\omega)$  be the amplitude response for  $s = i\omega$ , then minimum-phases via a Hilbert transform (by closing contour in the lower half plane) are

$$\phi(\omega) = \frac{1}{\pi} \text{p.v.} \int_{-\infty}^{\infty} \frac{\ln[A(z)]}{z - \omega} dz$$

where p.v. denotes principal value. Making use of causal properties of  $A(\omega)$  and  $\phi(\omega)$ ,

$$\phi(\omega) = \frac{2}{\pi} \text{p.v.} \int_0^{\infty} \frac{\omega \ln[A(z)]}{z^2 - \omega^2} dz$$

Integrating by parts and letting  $x = \ln(z/\omega)$ ,

$$\phi(\omega) = \frac{1}{\pi} \text{p.v.} \int_{-\infty}^{\infty} B(\omega, x) \ln |\coth(\frac{x}{2})| dx \quad (\omega > 0) \quad (2.3)$$

becomes the form most amenable for numerical computations because  $\ln|\coth(x/2)|$  decays rapidly away from  $x = 0$  and because  $B(\omega, x) = B(\omega_0, x + \ln(\omega/\omega_0)) = \frac{d}{dx}(\ln[A(\omega e^x)])$  can be obtained by translating  $B(\omega_0, x)$  along negative  $x$  direction by  $\ln(\omega/\omega_0)$ , where  $\omega_0$  is some reference frequency at which derivatives of  $\ln[A(\omega_0 e^x)]$  with respect to  $x$  are computed. The property of  $\ln|\coth(x/2)|$  allows the limits of the integration to be truncated at some finite values, but in so doing, one must be prepared to supply more unstable quantities of slopes of  $\ln(A)$ .

Thus lies the requirement on the parameterization for smoothly varying slopes. Since  $\ln[A(\omega)] \approx \frac{1}{2} \ln[G(u)]$ ,

$$B(1, x) \underset{\alpha}{\sim} \alpha + \frac{\sum_{j=1}^m j c_j e^{2jx}}{\sum_{m=0}^m c_j e^{2jx}} - \frac{\sum_{j=1}^n j d_j e^{2jx}}{\sum_{j=0}^n d_j e^{2jx}}$$

can be readily computed, and would coincide with derivatives of  $\ln(A)$  if  $G^{\frac{1}{2}}$  fits  $A$  identically everywhere.

Minimum-phases  $\phi(\omega)$  of equation (2.3) incidentally involves no arbitrariness of adding a multiple of  $\pi$  as for phases taken to be arguments of a complex response function. Since  $\int_{-\infty}^{\infty} \ln|\coth(x/2)|dx = \pi^2/2$ , minimum-phases asymptotically approach  $\alpha\pi/2$  at small  $\omega$ , while  $(\alpha+m-n)/2 \underset{\omega \rightarrow \infty}{\sim} \beta\pi/2$  at large  $\omega$ . However, unless the instrument polarity is already known to be the same as that of motion to be measured,  $\phi(\omega)$  could be off by  $\pi$  from actual phases of ELS. This simple relation between phases and slopes of amplitudes represents another means by which slopes of decay at both ends can be estimated from empirical phase calibrations. One such example is given next. For comparison with computed  $\phi(\omega)$ ,  $\pi$  is added to any empirical phases whose instrumental sensing polarity is opposite to that of ground motion; WWSSN long-period vertical instruments whose positive galvanometer reflections are negatively related to upward ground displacements in construction of transfer functions, for example, typify the case.

Parameterized Response Curves. To demonstrate the utility of a parameterization of an amplitude response curve and of a subsequent calculation of minimum-phases, the complete scheme is applied to WWSSN, SRO, USGS and LASA instruments. In all, 12 figures are presented, where abscissa is log frequency and ordinate on the left is log amplitude, while on the right, phase in radians. Experimental phase information is available only for SRO long-period and USGS short-period instruments.

(i) A Theoretical Example:

Since theoretical responses of WWSSN long-period instruments are well-documented (see, for example, Willmore, 1969, or Kisslinger, 1971), it is useful to study this response. Theoretical instrumental responses can be computed from its well-known transfer function by supplying appropriate natural periods and damping constants of seismometer and galvanometer, as well as their coupling constant.

The constants adopted for Figure 2.1 are  $T_s = 30$  (sec) ,  $T_g = 100$  (sec) ,  $h_s = h_g = 1$  and  $\sigma^2 = 0.01$  , and amplitude response is normalized to be 1 at frequency  $f = \omega/(2\pi) = 0.04$  Hz. Points denoted by + on the figure are theoretical values of amplitude and phase, which incidentally contains an extra  $\pi$  , as described above. Eighteen amplitude points were used to find  $d_j$ 's in equation (2.2) with  $m = 0$  ,  $c_0 = 1$  , and  $n = 4$  , since  $(\alpha, \beta)$  is known to be (3,-1). The input amplitude points were recorded to seven significant figures from the theoretical values. Parameters  $d_j$ 's are given in Table 2.1, multiplied by a factor of  $(2\pi)^{2j}$  so  $f$  instead of  $\omega$  can be used in computations.

The difference through 6 significant figures between theoretical and computed  $d_j$ 's exists only in  $d_0$  , and is only 1 in the least significant figure. Computed phases agree with theoretical ones to 1%, the discrepancies being primarily due to the integrand being singular at  $x = 0$  and due to truncation of integration limits in equation (2.3) in actual computations. Computed points are denoted by small dots, and illustrate smoothly varying amplitude and phase.

Such remarkable agreement exists because the system is linear and because parameterized form actually is identical to theoretical transfer function. Parameters so computed are unique within accuracy of digital computations, as confirmed by the fact that different sets of input points produced identical parameters to six significant figures. In this case, however, parameters can be

WWSSN (30-100) HS = 1.00 HG = 1.00 SIGMA SIGMA = 0.010  
 $\alpha = 3.0$   $\beta = -1.0$

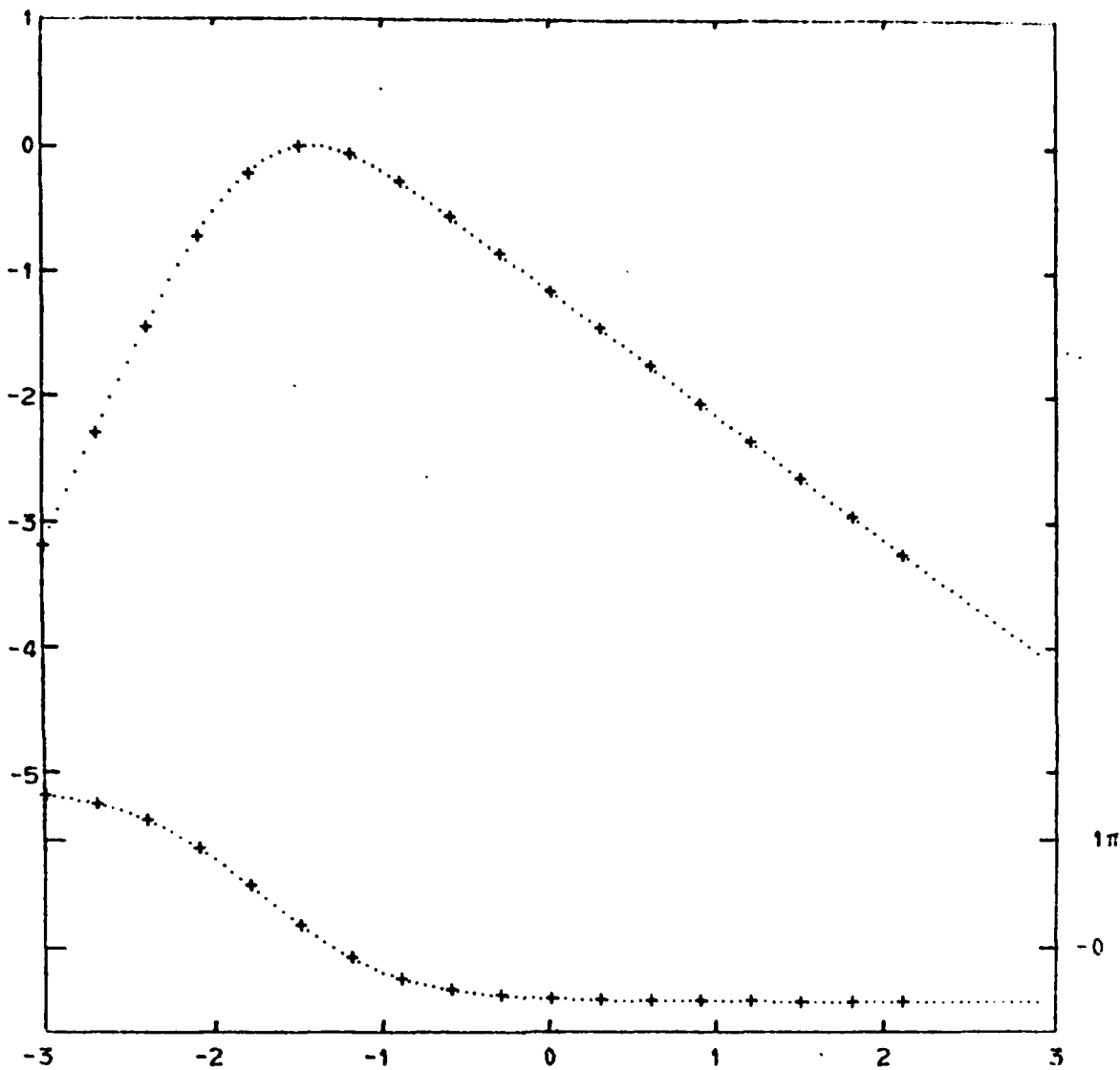


Figure 2.1: Theoretical responses of WWSSN (30-100) instruments.

meaningfully related to the five instrumental constants, though in general correlation even under such an ideal condition is still impossible because number of instrumental constants usually outnumbers that of parameters.

(ii) WWSSN Instruments:

Points, read off from empirical amplitude curves supplied by Geotech Corp., are used for computing  $d_j$ 's for 2 LP ((30-100) and (15-100) systems) and 1 SP instruments.  $(\alpha, \beta)$  is (3, -1) for the long-period systems, (3, -2) for the short-period, which at high frequencies include an extra decay due to inductance of transducer coils. Again  $d_j$ 's are listed in Table 2.1, and minimum-phases are displayed in Figures 2.2 - 2.4. Because input points can be read off only at best to 3 significant figures,  $d_j$ 's are not determined with as high a confidence as those of (i). If the empirical curves further contain some slight errors,  $d_j$ 's would even be more nonunique. Nonetheless, any set of  $d_j$ 's would approximate an empirical curve within its error to be useful, and minimum-phases would not differ greatly from one set of  $d_j$ 's to another.

Though WWSSN instruments are generally assumed and regarded to be linear, a simple computation of substituting different sets of instrumental constants into transfer function reveals that hardly any reasonable set fits the empirical curves well. This very distinctly exhibits that even with the simplest linear instruments, responses ought to be always calibrated empirically since those computed via a transfer function are usually too idealized to be reliable.

(iii) SRO Instruments:

As in (ii), points are read off from empirical amplitude curves (provided by Holcomb, 1975) of LP and SP instruments. However, some extrapolated points, denoted on the figures by  $\circ$ , are also incorporated into the input, as the calibration curves do not provide information of fall-off at high frequencies. Extrapolation is necessary because, for simplicity, numerical algorithm used

WWSSN (30-100) EMPIRICAL AS GIVEN BY GEOTECH

$$\alpha = 3.0 \quad \theta = -1.0$$

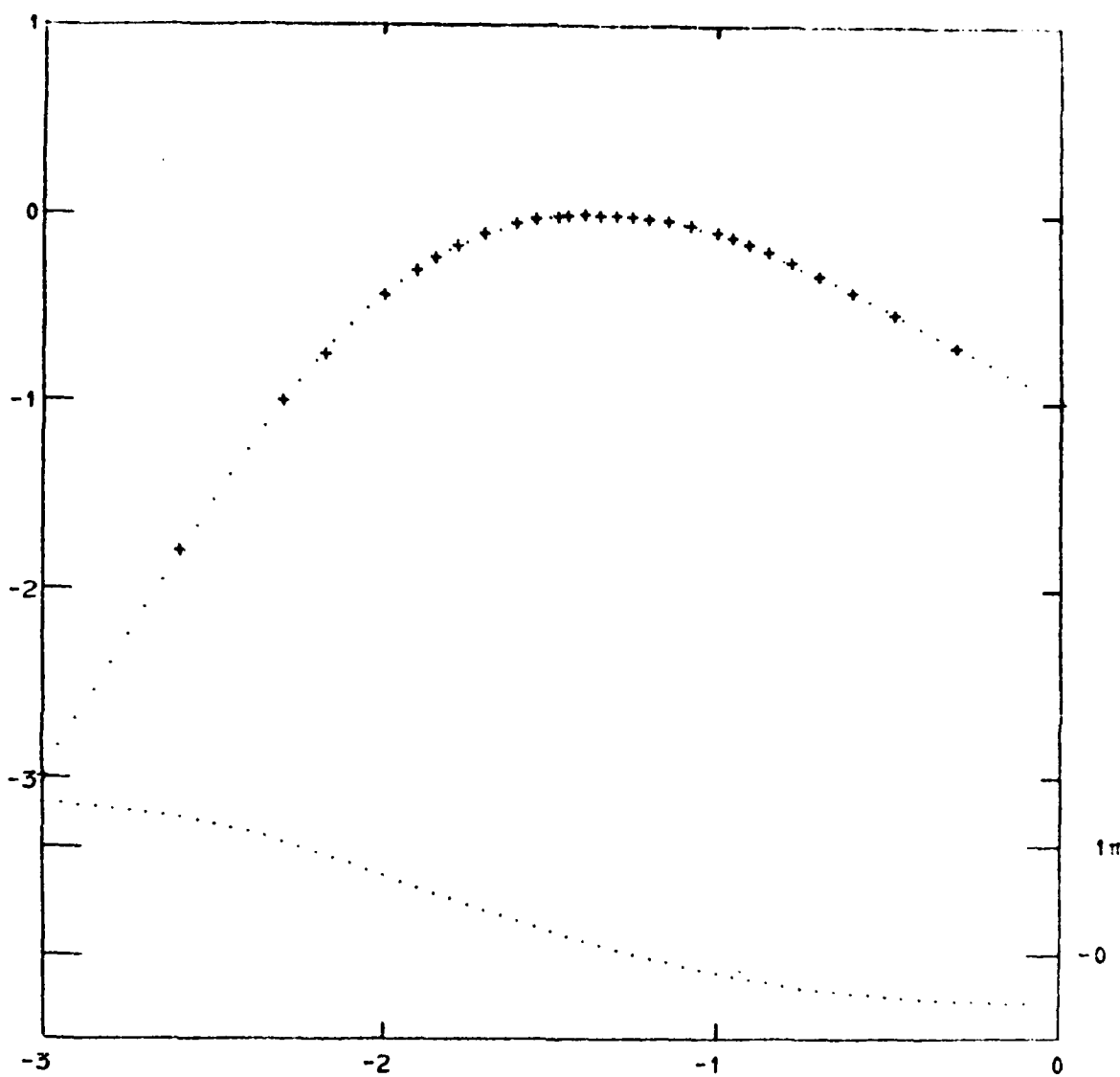


Figure 2.2: Empirical responses of WWSSN (30-100) instruments.

WWSSN (15-100) EMPIRICAL AS GIVEN BY GEOTECH

$$\alpha = 3.0 \quad \theta = -1.0$$

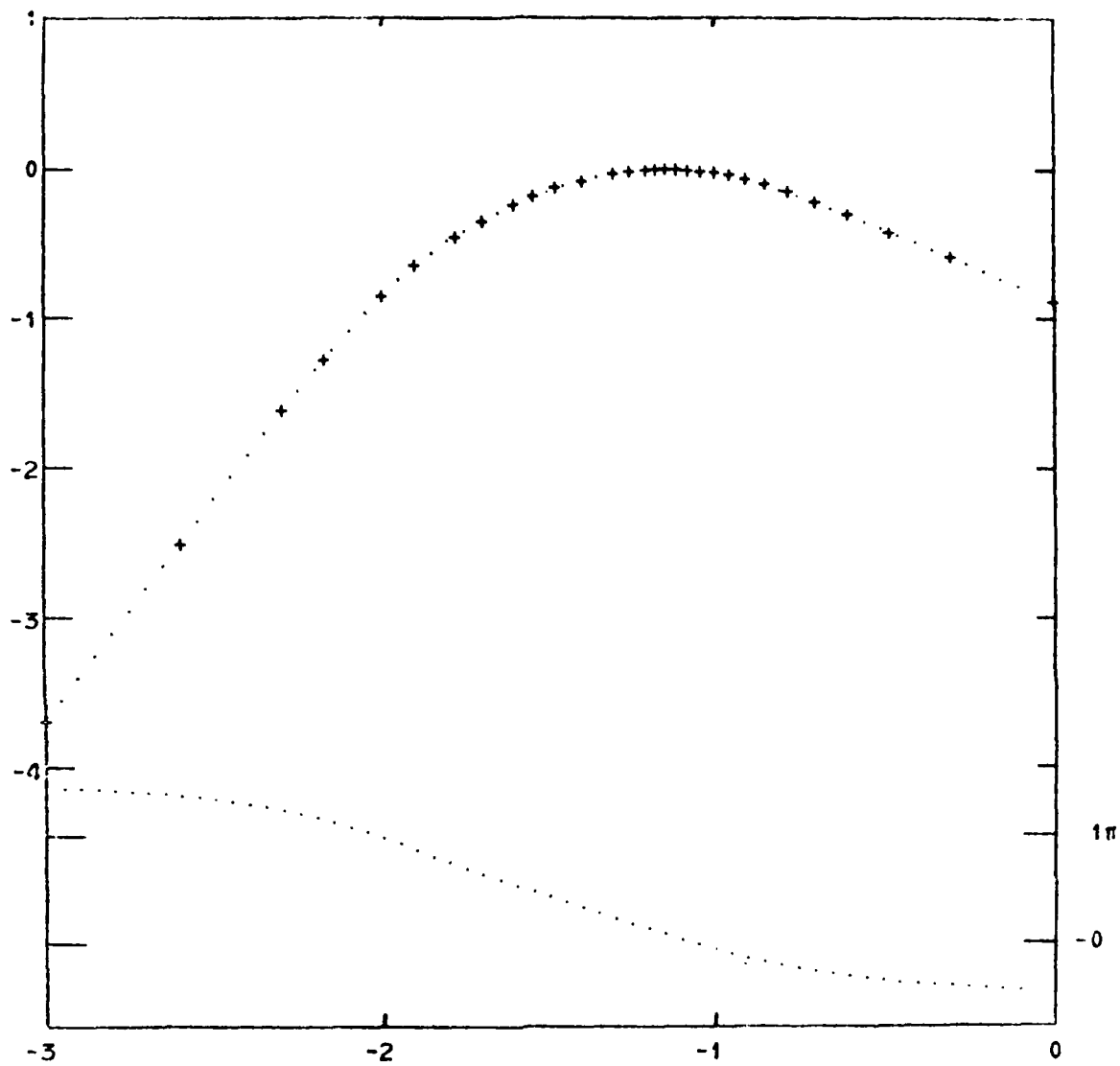


Figure 2.3: Empirical responses of WWSSN (15-100) instruments.

WWSSN (SP) EMPIRICAL AS GIVEN BY GEOTECH

$$\alpha = 3.0 \quad \beta = -2.0$$

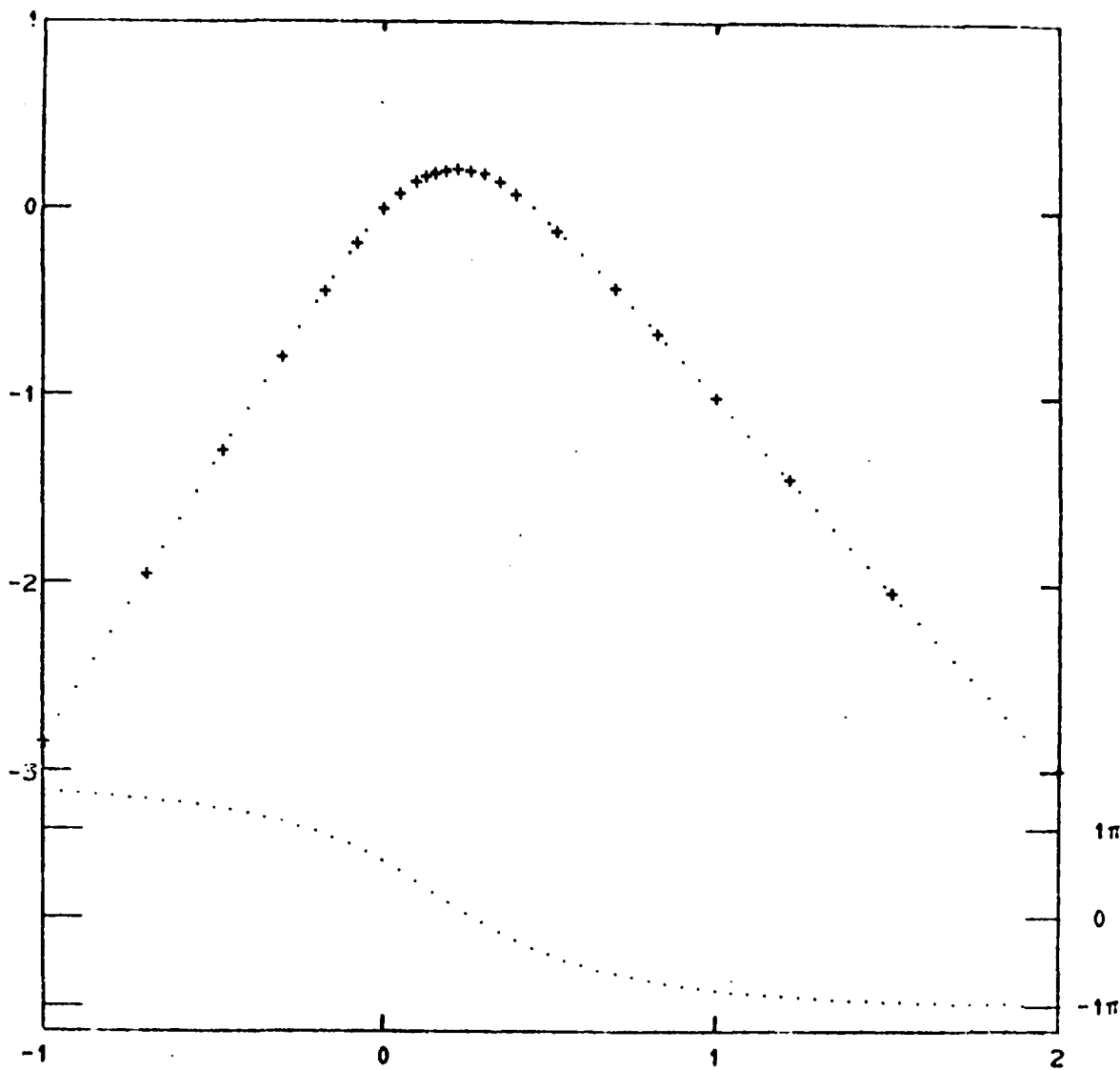


Figure 2.4: Empirical WWSSN (SP) responses.

Table 2.1: Parameters for various instruments with  $c_0 = 1$  and  $d'_j = (2\pi)^{-2j} d_j$ .  
 These parameters apply strictly to curves shown in Figs 1-12.

Theoretical WISSN (30-100)	WISSN (30-100)	WISSN (15-100)	WISSN (SP)
$d'_0$	$2.38724 \cdot 10^{-12}$	$8.96540 \cdot 10^{-13}$	$2.49483 \cdot 10^{-11}$
$d'_1$	$5.26147 \cdot 10^{-3}$	$2.17357 \cdot 10^{-8}$	$9.93382 \cdot 10^{-8}$
$d'_2$	$3.13512 \cdot 10^{-4}$	$3.41306 \cdot 10^{-4}$	$1.39596 \cdot 10^{-3}$
$d'_3$	$4.73534 \cdot 10^{-1}$	$6.05513 \cdot 10^{-1}$	$4.24246 \cdot 10^{-1}$
$d'_4$	$1.93366 \cdot 10^2$	$9.47240 \cdot 10^1$	$5.68088 \cdot 10^1$
$d'_5$			$2.03961 \cdot 10^{-2}$
			$1.00315 \cdot 10^{-2}$

SRO (LP)	#1	SRO (LP)	#2	SRO (LP)	#3	SRO (SP)
$d'_0$	$5.76375 \cdot 10^{-23}$	$4.28549 \cdot 10^{-23}$	$1.84535 \cdot 10^{-25}$	$1.09547 \cdot 10^{-2}$		
$d'_1$	$4.83727 \cdot 10^{-23}$	$2.40132 \cdot 10^{-18}$	$1.38739 \cdot 10^{-20}$		$2.21703 \cdot 10^{-1}$	
$d'_2$	$1.93663 \cdot 10^{-18}$	$3.52546 \cdot 10^{-15}$	$3.01041 \cdot 10^{-16}$		$5.70386 \cdot 10^{-1}$	
$d'_3$	$1.00925 \cdot 10^{-14}$	$2.26614 \cdot 10^{-11}$	$-3.95988 \cdot 10^{-13}$		$1.84869 \cdot 10^{-1}$	
$d'_4$	$7.50193 \cdot 10^{-12}$	$5.23430 \cdot 10^{-9}$	$1.80590 \cdot 10^{-9}$		$1.46143 \cdot 10^{-1}$	
$d'_5$	$1.43119 \cdot 10^{-8}$	$-3.74486 \cdot 10^{-6}$	$-1.28252 \cdot 10^{-6}$		$4.90508 \cdot 10^{-3}$	
$d'_6$	$3.04793 \cdot 10^{-7}$	$2.19973 \cdot 10^{-2}$	$1.02819 \cdot 10^{-3}$		$2.58472 \cdot 10^{-4}$	
$d'_7$	$6.07099 \cdot 10^{-3}$	$-9.11175 \cdot 10^0$	$-2.53725 \cdot 10^{-1}$		$5.51015 \cdot 10^{-6}$	

$d'_3$	$-3.21012 \cdot 10^{-1}$	$2.46312 \cdot 10^3$	$6.29166 \cdot 10^1$	$6.39441 \cdot 10^{-8}$
$d'_9$	$1.79415 \cdot 10^2$	$-3.10462 \cdot 10^5$	$-5.44985 \cdot 10^3$	$2.20113 \cdot 10^{-10}$
$d'_{10}$	$3.56063 \cdot 10^3$	$2.47320 \cdot 10^7$	$4.01516 \cdot 10^5$	
$d'_{11}$	$2.22086 \cdot 10^5$	$-9.92675 \cdot 10^8$	$1.01520 \cdot 10^7$	
$d'_{12}$	$2.35243 \cdot 10^6$	$2.57101 \cdot 10^{10}$	$-1.47355 \cdot 10^8$	
$d'_{13}$		$5.84606 \cdot 10^{10}$	$1.56569 \cdot 10^{10}$	

	USGS (SP) #1	USGS (SP) #2	LASA (SP) #1	LASA (SP) #2
$d'_0$	$2.38118 \cdot 10^{-9}$	$1.02914 \cdot 10^{-11}$	$9.42922 \cdot 10^{-2}$	$1.04133 \cdot 10^{-1}$
$d'_1$	$1.49581 \cdot 10^{-7}$	$7.44340 \cdot 10^{-9}$	$3.71174 \cdot 10^{-1}$	$3.12255 \cdot 10^{-1}$
$d'_2$	$1.05948 \cdot 10^{-7}$	$1.57511 \cdot 10^{-7}$	$3.67916 \cdot 10^{-1}$	$4.70911 \cdot 10^{-1}$
$d'_3$	$1.50388 \cdot 10^{-7}$	$9.48297 \cdot 10^{-8}$	$1.12169 \cdot 10^{-1}$	$4.65577 \cdot 10^{-2}$
$d'_4$	$1.07550 \cdot 10^{-9}$	$1.53107 \cdot 10^{-7}$	$1.67666 \cdot 10^{-2}$	$3.35362 \cdot 10^{-2}$
$d'_5$	$-9.54806 \cdot 10^{-13}$	$9.92766 \cdot 10^{-10}$	$5.18055 \cdot 10^{-4}$	$-1.33039 \cdot 10^{-3}$
$d'_6$	$2.40579 \cdot 10^{-15}$	$-5.04623 \cdot 10^{-13}$	$7.33697 \cdot 10^{-6}$	$9.80059 \cdot 10^{-5}$
$d'_7$	$-2.37040 \cdot 10^{-19}$	$1.81305 \cdot 10^{-15}$	$5.15944 \cdot 10^{-7}$	$-1.55703 \cdot 10^{-6}$
$d'_8$	$1.71659 \cdot 10^{-22}$	$5.91308 \cdot 10^{-20}$	$3.50962 \cdot 10^{-9}$	$3.05155 \cdot 10^{-8}$
$d'_9$	$1.97970 \cdot 10^{-27}$	$3.86026 \cdot 10^{-23}$	$4.56727 \cdot 10^{-11}$	$-1.46762 \cdot 10^{-11}$
$d'_{10}$	$1.17603 \cdot 10^{-31}$	$4.70211 \cdot 10^{-28}$	$2.16276 \cdot 10^{-13}$	$6.84511 \cdot 10^{-13}$
$d'_{11}$				$1.07177 \cdot 10^{-15}$

for finding  $d_j$ 's does not incorporate the condition of flatly and smoothly varying slopes. Should this condition be added, extrapolation may not be necessary.

Figures 2.5 - 2.7 show three versions of LP responses with  $(\alpha, \beta)$  being respectively  $(5, -7)$ ,  $(4, -9)$  and  $(4.5, -8.5)$ . Inputs of the three versions differ only near the ends; input at low frequencies for versions 2 and 3, for example, is adjusted slightly to accommodate for different  $\alpha$ 's. Versions 2 and 3 were tested because minimum-phases of version 1 did not agree well with calibrated phases.

$\beta = -9$  was arrived at for version 2 by examining the tendency of decrease in empirical phases at high frequencies, where phases should asymptotically approach  $\beta\pi/2$  for ELS. Note a greatly improved fit over version 1's. But there still remains a slight constant off-set.

Version 3 was therefore concocted, with non-integral  $(\alpha, \beta)$ . The fit becomes nearly exact, but whether or not non-integral  $(\alpha, \beta)$  is acceptable for ELS is somewhat questionable. That non-integral  $(\alpha, \beta)$  concurs with calibrations may well imply either that the system as a whole is actually slightly slightly nonlinear, or that calibrations are off by a small constant term ( $\approx \pi/4$ ).

Figure 2.8 shows SP response. Because empirical curve is limited, many different  $(\alpha, \beta)$  are possible. However, only one set  $(4, -5)$  is treated with an extrapolation again at high frequencies.

#### (iv) USGS Instruments:

Empirical curves are based on a USGS report by Bakun and Dratler (1976). Both amplitude and phase information are available, though their phase values are off by  $\pi/2$  since their theoretical values for a simple mass seismometer are likewise off by  $\pi/2$ . Accordingly,  $\pi/2$  is added to their empirical phases in Figures 2.9 and 2.10. Two versions are concocted with  $(\alpha, \beta)$  being

SRO (LP) INPUT - SMOOTHED AND EXTRAPOLATED VERSION 1 OF L. G. HOLCOMB'S  
 $\alpha = 5.0$        $\theta = -7.0$

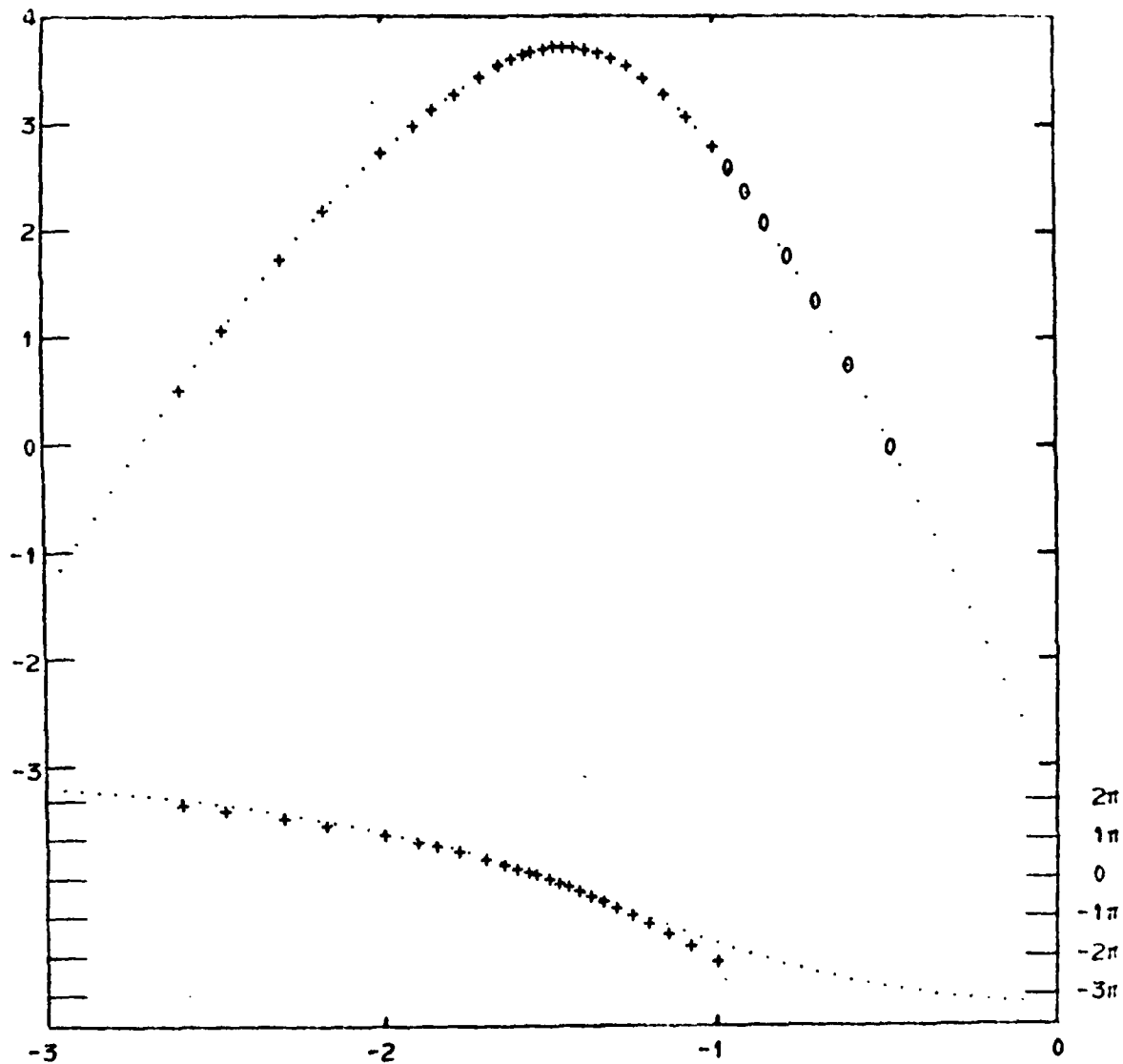


Figure 2.5: Version 1 of SRO (LP) responses.

SRO (LP) INPUT - SMOOTHED AND EXTRAPOLATED VERSION 2 OF L. G. HOLCOMB'S  
 $\alpha = 4.0$        $\beta = -9.0$

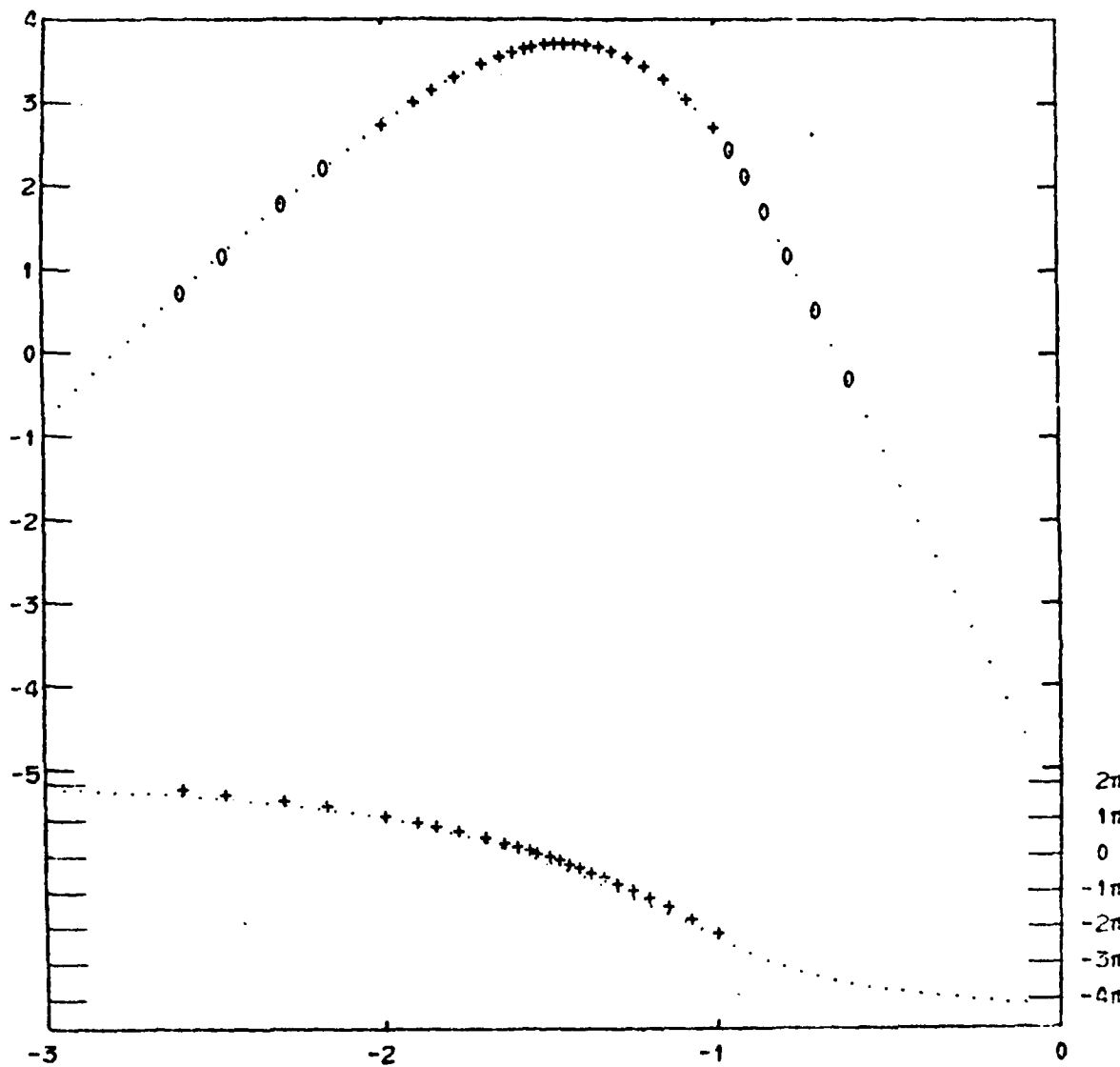


Figure 2.6: Version 2 of SRO (LP) responses.

SRO (LP) INPUT - SMOOTHED AND EXTRAPOLATED VERSION 3 OF L. G. HOLCOMB'S  
 $\alpha = 4.5$        $\theta = -8.5$

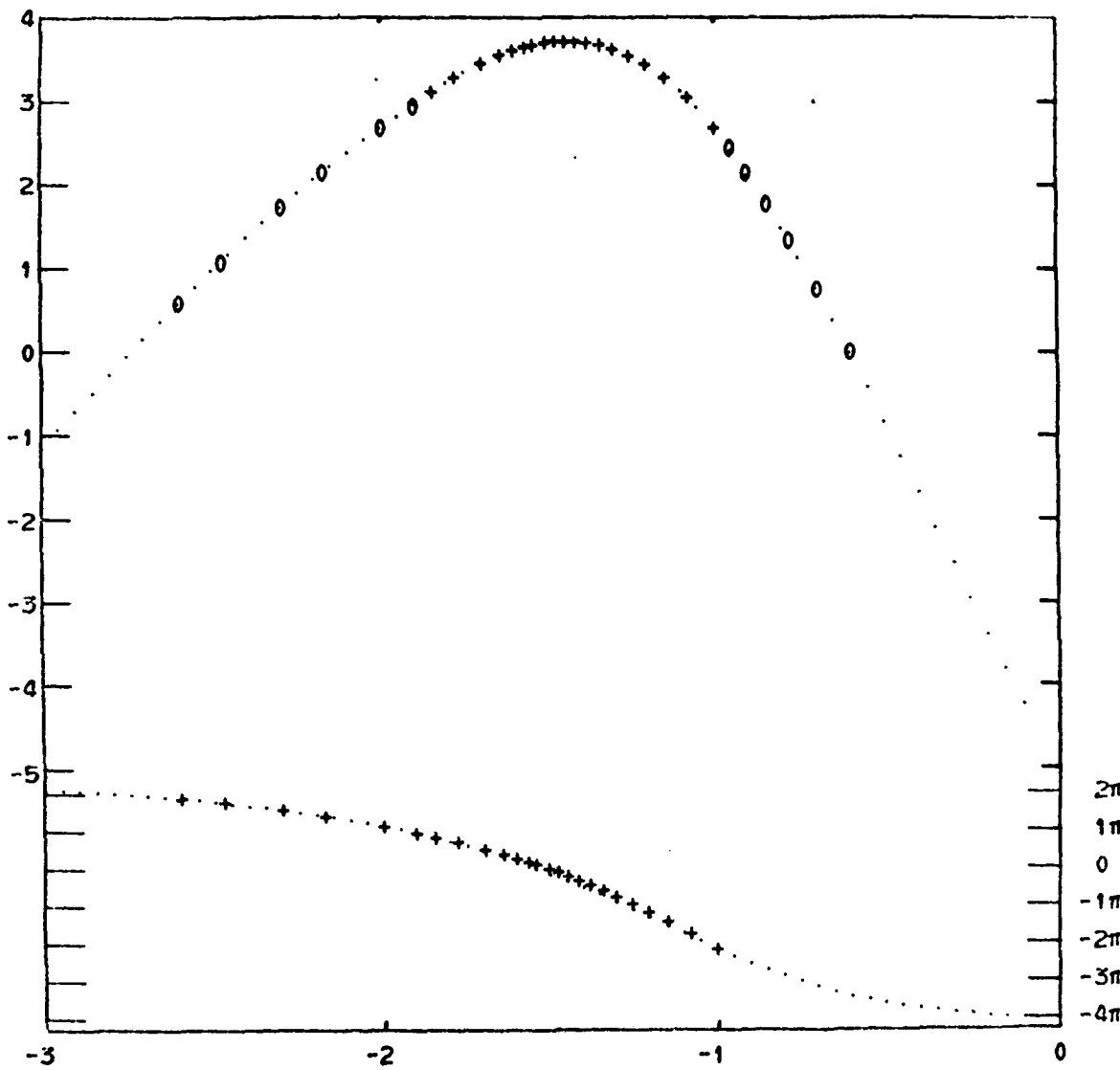


Figure 2.7: Version 3 of SRO (LP) responses.

SRO (SP) INPUT - SMOOTHED AND EXTRAPOLATED VERSION OF L. G. HOLCOMB'S

$$\alpha = 4.0 \quad \theta = -5.0$$

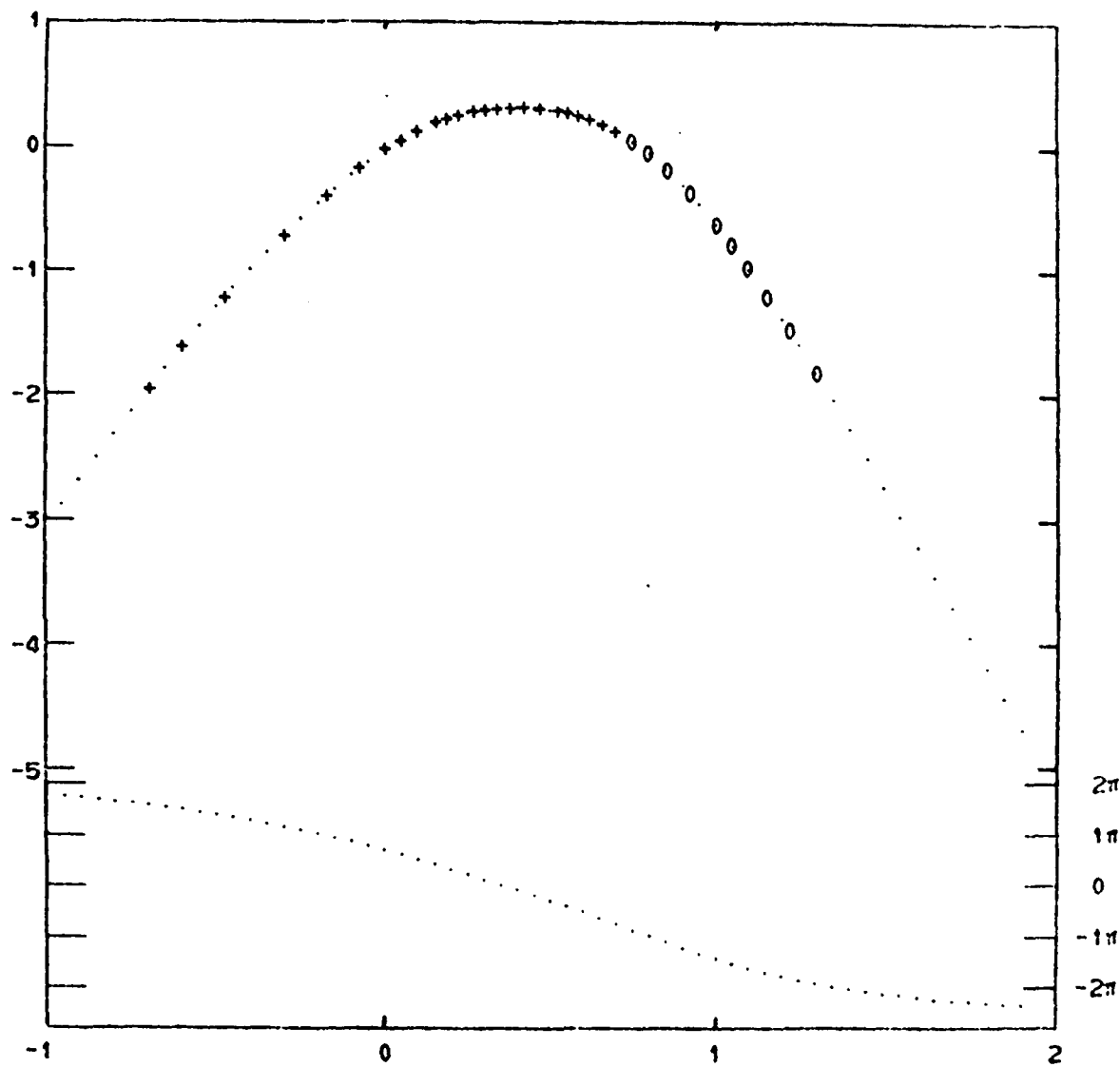


Figure 2.8: Responses of SRO (SP) instruments.

USGS (SP) INPUT - SMOOTHED AND EXTRAPOLATED VERSION 1 OF W. H. BAKUN, ET AL.'S  
 $\alpha = 4.0$        $\theta = -6.0$

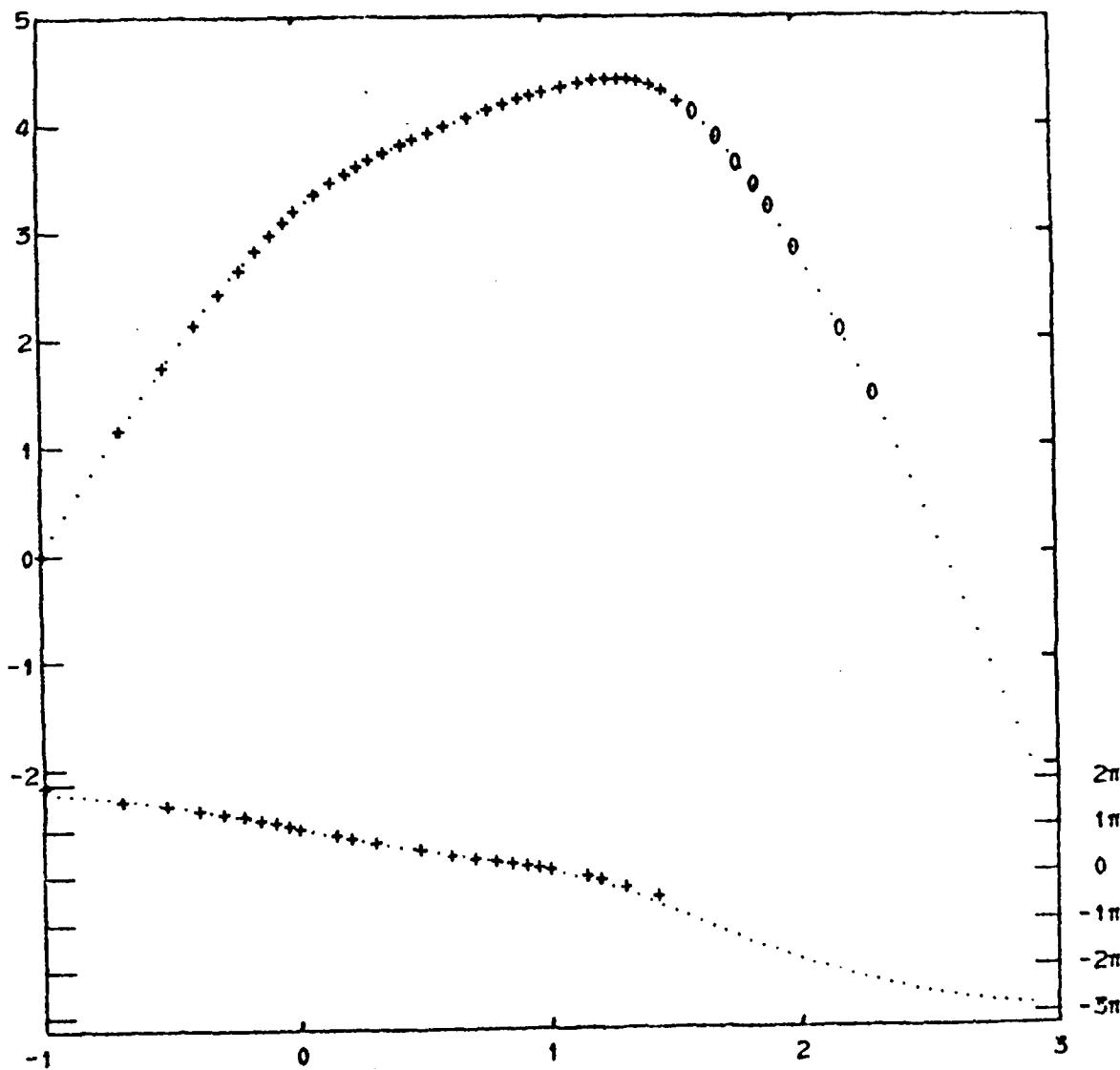


Figure 2.9: Version 1 of USGS (SP) instruments.

USGS (SP) INPUT - SMOOTHED AND EXTRAPOLATED VERSION 2 OF W. H. BAKUN, ET AL.'S  
 $\alpha = 5.0$        $\theta = -5.0$

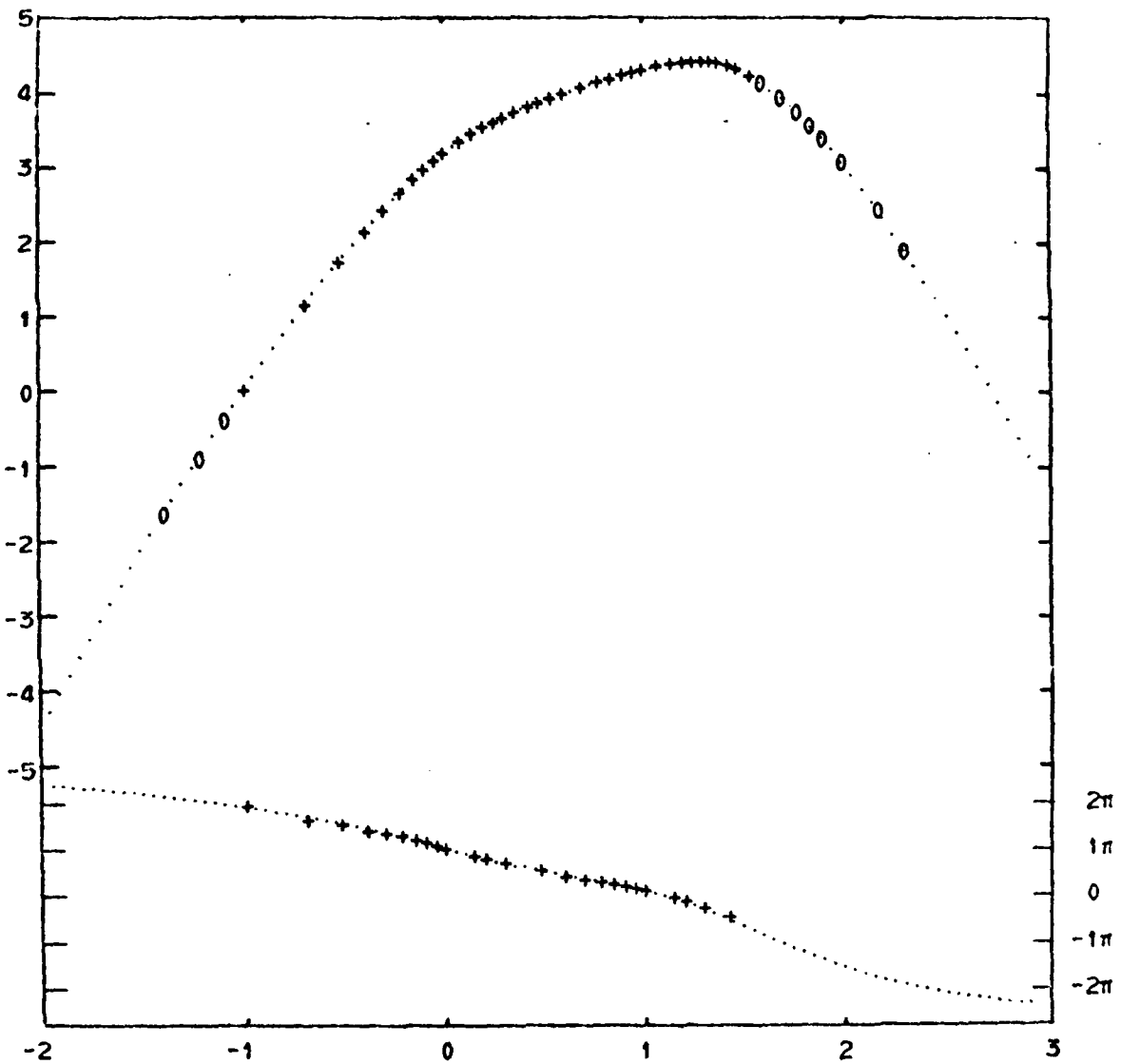


Figure 2.10: Version 2 of USGS (SP) instruments.

(4, -6) and (5, -5). Again version 2 is the better of the two. Version 1 shows that minimum-phases at low frequencies (about  $f = 0.1$  ) are slightly low, while at high frequencies, too low.

Here is another example illustrating versatility and utility of the present scheme. Empirical amplitude curve at low frequencies indicates that the slope has almost certainly settled down to 4 . But a comparison of minimum-phases with calibrated phases indicates otherwise. With a few extrapolation points added to accommodate the new  $(\alpha, \beta)$  , a better fit is obtained. However, whether or not version 2 represents a better parameterization over version 1 in characterizing the instrument's responses depends on how accurate calibrated responses are. If calibrated curves contain non-negligible uncertainties, both versions would be equally adequate because about the peak response they yield nearly identical parameterized responses.

(v) LASA Instrument:

Empirical amplitude curve given by Forbes, et al. (1965) is even worse in details than that of SRO SP instrument. Nevertheless, two versions are given in Figures 2.11 and 2.12 with  $(\alpha, \beta)$  being (4, -6) and (4, -7). The latter would be the better of the two because the instrument is designed to have a sharp decay in amplitude response at frequencies higher than 6 Hz.

Discussion. That parameterization and minimum-phase calculation work equally well for SRO-LP and USGS -SP instruments means in general band-limited instruments are indeed ELS. Thus, parameterization in terms of a transfer function of a linear system becomes a highly amenable scheme. The advantage of such a scheme is its simplicity. Nothing needed be known about constituents of an instrument; only its overall amplitude response is required. Deconvolution would be straightforward provided we know a parameterized expression and provided it approximates calibrated values well.

LASA (SP) INPUT - SMOOTHED AND EXTRAPOLATED VERSION 1 OF C. B. FORBES, ET AL.  
 $\alpha = 4.0$        $\beta = -6.0$

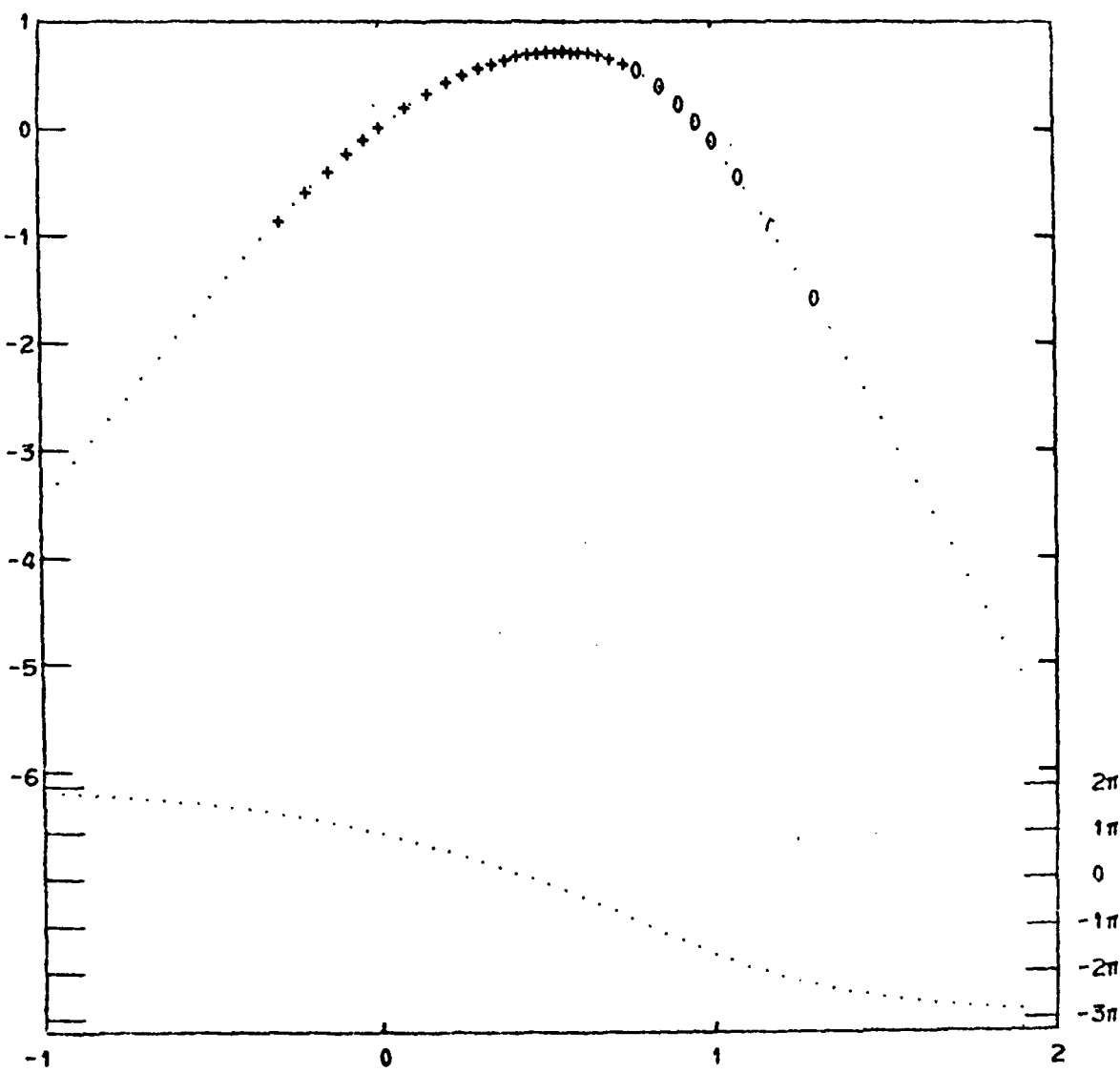


Figure 2.11: Version 1 of LASA (SP) instruments.

LASA (SP) INPUT - SMOOTHED AND EXTRAPOLATED VERSION 2 OF C. B. FORBES, ET AL.  
 $\alpha = 4.0$        $\beta = -7.0$

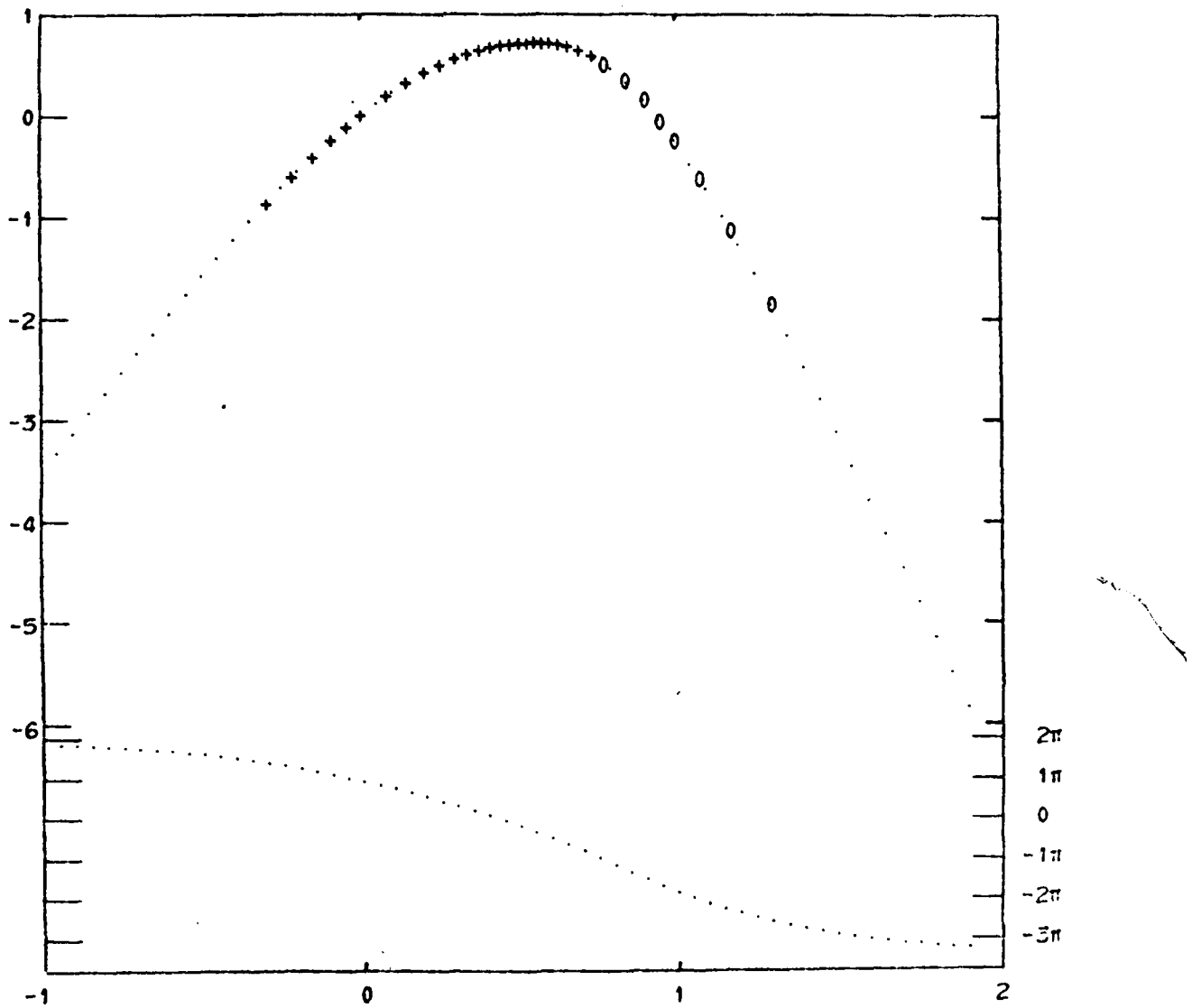


Figure 2.12: Version 2 of LASA (SP) instruments.

It should be pointed out, however, that parameters  $d_j$ 's in general depend strongly on input points. Thus, it is best not to use actual calibration points for input, as these points are susceptible to a variety of errors. Rather, it is best to read off points from a reasonable smooth curve passing through the calibration points. It is not too stringent to require input points to be more or less ideal, since the underlying assumption of the scheme is for the system on the whole to behave like a linear system, for which the response curve must be a smooth one.

Because of its simplicity, the present scheme can be easily applied to determine response characteristics of instruments of the same type at different station sites. If stations were further equipped with small computer, a straightforward deconvolution could be easily effected once a set of parameters is known. A calculation of minimum-phases would also be useful in checking accuracy of calibrations; for example, a deviation of less than  $\pi/4$  when instrumental sensing polarity with respect to that of ground motion is known may be acceptable, but a consistent deviation of more than  $\pi/4$  for ELS would suggest inaccurate calibrations.

The programs for calculating the parameters and calculating the minimum phases are available from Cires on request.

## 2.2 Determining the Impulse Response, with Emphasis on the SRO System.

Steady-state or transient calibration techniques are routinely used to provide the information needed to calculate the system response. However, noise and general inadequacy of the calibration technique often make it difficult to obtain the amplitude and phase responses over a frequency range sufficiently wide to permit the synthesis of the response of the systems to an impulse in ground displacement. Here we demonstrate how the noise impairs the determination

of the impulse response by an analysis performed in the time domain, as well as how even limited knowledge of the amplitude and phase response can be effectively used to determine the system impulse response upon making some assumptions about that response.

The general principles relating the response of a linear system for an arbitrary input to its impulse response are assumed known, as are the relations between the response of a seismograph to an impulse in ground displacement and its responses to impulses in ground velocity or acceleration, and to a step in ground acceleration. These are summarized as follows. If  $h(t)$  is the response to an impulse in ground displacement, and  $H(f)$  its Fourier transform, the system response to a step in velocity is

$$a_v(t) = u(t) * h(t)$$

where  $u(t)$  is the unit step function, with Fourier transform

$$A_v(f) = \frac{1}{(i2\pi f)^2} H(f)$$

The response to an impulse in acceleration is

$$a_a(t) = t u(t) * h(t)$$

with transform

$$A_a(f) = \frac{1}{(i2\pi f)^2} H(f)$$

and to a step in acceleration

$$a_s(t) = \frac{1}{2} t^2 u(t) * h(t)$$

with transform

$$A_s(f) = \frac{1}{(12\pi f)^3} H(f)$$

The WWSSN 15-100 Long Period Seismograph. The system transfer function of an electromagnetic seismograph system (Hagiwara, 1958) is

$$H(f) = \frac{-\frac{1}{2\pi} iKf^3}{R(f) + iI(f)} \quad (2.4)$$

where

$K$  = scaling constant,

$$R(f) = (f^2 - f_s^2)(f^2 - f_g^2) - 4\zeta_s \zeta_g f_s f_g f^2 (1 - \sigma^2) ,$$

$$I(f) = 2ff_g \zeta_g (f_s^2 - f^2) + 2ff_s \zeta_s (f_g^2 - f^2) ,$$

$f_s, f_g$  = natural frequencies of seismometer and galvanometer, respectively,

$\zeta_s, \zeta_g$  = damping coefficients of seismometer and galvanometer respectively,

and

$$\sigma^2 = \text{coupling factor.}$$

Note that (2.4) differs in sign from the usual expression given by Hagiwara (1958).

This convention is chosen so that a positive input pulse into the system will

result in an output which has an initial positive going pulse, followed by an overshoot.

To synthesize the response of a WWSSN 15-100 seismograph system with peak magnification of 3000, the instrumental constants given by Chandra (1970) were used. The appropriate constants are  $K = 2350$ ,  $f_s = 1/15$ ,  $f_g = 1/100$ ,  $\zeta_s = 0.93$ ,  $\zeta_g = 1.00$ , and  $\sigma^2 = 0.204$ .

To synthesize the outputs of the seismograph system described by (2.4) for arbitrary inputs, a discrete Fourier transform is used. If  $N$  points of a time function  $h(t)$  are sampled at an interval of  $\Delta t$  seconds, then the approximation to the Fourier transform is

$$H(n\Delta f) = \Delta t \sum_{n=0}^{N-1} h(k\Delta t) \exp(-2\pi ink/N) \quad (2.5)$$

for  $n = 0, N - 1$  and

$$\Delta f = 1/N\Delta t$$

The corresponding discrete inverse Fourier transform is

$$h(k\Delta t) = \Delta f \sum_{n=0}^{N-1} H(n\Delta f) \exp(+2\pi ink/N) \quad (2.6)$$

for  $k = 0, N - 1$ .

In applying the discrete Fourier transform, a Fast Fourier Transform described by Brenner (1967) was used. Care must be taken in applying (2.5) and (2.6) to minimize the effects of aliasing in the frequency domain and truncation in the time domain. For the synthesis of a time domain function using (2.6), one also has to worry about the effects of windowing the spectra

through the choice of  $\Delta t$  . These particular properties of the discrete Fourier transform are described in detail by Brigham (1974).

Because of the windowing effects, some special steps must be taken in order to obtain the impulse response of the system, e.g., the best numerical approximation to  $h(t)$  . The windowing effect arises for the following reason: the number of frequencies sampled by the inverse discrete Fourier transform is finite. The highest frequency sampled is the Nyquist frequency  $f_n = \frac{1}{2}\Delta t$  . This sampling is equivalent to passing the original spectrum through a rectangular window. To see the effect on the approximation to the impulse response, consider the following Fourier transform pair:

$$g(t) = \frac{\sin 2\pi f_0 t}{t} \begin{cases} 1 |f| < f \\ 0 |f| > f_0 \end{cases} \quad G(f) = \frac{1}{2}|f| = f^0$$

Windowing in the frequency domain is equivalent to convolving  $g(t)$  with  $h(t)$  in the time domain. If  $h(t)$  has any sharp changes as a function of time, then  $g(t) * h(t)$  will have a Gibb's phenomenon type of noise present at that time.

To avoid this type of numerical noise, an approximation to the impulse function which minimizes the discontinuities in the frequency domain near the Nyquist frequency is used. Instead of defining the discrete impulse function as  $x(k\Delta t) = 0$  for  $k \neq k_j$  and  $x(k_j\Delta t) = 1/\Delta t$  , use the following function as input to the system:

$$\begin{aligned} x(k_{j-1}\Delta t) &= (1/4\Delta t) \\ x(k_j\Delta t) &= (1/2\Delta t) \\ x(k_{j+1}\Delta t) &= (1/4\Delta t) \end{aligned} \quad (2.7)$$

for some  $k_j$  and

$$x(k\Delta t) = 0$$

elsewhere. Both functions are such that the area under the pulse is unity, however the first definition using a single sample point has a flat spectrum in the frequency domain, while the second, triangular pulse, has a zero in the frequency domain at the Nyquist frequency and is a smoothly varying function between  $f = 0$  and  $f = f_N$ . Thus while (2.7) does not have the desired spectral properties of the impulse function for all frequencies, it provides a suitable approximation to the impulse function at low frequencies and also eliminates the Gibb's phenomenon effects in the synthesized pulses.

Figure 2.13 shows the results of using these numerical techniques to obtain the response of the WWSSN 15-100 seismograph to various inputs. Because the 15-100 WWSSN seismograph has significant response at high frequencies, the response to an impulse in ground displacement begins very sharply. It is theoretically possible to obtain the response of the system to an impulse in displacement by taking the third derivative of the response of the system to a step acceleration. Because of the sharpness of the response to an impulse in displacement, it would seem that one must know the exact nature of the first few seconds of the step acceleration response very accurately before attempting the numerical differentiation. Any noise on an observed trace would make this requirement difficult to satisfy.

The SRO System. The SRO (Seismic Research Observatory) seismograph is a newly developed digital seismograph system. It consists of a short-period force balance accelerometer and associated electronic filtering shaped for short- and long-period responses. Long period recording is digitally on magnetic tape with a sample taken every second. Since the system is still

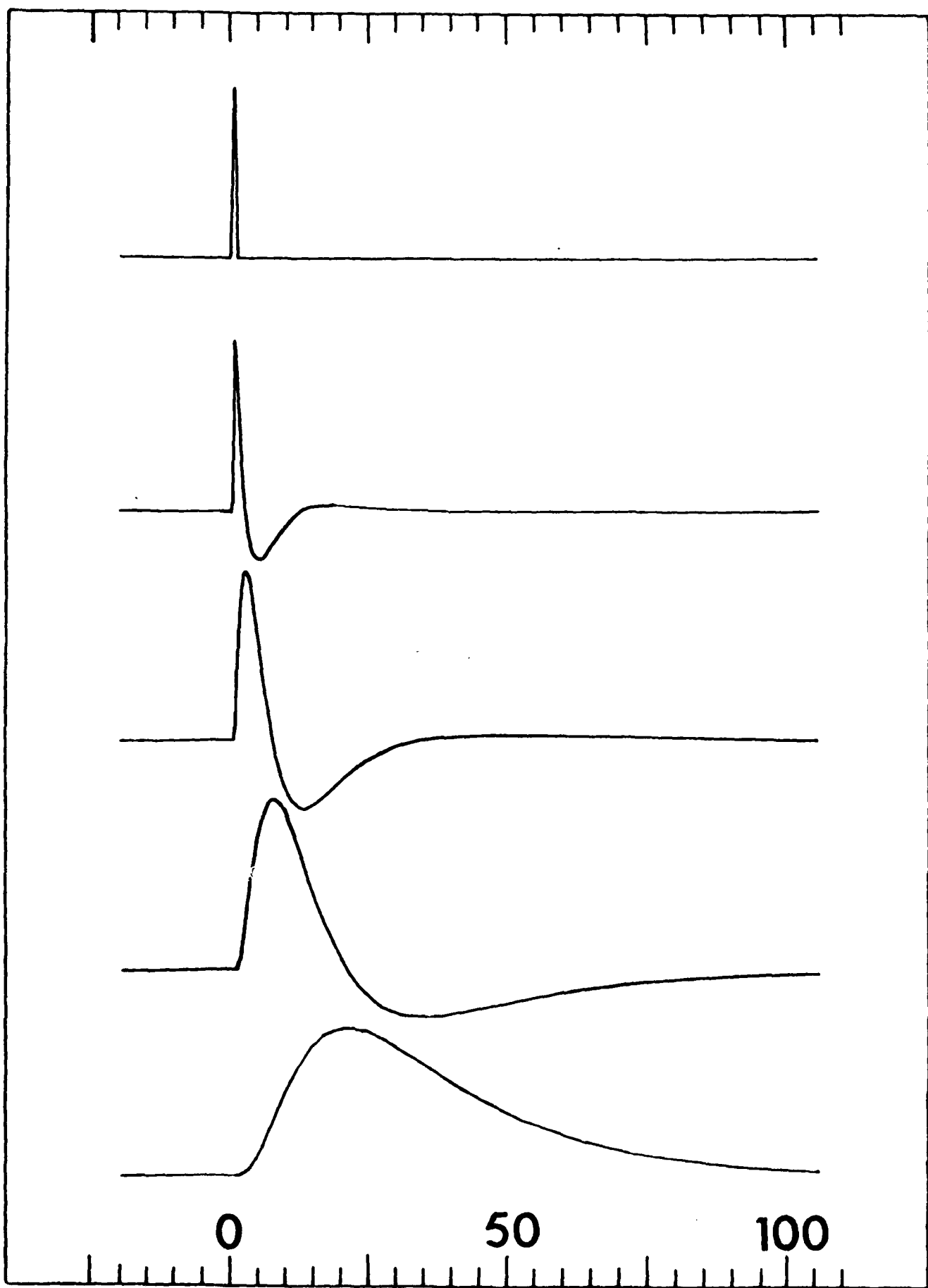


Figure 2.13

Figure 2.13: Response of WWSSN 15-100 long period seismograph to various inputs. From top to bottom: numerical impulse used based on (2.4); response to an impulse in ground displacement; response to an impulse in ground velocity; response to an impulse in ground acceleration; and response to a unit step in ground acceleration. Time scale is in seconds.

relatively new, it is appropriate to attempt an instrument calibration and to discover deficiencies in data, so as to indicate improvements that should be made to the calibration technique to provide necessary information.

Figure 2.14 shows a representative calibration response of the system. A step acceleration was applied to the system during normal operation at time  $t = 0.0$  seconds. The time coordinate is in units of seconds, while the amplitude coordinate is in units of digital counts. The step acceleration response is characterized by an initial upward displacement, followed by a negative overshoot, followed by a very small positive overshoot. Note the presence of background noise on the calibration pulse. This noise will obliterate much of the desired information about the impulse response of the system.

The work of many authors indicates that it is very difficult to obtain adequate high frequency information concerning the amplitude and phase response of a system by the application of Fourier analysis to the step acceleration output pulse. Figure 2.15 shows the amplitude of the Fourier transform of the step acceleration response. Even though particular calibration pulse used was not as noisy as the one plotted in Figure 2.14, information seems to deteriorate above the frequency of 0.05 Hz. The amplitude of the desired impulse response  $H(f)$  as determined by differentiating the step acceleration responses three times is plotted in Figure 2.16. Data at frequencies greater than 0.1 Hz were not plotted, since the results begin to show scatter near 0.07 Hz. The derived phase response also shows scatter at these high frequencies.

At this point, we are hampered by a limited knowledge of the frequency response of the system. To obtain the desired impulse response, some assumptions will have to be made later concerning the amplitude and phase response of the system at high frequencies, and it would be good to see if we can establish some time domain constraints along the way.

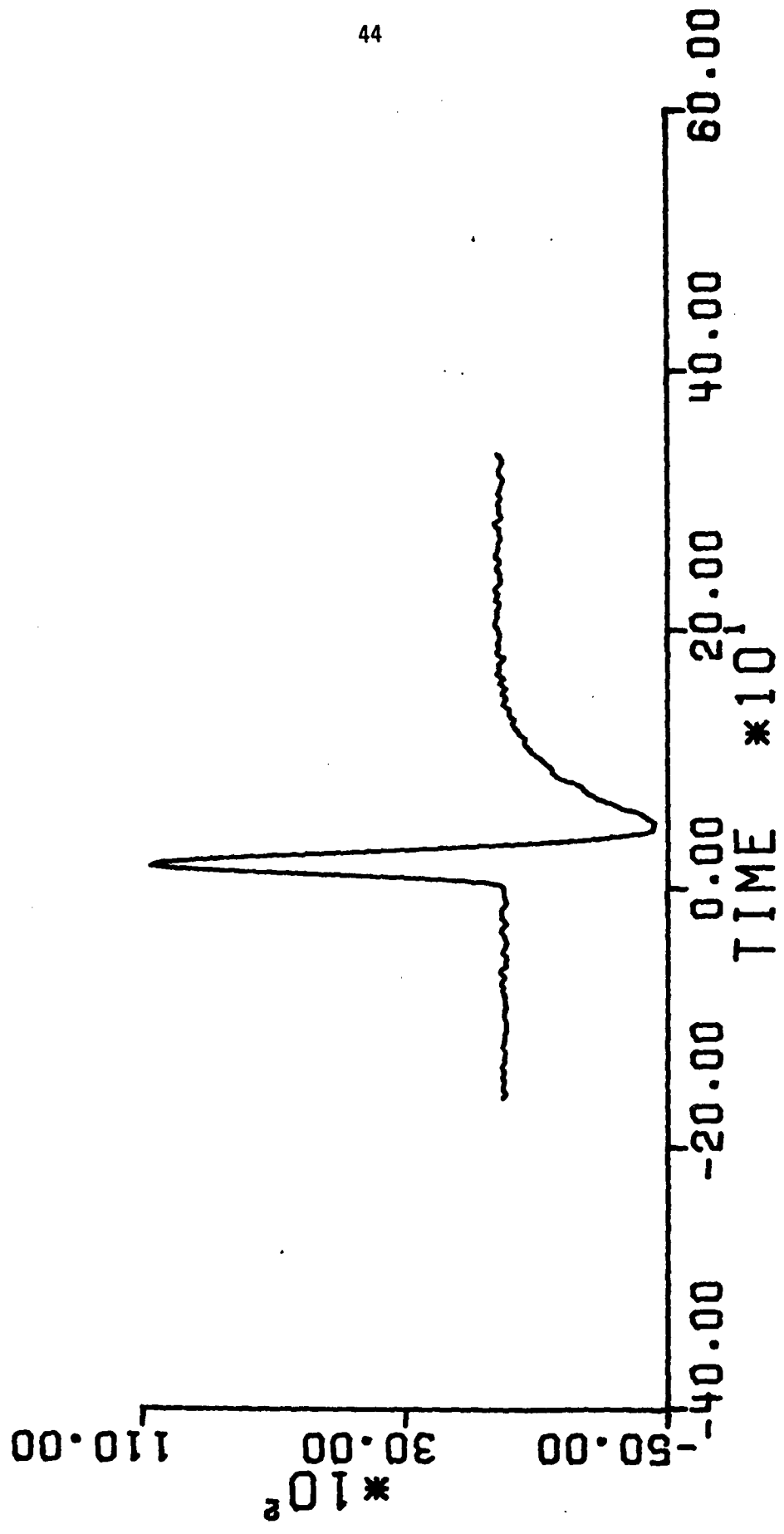


Figure 2.14: Typical recorded response of SRO to a step acceleration calibration pulse.

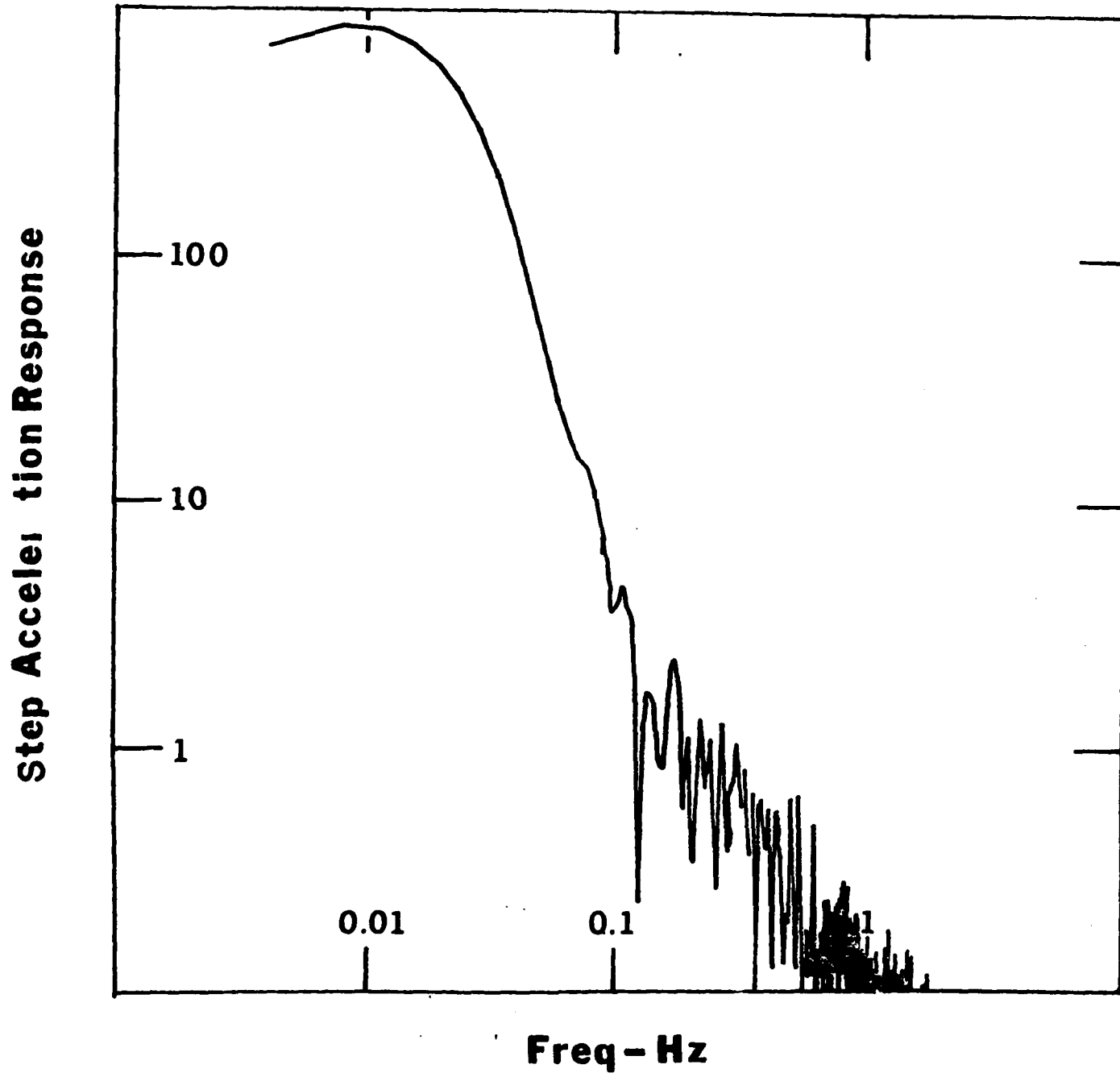


Figure 2.15: Fourier amplitude spectrum of the step acceleration response of the SRO system.

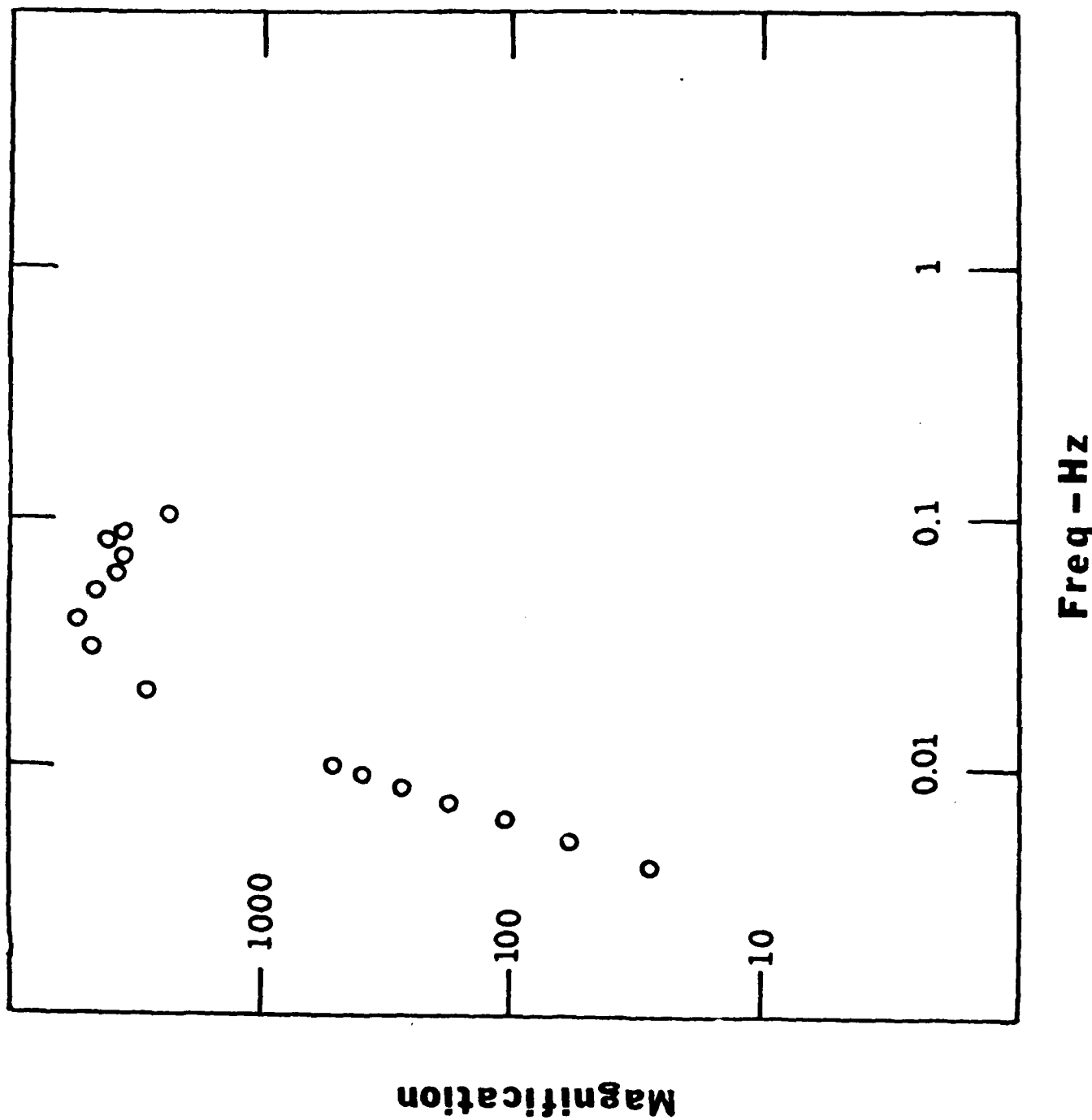


Figure 2.16: Instrument magnification of SRO as computed from step acceleration response of Figure 2.15.

Figure 2.17 shows the results of applying the first, second and third time derivatives to the step acceleration response. These derivatives should represent the response of the system to impulses in ground acceleration, velocity, and displacement. To perform the differentiation, a cubic spline was fit to the calibration pulse of Figure 2.14, with a node every second. The coefficients of the cubic spline fit to the calibration pulse can be used to determine the first, second and third derivatives at each node. A characteristic of this type of polynomial curve fitting is that the second derivative varies linearly between nodes, while the third derivative varies discontinuously between nodes.

In Figure 2.17, the bottom trace is the third derivative and does not provide much information concerning the impulse response of the system,  $h(t)$ , because of the noise. This is the time domain effect of the scatter in the frequency domain at high frequencies evident in Figure 2.15.

Some improvement to the estimate of  $h(t)$  can be obtained by sampling the step acceleration response at a greater time interval. Such an approach is in actuality a filtering operation and care must be taken so that the filtering does not affect the results. Figure 2.18 shows the results of sampling every 4 seconds instead of every 1 second. The nature of the response to an impulse in ground displacement,  $h(t)$ , is becoming clearer. However, the estimated  $h(t)$  lacks the smoothness and detail required for synthesis of theoretical seismograms.

At this point, let us return to what is known of the amplitude and phase response of the SRO seismograph system. Through an analysis of the step acceleration response and the response of the system to harmonic accelerations, the USGS Albuquerque Seismological Center was able to provide a fairly accurate determination of the amplitude and phase response of the system from about

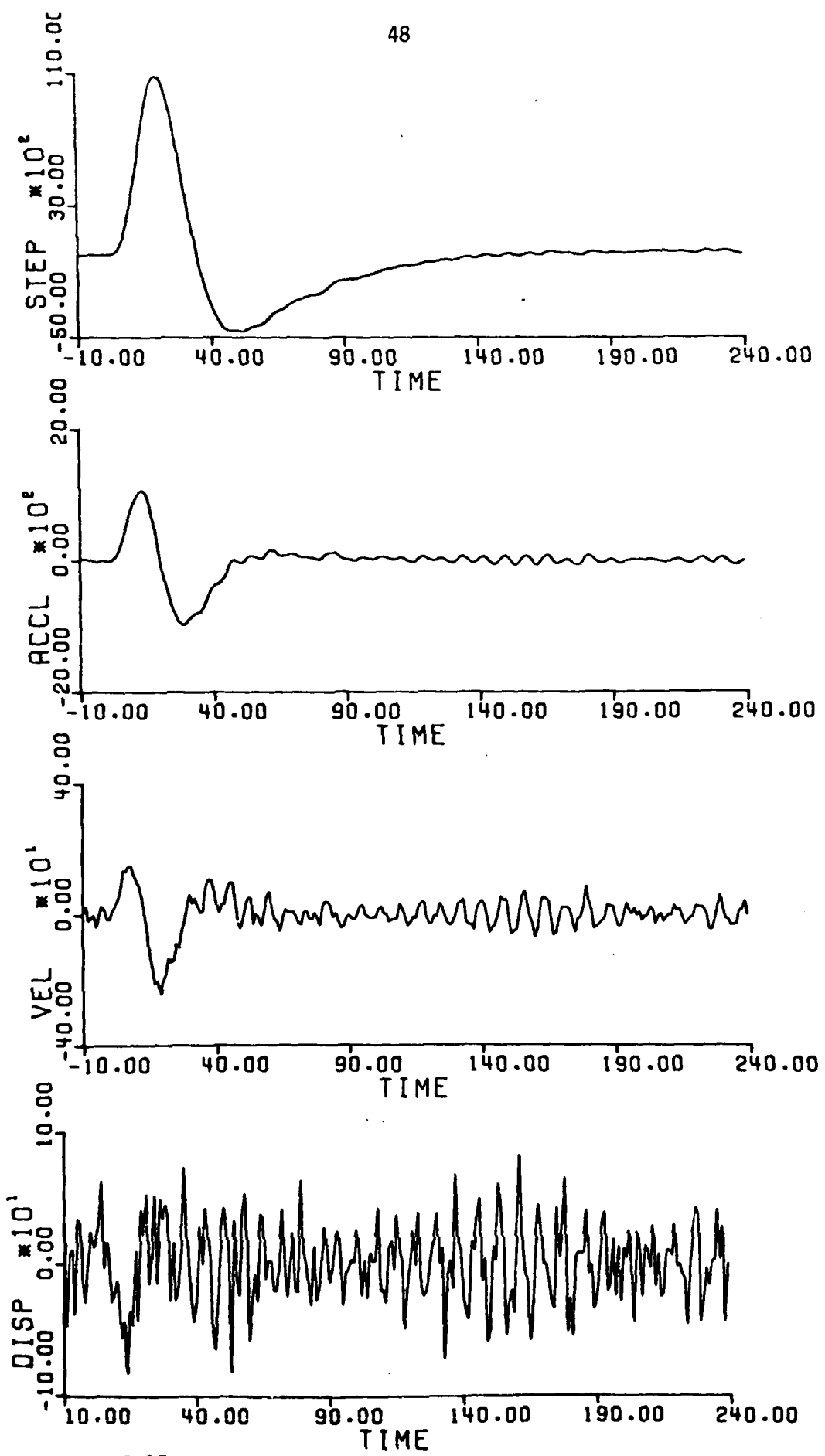


Figure 2.17

Figure 2.17: Direct estimation of SRO system impulse response by numerical differentiation of calibration pulse. Data samples taken every 1.0 second. Traces from top to bottom: digitized system response to step acceleration; estimated response to impulse in ground acceleration; estimated response to impulse in ground velocity; estimated response to impulse in ground displacement. The time scale is in seconds,  $t = 0$  is the time of application of the step acceleration.

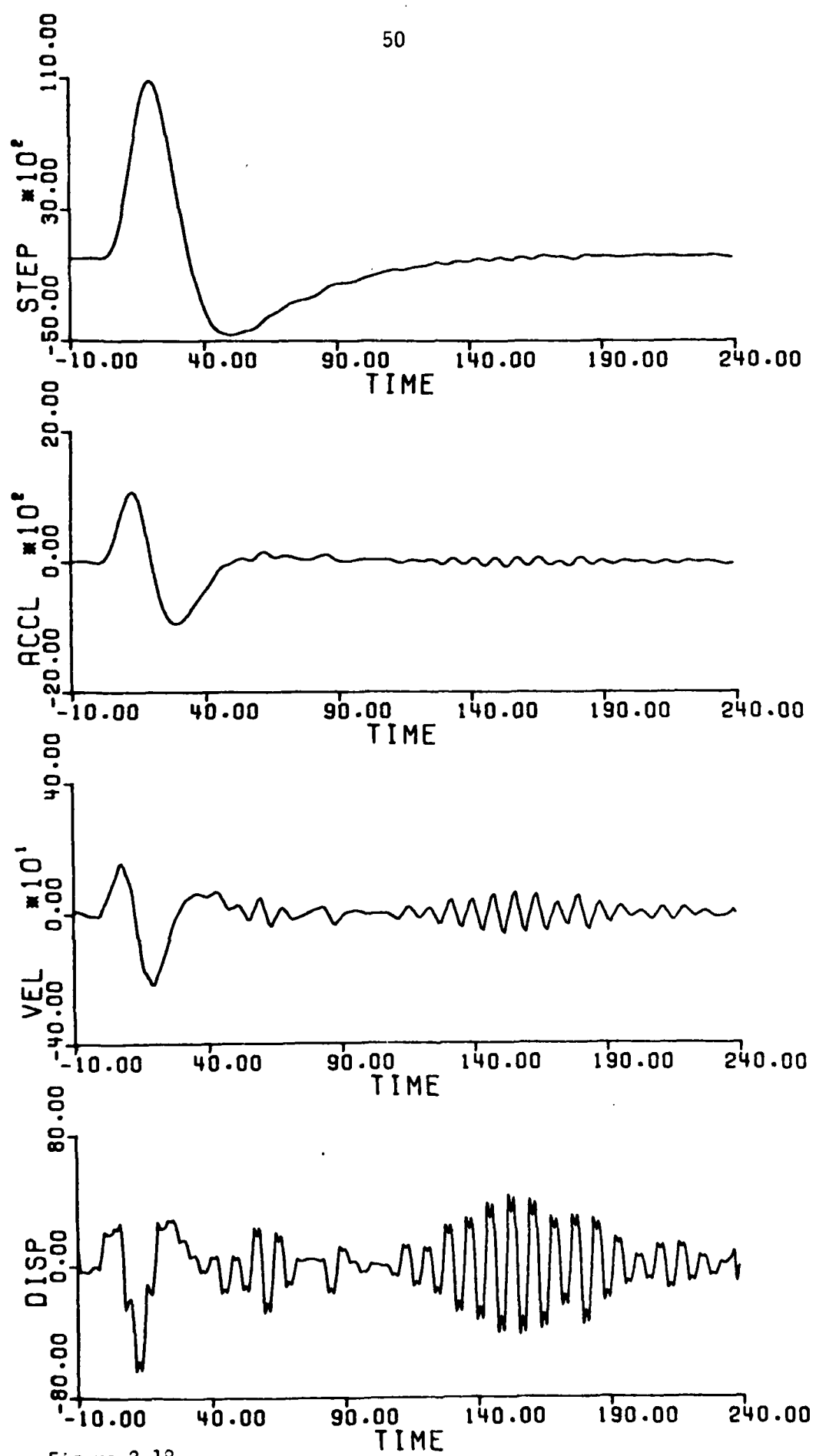


Figure 2.18

Figure 2.18: Estimation of SRO impulse response by numerical differentiation of calibration pulse. Data samples taken every 4.0 seconds. Trace order is as in Figure 2.17.

0.002 Hz to 0.05 Hz. The amplitude and phase response data so obtained are given by the open circles in Figures 2.19 and 2.20, respectively.

The phase response can be calculated from the amplitude response by a Hilbert transform, as explained in detail in Section 2.1. As is seen from the data points of Figure 2.19 the amplitude response is known over only a limited frequency range. We can, however, make some assumptions concerning the amplitude response. We assume that the amplitude response varies as  $f^4$  at low frequencies, and as either  $f^{-4}$  (curve a),  $f^{-5}$  (curve b),  $f^{-6}$  (curve c), or  $f^{-7}$  (curve d) for frequencies greater than 0.1 Hz. The computed phase responses are plotted in Figure 2.20. The curves designated by the letters a, b, c, and d correspond to the choices made for the high frequency asymptote of the amplitude response in Figure 2.19. From the comparison with the observed phase data, it seems that curve d, or the  $f^{-7}$  high frequency amplitude response asymptote, gives the best agreement to the phase data. Because of the Hilbert transform relationship, the phase angle at 0.05 Hz, for example, is dependent upon the nature of the amplitude response at frequencies greater than 0.1 Hz. Thus the known amplitude and phase information over a certain frequency range lay some constraints on the nature of the amplitude and phase response outside this particular frequency range if the system is to be minimum-phase causal.

One might be tempted to stop at this point and accept curves d for the amplitude and phase response of the system. However from Figure 2.16 there may be some error in the amplitude response at 0.1 Hz at which the various high frequency asymptotes were drawn. Thus, to settle the choice of the proper curves, a time domain comparison should be made between an observed step acceleration response and the computed step acceleration responses for the four response curves.

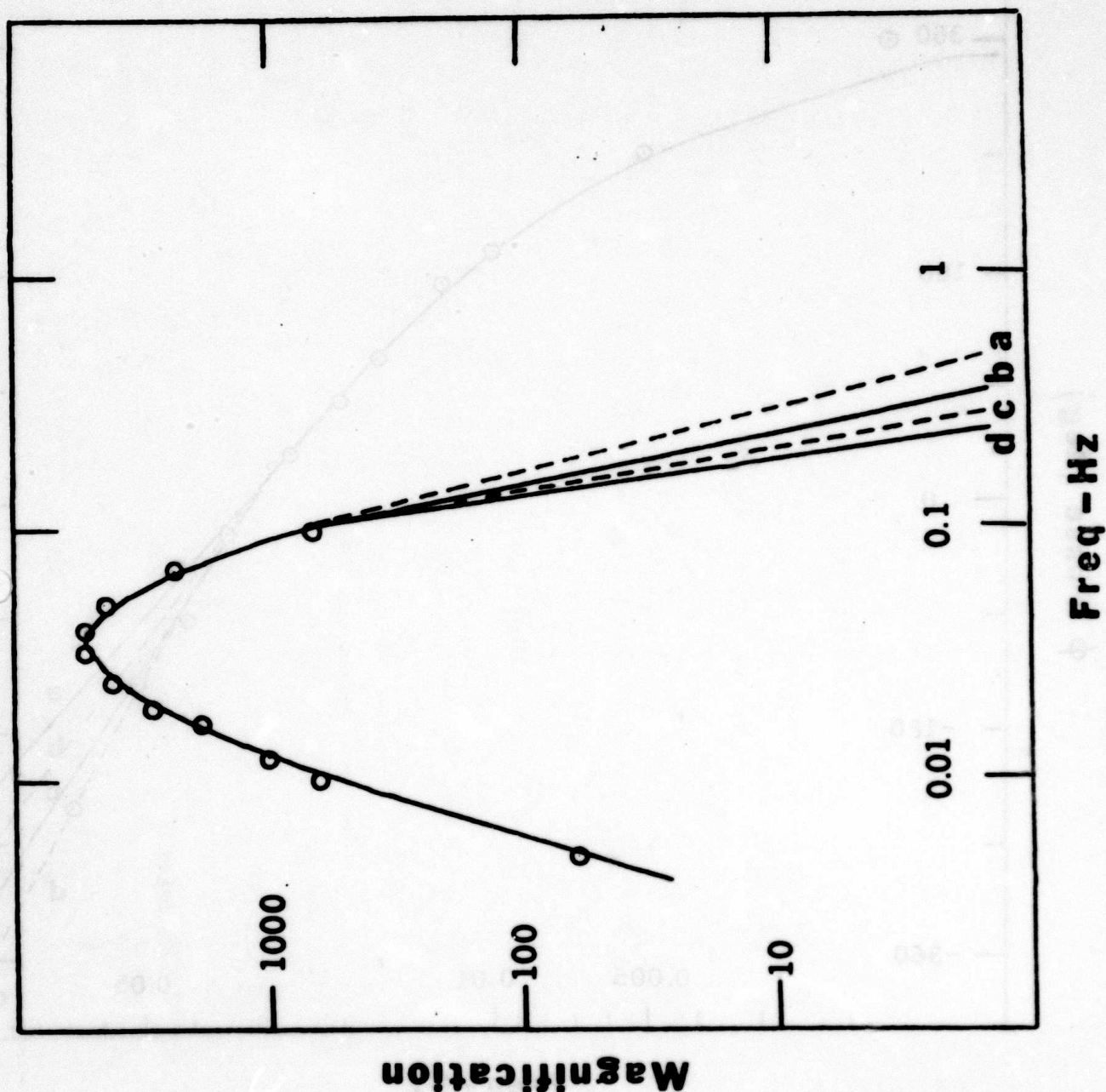


Figure 2.19: SRO amplitude response (open circles) as provided by USGS. The solid and dashed curves are the shapes of the assumed amplitude response for use in the determination of the phase response.

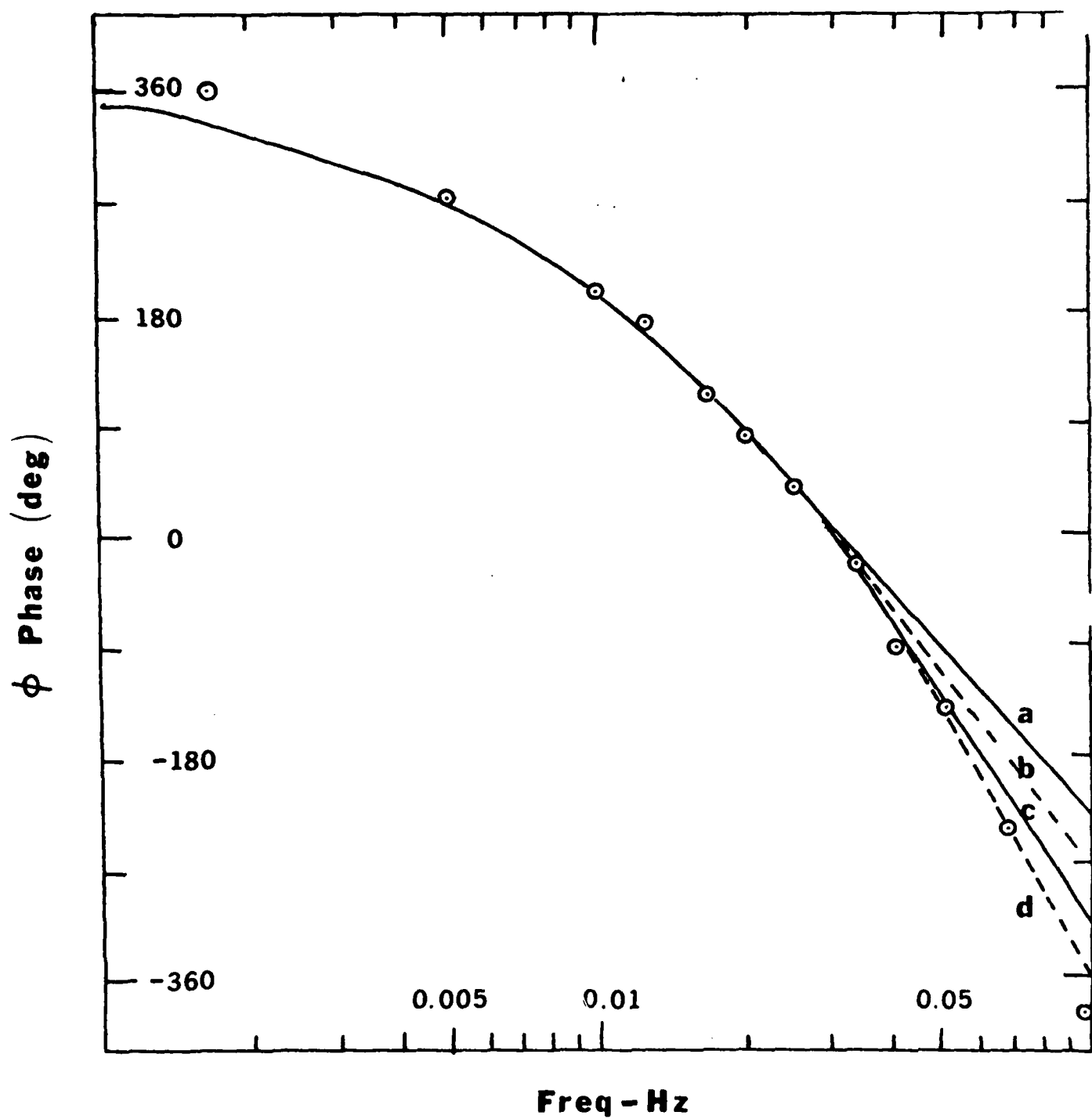


Figure 2.20: SRO phase response (open circles) as determined by the USGS. The solid and dashed curves are the theoretical Hilbert-transform determined phase responses obtained by the respective amplitude responses of Figure 2.19.

The technique of computing the theoretical responses is the same as that used to obtain the WWSSN response of Figure 2.13. Let  $A(f)$  be an amplitude value taken from a particular curve in Figure 2.19 and let  $\theta(f)$  be the phase response from the corresponding curve in Figure 2.20. The system transfer function is defined as

$$H(f) = A(f) \exp(i\theta(f))$$

Figure 2.21 compares the observed step acceleration response of the SRO system to those computed using the various high frequency responses. In this figure, the vertical tic on the trace represents the time of application of the acceleration step, and the letters correspond to the letters used in Figures 2.19 and 2.20. Note that all the responses are very similar. In fact, they all superpose after a time shift. This is because the step acceleration emphasizes the low frequency content and because the phase response acts linearly at high frequencies. Recall that a time shift in a signal is accompanied by a linear phase shift. By considering the time delays, it seems that trace a, corresponding to the  $f^{-4}$  high frequency asymptote gives the best agreement between the observed and predicted step acceleration responses.

Figure 2.22 shows the computed responses of the system to an impulse in ground displacement, the desired  $h(t)$ . Note that all responses are similar, differing only in the time shift from the application of the impulse. The scaling numbers indicate that the relative amplitudes of the signals are also very similar. A comparison of Figure 2.22 with the estimated displacement impulse response of the bottom curve of Figure 2.18, shows that the time domain derivative estimate agrees very well with the synthetics achieved through the Hilbert transform technique. This demonstrates that time domain

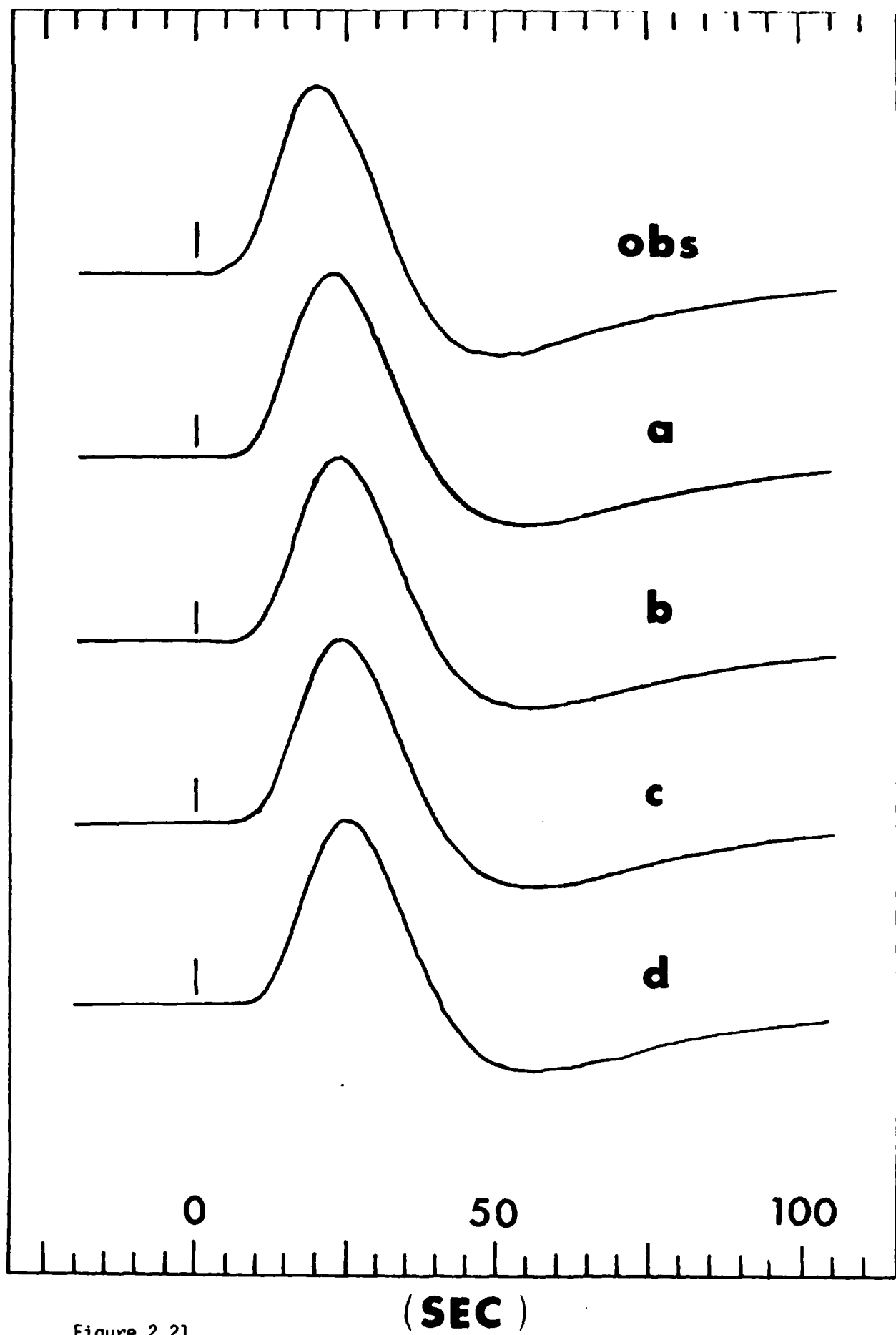


Figure 2.21

Figure 2.21: Comparison of observed and predicted step acceleration responses of the SRO system. The letters refer to the particular amplitude response (Figure 2.19) and phase response (Figure 2.20).

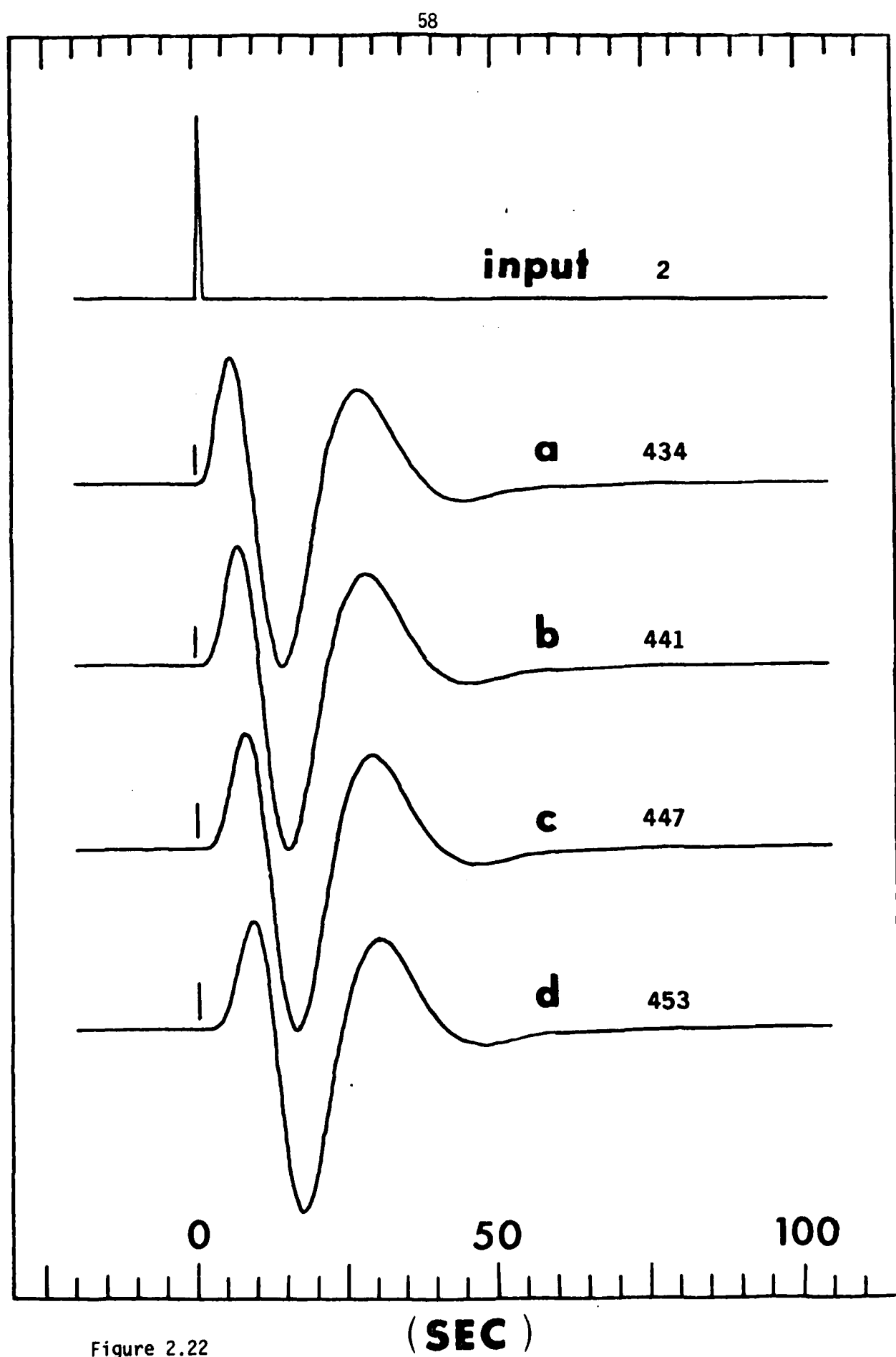


Figure 2.22

Figure 2.22: Computed response of SRO to an impulse (top trace) in ground displacement for each of the four amplitude and phase responses considered.

differentiation can be used to estimate the shape of the displacement impulse response. It also shows that the other derivatives can be used as constraints upon the synthesized responses to impulses in ground velocity and acceleration.

On the basis of agreement in the time shift, curve a ( $f^{-4}$ ) is preferred to curve d ( $f^{-7}$ ) even though there is some discrepancy in the phase responses. But as mentioned above, the discrepancy in the phase responses may also be due to errors in the amplitude response given between 0.05 and 0.1 Hz. Figure 2.23 presents the computed responses of the SRO system to various inputs.

Discussion. This paper has dealt with the practical aspects of obtaining the response of a seismograph system to an impulse in ground displacement, with particular emphasis on the SRO long period system. Spectral analysis of the step acceleration calibration pulse, or equivalent time domain operations cannot provide adequate estimates of the system impulse response at all frequencies because of errors in digitizing and because of noise present in the signal, and the enhancement of the high frequency content of the calibration pulse. The use of the Hilbert transform technique with the band limited amplitude and frequency response data results in a reasonable determination of the system impulse response, when constrained by the time domain data.

With respect to the specific SRO system, efforts should be made to obtain better information on the amplitude and phase response at frequencies greater than 0.05 Hz. The acquisition of this added information might be made possible by sampling at a rate faster than 1 sample per second when calibrations are being performed. This is very important in phase determinations, since a one second sampling interval means that there is up to a  $\pm 0.5$  second error in determining the time of application of the calibration step acceleration.

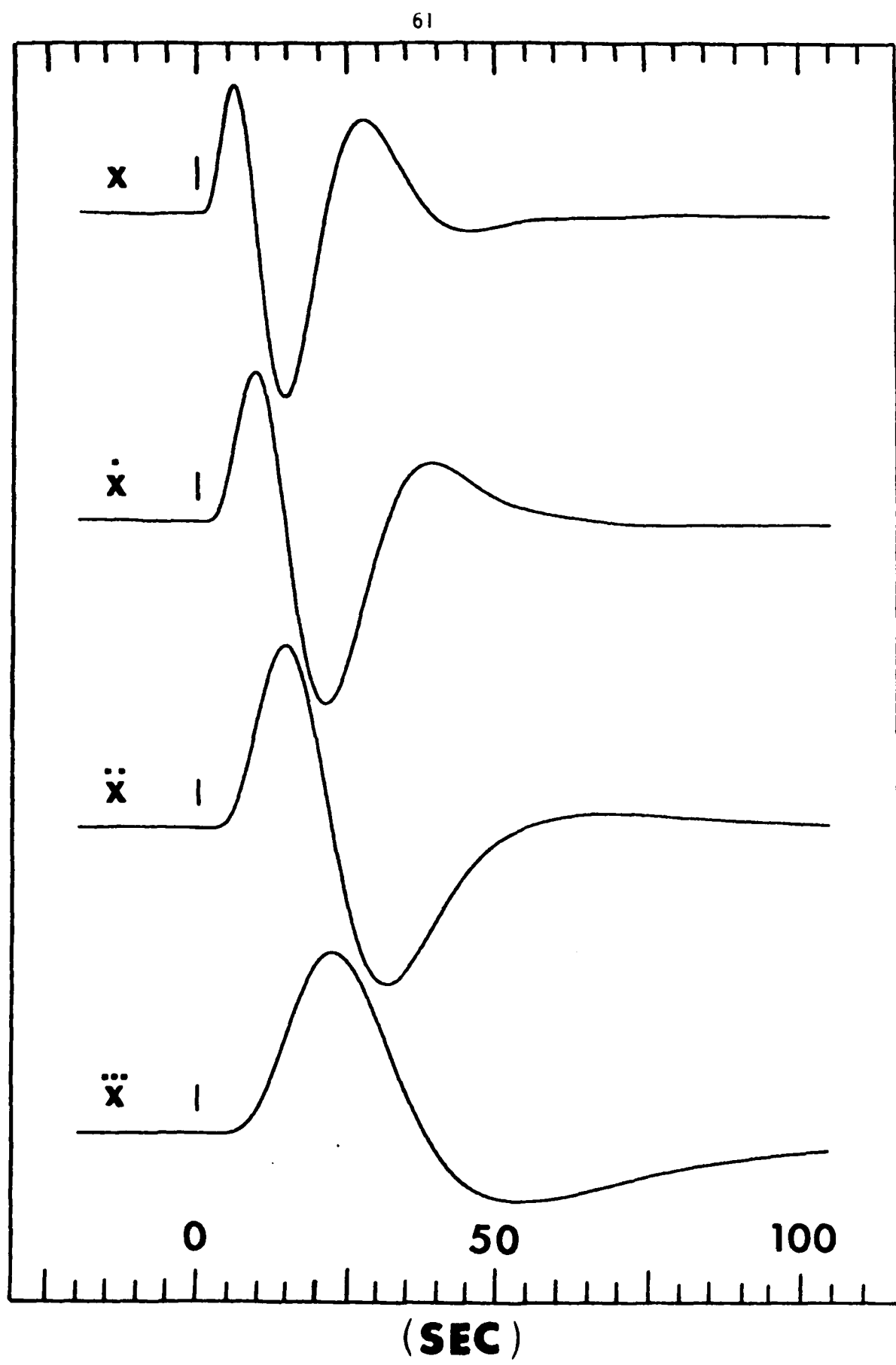


Figure 2.23

Figure 2.23: Responses of SRO system with response curve 'a' to various inputs. Traces from top to bottom: response to an impulse in ground displacement; response to an impulse in ground velocity; response to an impulse in ground acceleration; and response to a step in ground acceleration.

This timing error translates into a  $\theta = \pm (0.5 f) 360^\circ$  phase error, or about  $18^\circ$  at  $f = 0.1$  Hz.

References

Bakun, W. H. and J. Dratler (1976). Empirical transfer functions for stations in the central California seismological network, preliminary version, U.S.G.S. open-file report, Menlo Park, California.

Berg, E. and D. M. Chesley (1975). Automated high-precision amplitude and phase calibration of seismic systems, unpublished manuscript.

Bolduc, P. M., R. M. Ellis, and R. D. Russell (1972). Determination of the seismograph phase response from the amplitude response, Bull. Seism. Soc. Am., 62, 1665-1672.

Brenner, N. M. (1967). Three Fortran Programs that Perform the Cooley-Tukey Fourier Transform, Technical Note 1967-2, Lincoln Laboratory.

Brigham, E. O. (1974). The Fast Fourier Transform. Prentice-Hall, Inc., Englewood Cliffs.

Chandra, U. (1970). Analysis of body-wave spectra for earthquake energy determination, Bull. Seism. Soc. Am., 60, 539-563.

Forbes, C. B., R. Obenchain, and R. J. Swain (1965). The LASA sensing system design, installation and operation, Proc. IEEE, 53, 1834-1843.

Holcomb, L. G. (1975). Amplitude and phase response (LP), calibrated on 9 December 1975; and relative SP response to ground displacement, calibrated on 29 August 1975.

Hagiwara, T. (1958). A note on the theory of the electromagnetic seismograph, Bull. Earthq. Res. Inst., Tokyo, 36, 139-164.

Helmburger, D. V., and S. D. Malone (1975). Modeling local earthquakes as shear dislocations in a layered half space, J. Geophys. Res., 80, 4881-4888.

Jarosch, H. and A. R. Curtis (1973). A note on the calibration of the electromagnetic seismograph, Bull. Seism. Soc. Am., 63, 1145-1155.

Kisslinger, C. (1971). Seismological Instrumentation, Internat. Inst. Seis. Earthquake Engi., Tokyo, Japan.

Mitchell, B. J. and M. Landisman (1969). Electromagnetic seismograph constants by least-squares inversion, Bull. Seism. Soc. Am., 59, 1335-1348.

Willmore, P. L. (1960). The detection of earth movements, Methods and Techniques in Geophysics, John Wiley & Sons, New York.

3. A Resolving Criterion for Band-Limited Filtration

P. C. Luh

An exact expression for the envelopes, devoid of sinusoidal oscillations, of non-dispersive seismic signals which have been passed through a Gaussian filter in the frequency domain has been derived. The object is to examine the effectiveness of band-limited filtration alone to discriminate multiple events within a short duration and to differentiate different body-wave phases. Attention is focused on non-dispersive signals because body waves are generally non-dispersive and because such signals are easy to manipulate analytically. Gaussian filters are studied because evaluation of an integral is simplified and because results for a Gaussian filter should be extendible to other forms of band-limited filters that do not introduce a ringing effect in filtered signals in the time domain.

Analytic calculations assume that the Taylor series expansion of a real amplitude factor of a seismic signal uniformly converges everywhere in the frequency domain and that the signals are square integrable. Analytic calculations are effected not to supply a new formula, which incidentally is not suitable for numerical application, but to provide a better picture of where the envelope's relative maxima are located in relation to theoretical group arrivals of various phases.

The most important result is a criterion of resolvability when using band-limited filtration for discriminating multiple arrivals or multiple phases. This criterion easily follows from an analytic consideration in terms of an infinite series, in addition to incorporating Rayleigh's criterion in optics.

The motivation behind expressing the filtered signal in an infinite series is that, in effecting narrow-band filtration, one almost without exception

retains only the first-order term and claims group arrivals of phases at the envelope's relative maxima (Archambeau and Flinn, 1965). Such an approximation is acceptable only if a filter is indeed very narrow. But if a filter is not sufficiently narrow, one must clearly go to higher-order terms. It turns out that for non-dispersive signals, one can easily express higher-order terms analytically when using a Gaussian filter.

The resolvability criterion is tested by using cusp-shaped filters on seismic data from Adak stations as well as from the Florissant test site (the latter data due to Kisslinger, et al., 1963). Numerical results generally confirm the criterion. Some results from applying very broad-band filters are also shown because they exhibit some interesting features.

### 3.1 Resolvability Criterion for Relative Maxima of Envelope.

For simplicity, let a Fourier-transformed seismic signal be composed of only one phase, so that the signal at a receiver, a propagation distance  $r$  away from a source, is

$$S(\omega, r) = A(\omega, r) \exp\{i[\kappa(\omega) r + \phi(\omega)]\}$$

where  $A$ ,  $\kappa$  and  $\phi$  are respectively real amplitude factor, angular wave number and initial phase at the source. Let a Gaussian filter whose narrowness is characterized by  $\alpha$  be

$$G(\omega, \alpha) = \sqrt{\frac{\alpha}{\pi}} \exp(-\alpha\omega^2)$$

Then the filtered signal in the time domain (with a Gaussian filter centered at  $(\omega_0)$  is

$$\begin{aligned}
 F(t; \omega_0, \alpha) &= \frac{1}{2\pi} \int_{-\infty}^{\infty} G(\omega - \omega_0; \alpha) S(\omega, r) e^{i\omega t} d\omega \\
 &= \frac{e^{i\omega_0 t}}{2\pi} \int_{-\infty}^{\infty} G(\omega; \alpha) A(\omega + \omega_0, r) e^{i\psi(\omega, t)} d\omega
 \end{aligned}$$

where  $\psi(\omega, t) = \omega t - \kappa(\omega + \omega_0) r - \phi(\omega + \omega_0)$ . Provided  $A(\omega, r)$  and  $\psi(\omega, t)$  belong to class  $\mathcal{C}^\infty$  (vector space of infinitely differentiable functions) with respect to  $\omega$ , and provided Taylor series of  $A(\omega, r)$  uniformly converges for every  $\omega$ , then if  $G(\omega - \omega_0; \alpha) S(\omega, r)$  is square integrable,

$$\begin{aligned}
 F(t; \omega_0, \alpha) &= \frac{e^{i\omega_0 t}}{2\pi} \int_{-\infty}^{\infty} G(\omega; \alpha) \sum_{j=0}^{\infty} \frac{A^{(j)}(\omega_0, r)}{j!} \omega^j e^{i\psi(\omega, t)} d\omega \\
 &= \frac{e^{i\omega_0 t}}{2\pi} \sum_{j=0}^{\infty} \frac{(-i)^j A^{(j)}(\omega_0, r)}{j!} \frac{\partial^j}{\partial t^j} \left[ \int_{-\infty}^{\infty} G(\omega; \alpha) e^{i\psi(\omega, t)} d\omega \right]
 \end{aligned}$$

where

$$A^{(j)}(\omega_0, r) = \left[ \frac{\partial^j A(\omega, r)}{\partial \omega^j} \right]_{\omega=\omega_0}$$

It can be easily shown that non-dispersive signals with  $\phi(\omega)$  also having no higher derivatives than the first order\*,

\*Actually, one can extend to the second order by replacing  $\alpha$  by  $\alpha - \frac{i}{2} \left[ \frac{\partial^2 \psi}{\partial \omega^2} \right]_{\omega=0}$

$$\int_{-\infty}^{\infty} G(\omega, \alpha) e^{i\psi(\omega, t)} d\omega = \exp \left\{ - \frac{[\psi'(0, t)]^2}{4\alpha} + i\psi(0, t) \right\}$$

and that after a few algebraic manipulations,

$$\begin{aligned}
 F(t; \omega_0, \alpha) &= \frac{1}{2\pi} \exp \left\{ - \frac{[\psi'(0, t)]^2}{4\alpha} + i[\omega_0 t + \psi(0, t)] \right\} \sum_{j=0}^{\infty} i^j \\
 &\cdot A^{(j)}(\omega_0, r) \sum_{k=0}^{j'} \frac{(-)^k}{k! (j-2k)!} \left( \frac{1}{4\alpha} \right)^k \left[ \frac{\psi'(0, t)}{2\alpha} \right]^{j-2k} \\
 &= \frac{1}{2\pi} \exp \left\{ - \frac{[\psi'(0, t)]^2}{4\alpha} + i[\omega_0 t + \psi(0, t)] \right\} \sum_{j=0}^{\infty} \left( \frac{1}{4\alpha} \right)^j \\
 &\cdot \sum_{k=0}^{j'} \frac{i^k}{k! (j-k)!} A^{(2j-k)}(\omega_0, r) [2\psi'(0, t)]^k \quad (3.1)
 \end{aligned}$$

where  $\psi'$  indicates a partial derivative with respect to  $\omega$ , and  $j' = \left[ \frac{j}{2} \right]$  (or the largest integer no larger than  $\frac{j}{2}$ ).

In general, if a signal is composed of  $N$  different non-dispersive phases,

$$\begin{aligned}
 F(t; \omega_0, \alpha) &= \frac{1}{2\pi} \sum_{p=1}^N \exp \left\{ - \frac{[\psi_p'(0, t)]^2}{4\alpha} + i[\omega_0 t + \psi_p(0, t)] \right\} \sum_{j=0}^{\infty} \left( \frac{1}{4\alpha} \right)^j \\
 &\cdot \sum_{k=0}^{j'} \frac{i^k}{k! (j-k)!} A_p^{(2j-k)}(\omega_0, r) [2\psi_p'(0, t)]^k \quad (3.2)
 \end{aligned}$$

where

$$\psi_p'(0,t) = t - t_p \quad \text{with} \quad t_p = \kappa_p(\omega_0) r + \phi_p(\omega_0)$$

Note that  $F$  would oscillate with angular frequency  $\omega_0$  in the time domain if each infinite sum is not overwhelmingly large away from respective  $t_p$ . Suppose  $A$  uniformly converges everywhere in frequency domain, then it can be easily shown that the series would also uniformly converge for every non-zero  $\alpha$ . However, for  $|\alpha| \leq \frac{1}{4}$ , it is not difficult to observe that each infinite sum away from  $t_p$  would in general become too large as well as too complex to obliterate Gaussian envelopes completely. Under such circumstances, equation (3.1), the series representation for  $F$ , would become quite useless.

If a signal is dispersive,  $F$  would be very complicated, but the first few terms in a series expansion are

$$\begin{aligned} F(t; \omega_0, \alpha) = & \frac{1}{2\pi} \sum_{p=1}^N \exp \left\{ -\frac{[\psi_p'(0,t)]^2}{4\alpha} + i \left[ \omega_0 t + \psi_p(0,t) \right] \right\} \\ & \cdot \left\{ A_p^{(0)} + \frac{1}{4\alpha} \left[ A_p^{(1)} + 2i A_p^{(1)} \psi_p^{(0)} + i A_p^{(0)} \psi_p^{(1)} \right] + \left( \frac{1}{4\alpha} \right)^2 \left[ \frac{A_p^{(iv)}}{2} \right. \right. \\ & \left. \left. + 2i A_p^{(1)} \psi_p^{(1)} - A_p^{(1)} (2\psi_p^{(0)} - 3i\psi_p^{(1)}) + 2i A_p^{(1)} (\psi_p^{(1)} + 3i\psi_p^{(0)}) \right. \right. \\ & \left. \left. + \frac{i A_p^{(0)}}{2} (\psi_p^{(iv)} + 4i \psi_p^{(1)} \psi_p^{(0)} - 4\psi_p^{(0)} \psi_p^{(1)} + 3i \psi_p^{(0)}) \right] + \dots \right\} \end{aligned}$$

For reasonably high  $\alpha$ , higher-order terms in  $\frac{1}{4\alpha}$  can be neglected, in which case we obtain the familiar result of

$$A_p^{(0)} \exp \left\{ - \frac{[\psi_p'(0, t)]^2}{4\alpha} + i[\omega_0 t + \psi_p(0, t)] \right\}$$

Envelope of  $F$  without sinusoidal oscillations is simply  $|F|$ . It can be shown that for equation (3.2)

$$|F|^2 = \frac{1}{4\pi^2} \sum_{p,q} \exp \left[ - \frac{(t_p - t_q)^2}{8\alpha} \right] \exp \left[ - \frac{(2t - t_p - t_q)^2}{8\alpha} \right] \sum_{j=0}^{\infty} \frac{c_{j,pq}(t)}{(4\alpha)^j} \quad (3.3)$$

where

$$c_{j,pq}(t) = \sum_{\ell=0}^{j'} \sigma_{j\ell} \sum_{m=0}^{j'} \sum_{n=\max(0, \ell-2m)}^{\min(\ell, j-2m)} \frac{(-)^{\ell+m+n}}{n! (\ell-n)! (j-2m-n)! (2m-\ell+n)!} \cdot \begin{aligned} & \cdot A_p^{(\ell+n)}(\omega_0, r) A_q^{(2j-\ell-2m-n)}(\omega_0, r) [2\psi_p'(0, t)]^{\ell-n} \\ & \cdot [2\psi_q'(0, t)]^{2m-\ell+n} + A_p^{(2j-\ell-2m-n)}(\omega_0, r) A_q^{(\ell+n)}(\omega_0, r) \\ & \cdot [2\psi_p'(0, t)]^{2m-\ell+n} [2\psi_q'(0, t)]^{\ell-n} \end{aligned}$$

with  $\sigma_{j\ell} = 1 + \frac{1}{2}(j-1-2j')\delta_{j'-\ell}$ . Equation (3.3) is an exact expression in terms of an infinite series of the envelope for a non-dispersive signal. Note the terms with modulation factor  $\exp - (t_p - t_q)^2 / (8\alpha)$  for  $p \neq q$  represent interferences between phases  $p$  and  $q$ .

To examine relative maxima of equation (3.3), first let  $\min_{p \neq q} |t_p - t_q|$  be large such that  $|F|^2$  is safely

$$|F|^2 \simeq \frac{1}{4\pi^2} \sum_p \exp \left[ -\frac{(t-t_p)^2}{2\alpha} \right] \sum_{j=0}^{\infty} \frac{c_{j,pp}(t)}{(4\alpha)^j} \quad (3.4)$$

with

$$c_{j,pp}(t) = \sum_{\ell=0}^{j'} 2\sigma_{j\ell} \sum_{m=0}^{j'} \sum_{n=\max(0, \ell-2m)}^{\min(\ell, j-2m)} \frac{(-)^{\ell+m+n}}{n! (\ell-n)! (j-2m-n)! (2m-\ell+n)!} \cdot A_p^{(\ell+n)}(\omega_0, r) A_p^{(2j-\ell-2m-n)}(\omega_0, r) [2\psi_p(0, t)]^{2m}$$

It is easy to note that relative maxima of equation (3.4) occurs exactly at  $\psi_p(0, t) = 0$  (or  $t - t_p = 0$ ) since  $c_{j,pp}(t)$  is made up of polynomials in  $[\psi_p(0, t)]^2$ . For dispersive signals, even if  $\min_{p \neq q} |t_p - t_q|$  is large, relative maxima of  $|F|^2$  due to presence of higher-order derivatives of  $\psi$  would deviate from  $t = t_p$  slightly. Although these two results are trivial and not new, a formal proof of the former based on equation (3.4) has not been given before. Thus, in body-wave phase studies, an envelope's relative maxima, if not greatly interferred with by adjacent phases, are precisely group arrivals.

Again it should be noted that infinite series representation for both equation (3.3) and (3.4) is meaningful only if  $\alpha > \frac{1}{4}$ . Because exponential decay factor is the same, a resolving criterion for multiple arrivals or multiple phases is simply that of Rayleigh's in optics; i.e.

$$\exp \left[ -\frac{(t_p - t_q)^2}{8\alpha} \right] \leq \exp(-1)$$

where exponent of  $-1$  rather than  $-\ln(2)$  is chosen for simplicity. Thus, a criterion of resolvability using Gaussian filtration alone is

$$2 < 8\alpha \leq (t_p - t_q)^2 \quad (3.5)$$

Because  $t_p = \kappa'_p(\omega_0) r + \phi'_p(\omega_0)$  depends on propagation distance  $r$ , inequality (3.5) also implies a minimum radius within which application of band-limited filtration alone to resolve different phase arrivals cannot be as effective as an application to seismic data collected outside that radius. This minimum distance, however, does not apply to multiple events occurring at one place within a short duration, as time separation of a given phase from each event is nearly the same regardless where a station is located relative to the source position.

Success of applying band-limited filtration to resolve phases with  $|t_p - t_q| > \sqrt{2}$  has been amply demonstrated. For example, two recent reports of Systems, Science and Software (S<sup>3</sup>) (1975a, 1975b) show high resolvability of phases as well as multiple arrivals of events. The time separation in these reports is on the order of 10 sec. Although the filter the S<sup>3</sup> group used is cusp-shaped one, the criterion (3.5) should be equally applicable to it as to Gaussian filter, with a slight modification. <sup>†</sup>

---

<sup>†</sup> Let cusp-shaped filter be  $G_c(\omega) = \frac{\pi}{\beta} [1 - \sin(\beta|\omega|)]$  for  $|\omega| < \pi/(2\beta)$  and 0 otherwise. Then its inverse Fourier transform is  $[\frac{\beta}{t} \sin(\frac{\pi t}{2\beta}) - 1]/(\beta^2 - t^2)$  so that half-width is approximately  $\frac{5}{2}\beta$ . Thus,  $|t_p - t_q| > 5\beta$ , or  $(t_p - t_q)^2 > 25\beta^2$ . Hence, without great loss of generality, we can replace  $\alpha$  in inequality (3.5) by  $3\beta^2$  for cusp-shaped filters.

It should be pointed out here that  $[\alpha]$  (dimension of  $\alpha$ ) is  $[T^2]$ . In numerical applications, instead of  $\alpha$ , it is frequently more convenient to set  $\alpha = Q/\omega_0^2$  for the Gaussian filter, where broadness is now characterized by non-dimensional parameter  $Q$ .

### 3.2 Numerical Examples.

Figures 3.1-3.3 show filtered envelopes for vertical, short-period data collected at three different sites (A,B,C) on Adak Island, Alaska. The event is a nuclear explosion, detonated on 28 October 1975. In each figure,  $Q$  and centering frequency  $f_0$  of cusp-shaped filters are printed at left; viz. (10,1), (7.5,1), (5,1) and  $\beta = Q/(6f_0)$ . Amplitudes are all scaled arbitrarily. The previous note indicates that  $|t_p - t_q| > 5Q/(6f_0)$ , so that for three sets of  $(Q, f_0)$  above, resolvable time separation is at least 4 sec. Phases, moreover, seem to arrive at the same time on each figure except more phases are visible for (5,1) filter than for (10,1).

Figures 3.4-3.6 are similar results with (2.5,1), and (1,1) and (0.5,1). The additional peaks that can be seen on these plots are primarily due to more prominent superposition of different phases since half-widths of filters used are broader than those used before. That envelopes correspondingly show increasing complexity or distortion is in accord with the theoretical prediction above, i.e., envelope shapes are becoming more and more distorted as  $\alpha$  becoming smaller and smaller than  $\frac{1}{2}$ . Because  $(Q, f_0)$  for these three figures (at least on the lower two traces) do not satisfy  $5\beta > \sqrt{2}$  and because it would be inappropriate here to associate phase arrivals with relative maxima of envelopes, whose time separation between adjacent relative maxima is generally greater than  $\sqrt{2}$  sec, the criterion of  $(t_p - t_q)^2 > 8\alpha > 2$  or  $|t_p - t_q| > 5\beta > \sqrt{2}$  seems adequately confirmed in order for any satisfactory study of phase identification to take place. Too small an  $\alpha$  or  $\beta$  would

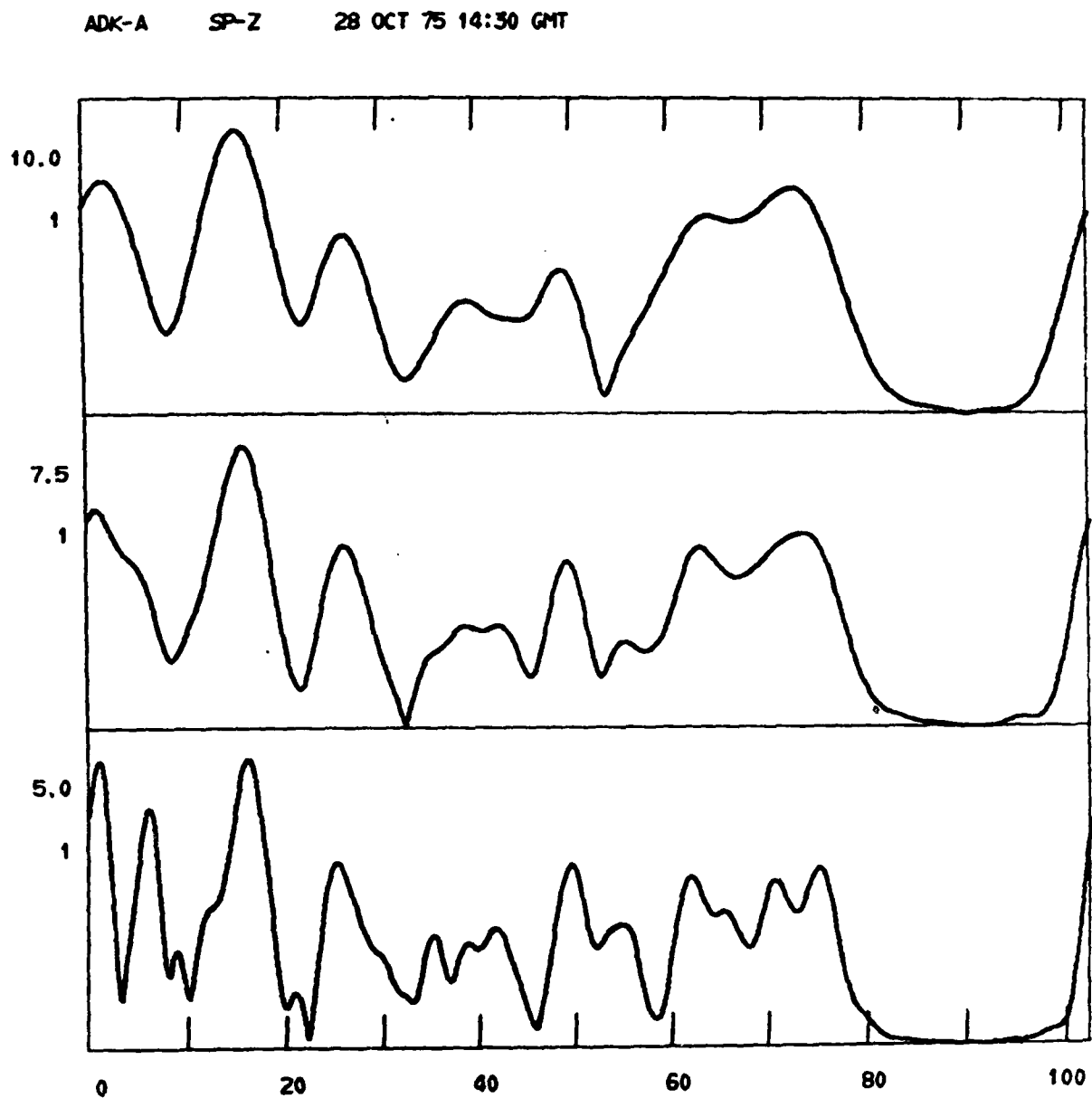


Figure 3.1: Filtered envelopes using  $(Q, f_0) = (10, 1)$ ,  $(7.5, 1)$  and  $(5, 1)$  for SP-Z component record at Adak-A site. The time scale is in seconds;  $t = 0$  corresponds to beginning of digitization. Amplitudes are normalized arbitrarily.

ADK-B SP-Z 28 OCT 75 14:30 GMT

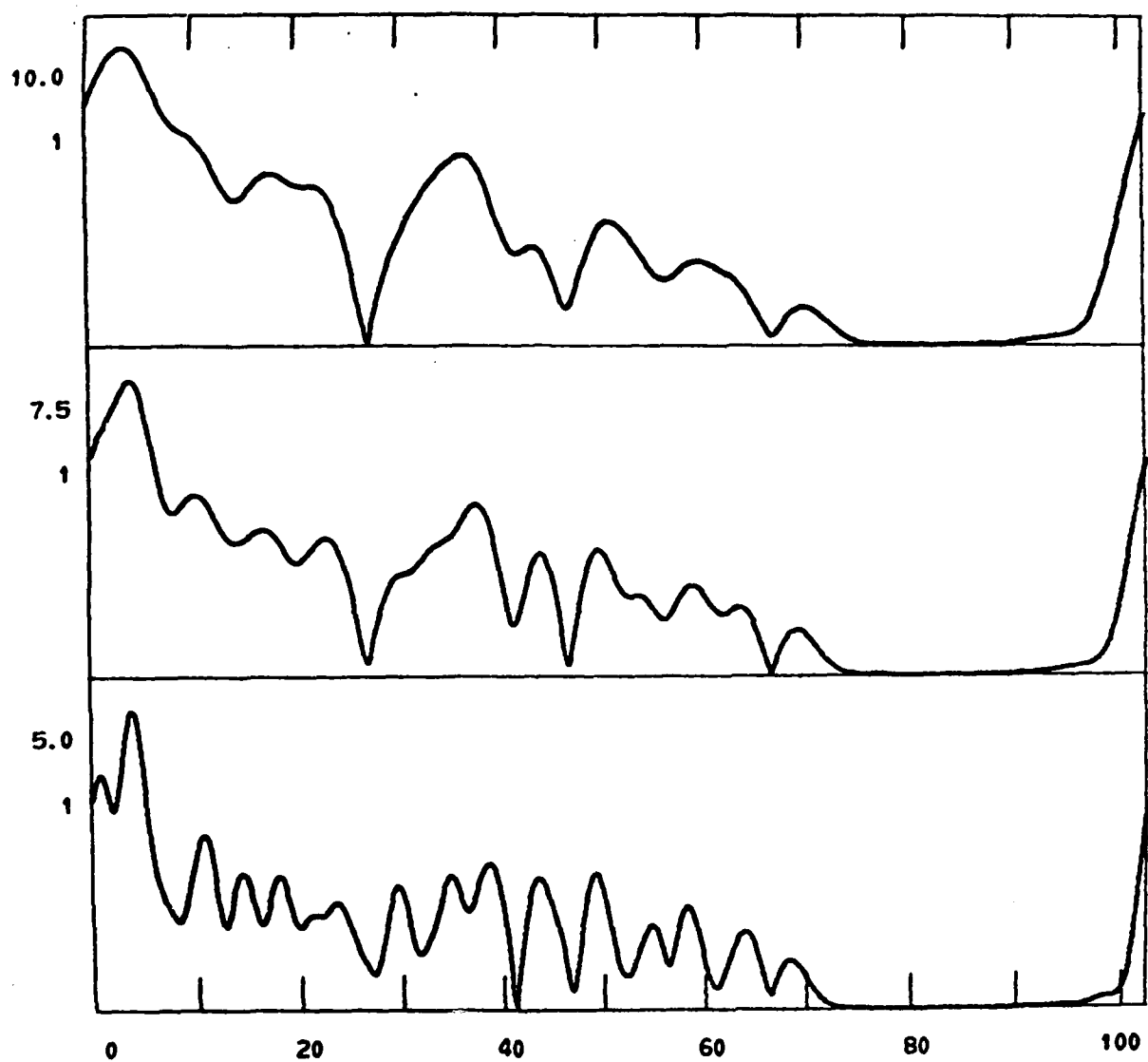


Figure 3.2: Same as Figure 3.1, at Adak-B site.

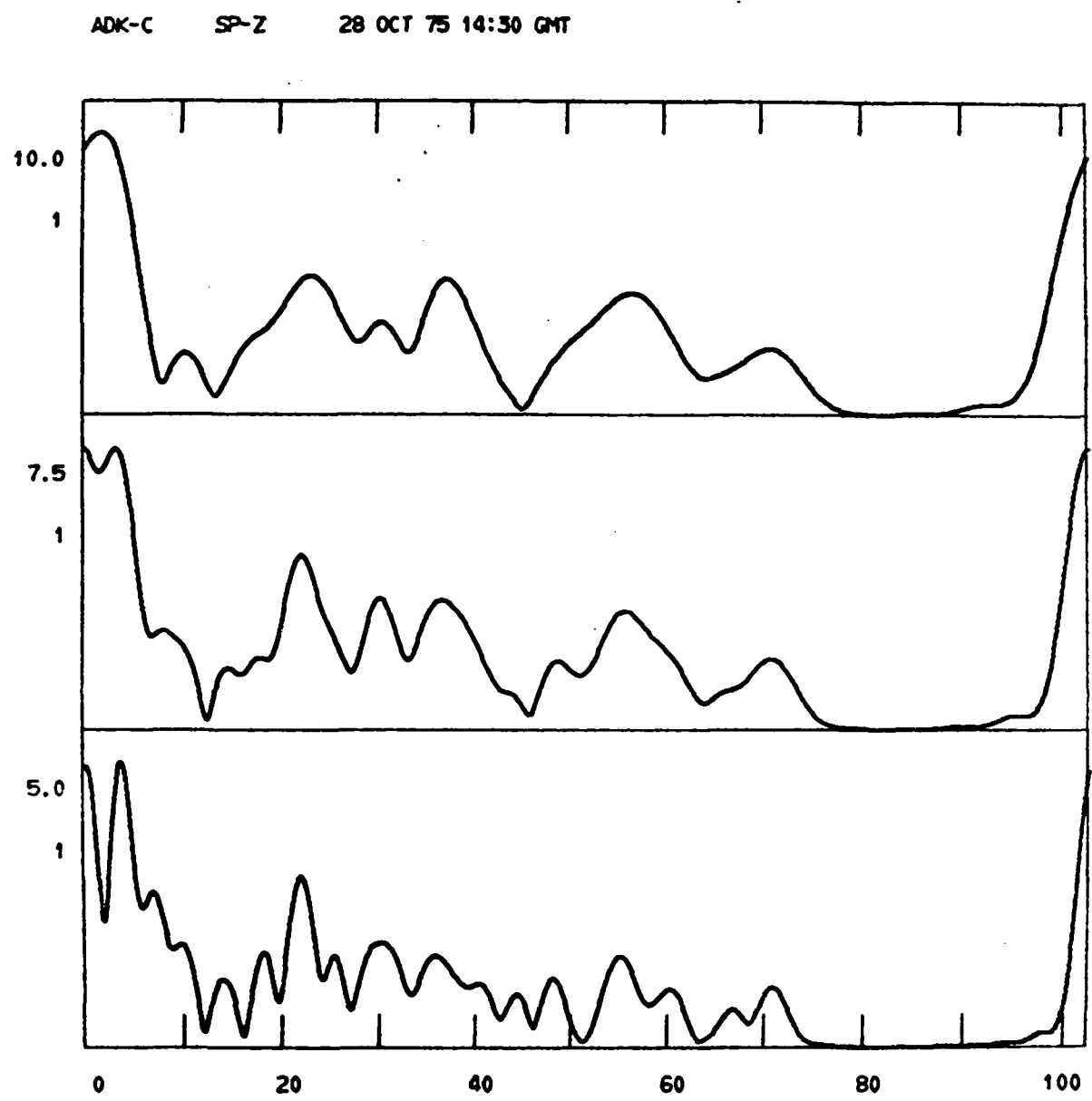


Figure 3.3: Same as Figure 3.1 at Adak-C site.

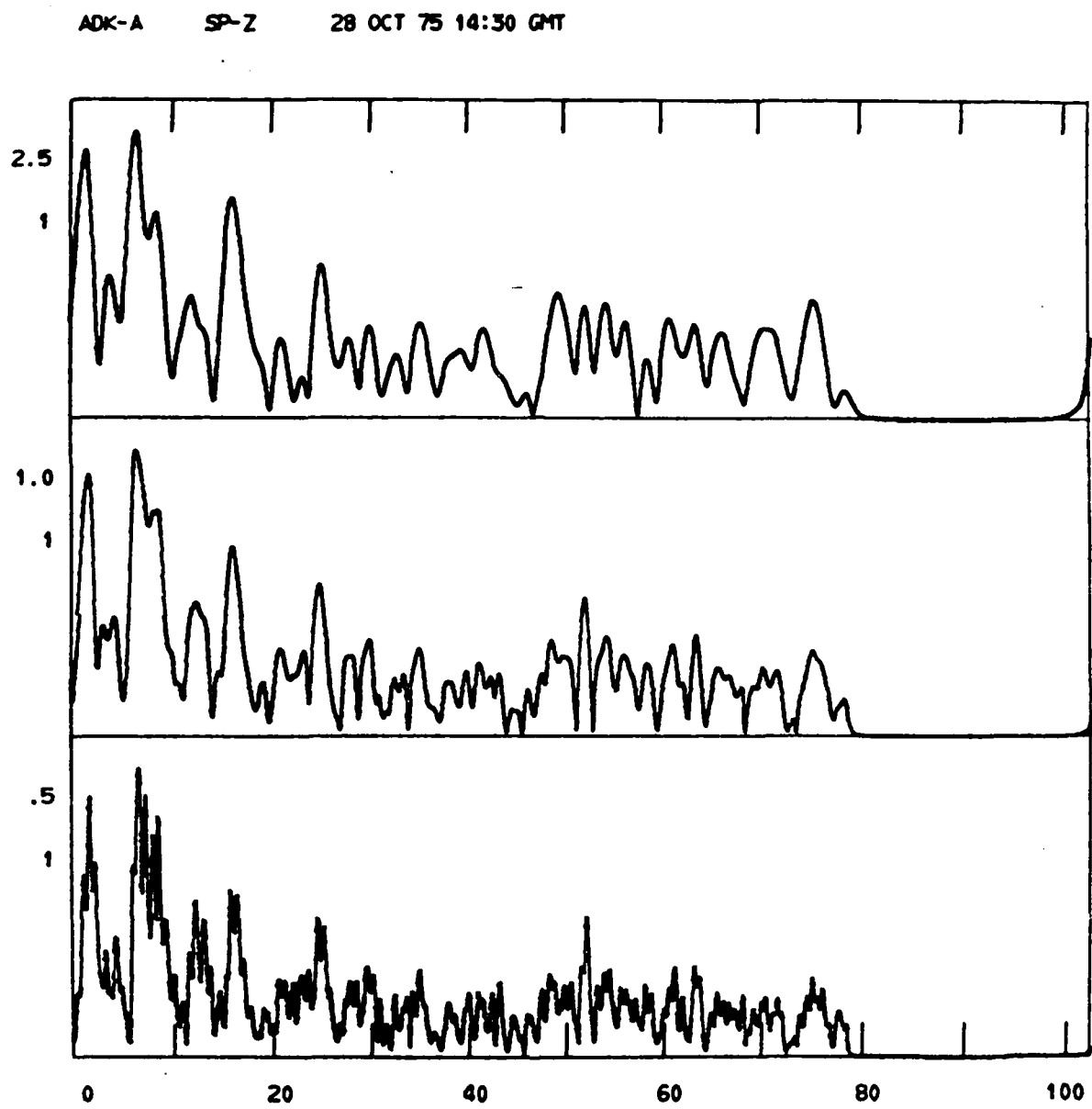


Figure 3.4: Same as Figure 3.1 for  $(Q, f_0) = (2.5, 1)$ ,  $(1, 1)$  and  $(0.5, 1)$ .

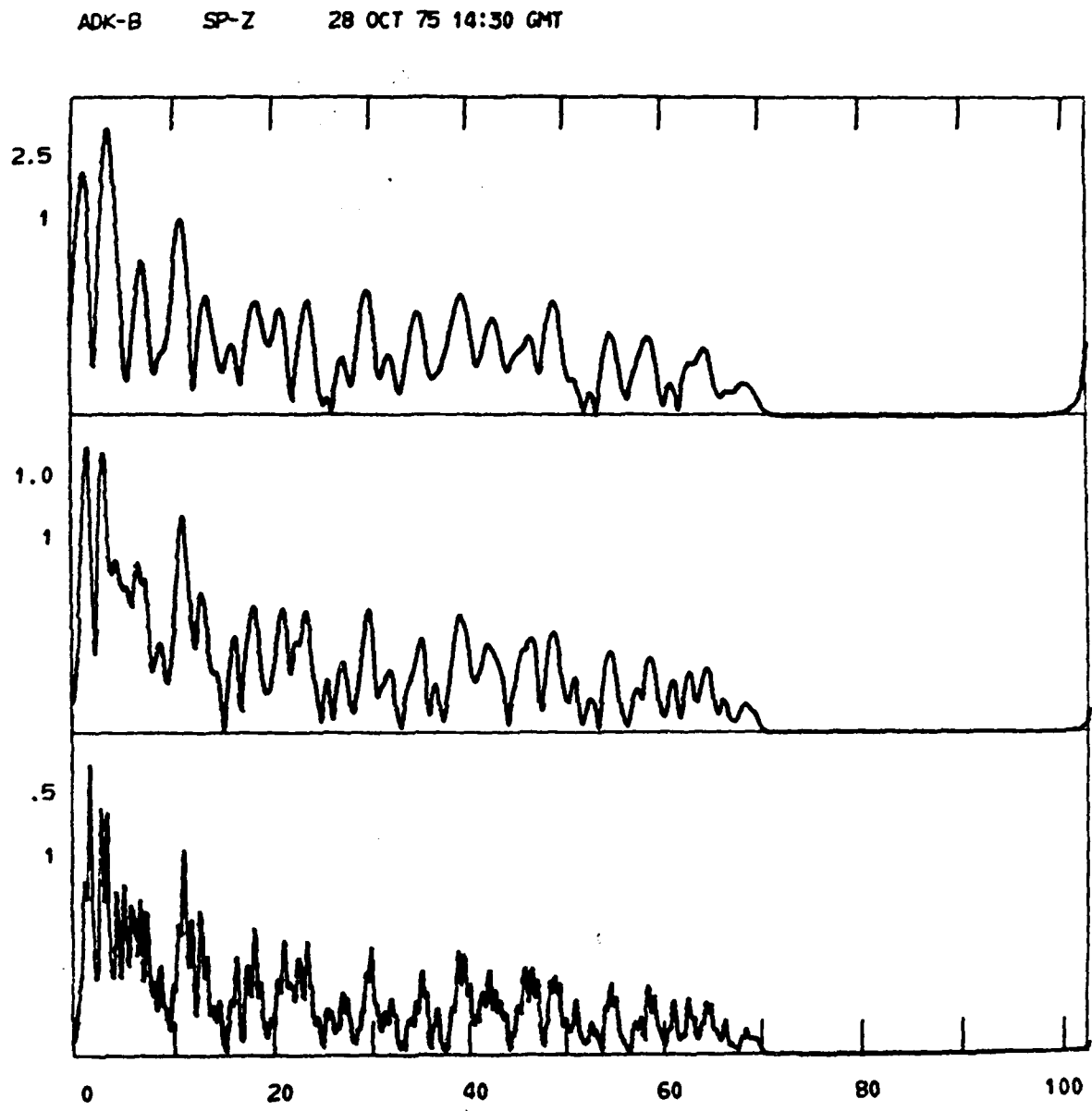


Figure 3.5: Same as Figure 3.4, at Adak-B site.

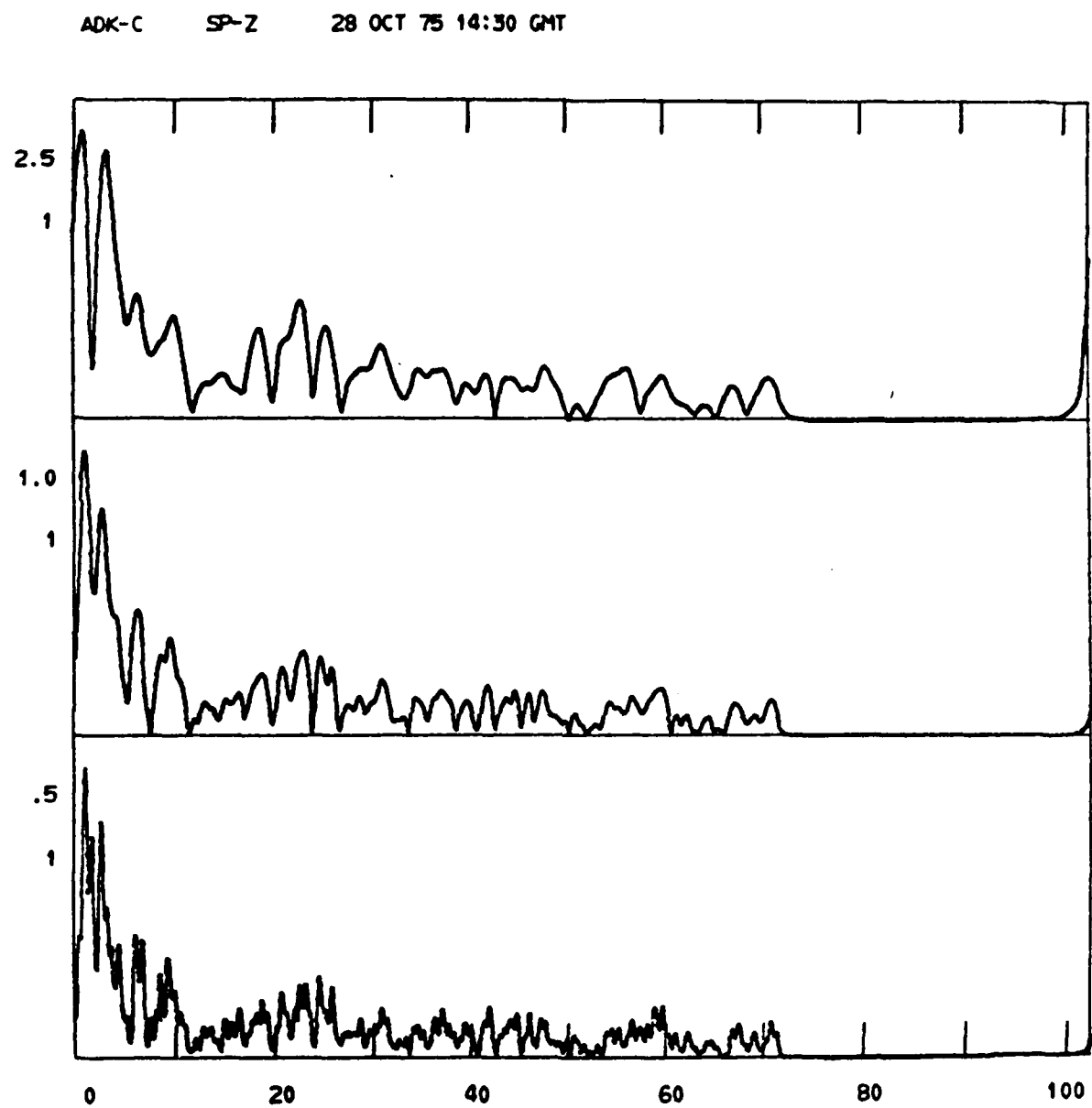


Figure 3.6: Same as Figure 3.4, at Adak-C site.

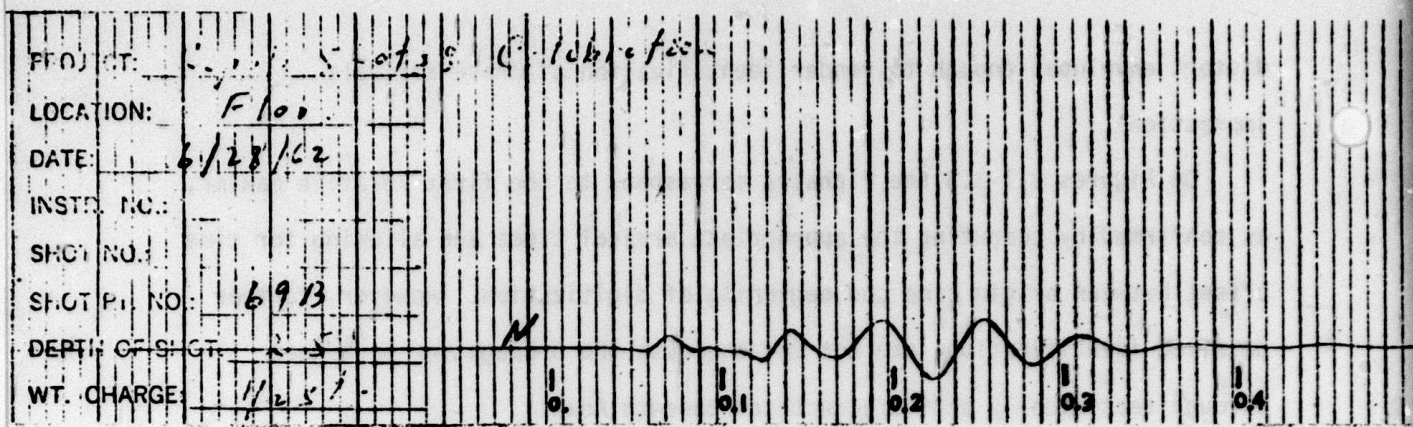
distort envelopes enough to render identification of phase arrivals impractical.

On Figures 3.1-3.3 the P phases correspond to the first relative maxima, as confirmed by computing the appropriate arrival times and allowing for time offset between origin time and beginning of digitization. However, further detailed identifications are not made because the propagation path goes through tectonically active structures beneath Adak.

Next, data due to small chemical explosions from the Florissant site (Kisslinger et al., 1963) are used to examine the effects of variation of  $Q$  with  $f_0$ . The seismograms used (shot points 69B and 71) were recorded at 30 m away from the sources, and phases are thus very closely bunched, on the order of less than 0.1 sec. Figure 3.7 shows the seismogram used and log-log plots of the amplitude spectrum, and filtered amplitude spectra, along with filters for (0.1,40), (1,40) and (10,40).

The time-domain envelopes with two additional filters ( $f_0 = 160$  and 640 Hz) are shown as the lower two traces of Figures 3.8-3.10. Amplitudes are always scaled relative to the top trace of each figure. Because of broad filters used in Figure 3.8, hardly any differences exist among the three envelopes. Figure 3.9, on the other hand, shows that as  $f_0$  is increased  $\beta$  becomes smaller and filtered envelopes begin to resemble those of Figure 3.8. Increasing  $f_0$  is equivalent to decreasing  $Q$ , as far as resolution is concerned.

The top trace of Figure 3.10 again confirms the validity of the resolvability criterion. Despite being the largest  $\beta$  ( $\beta = 1/24$ ) among those tested here, this  $\beta$  still does not satisfy inequality (3.5). As can be seen, only a broad envelope is obtained, resolving nothing. As higher centering frequencies are used, less content of seismic information is retained and is reflected



$f_0 = 40$

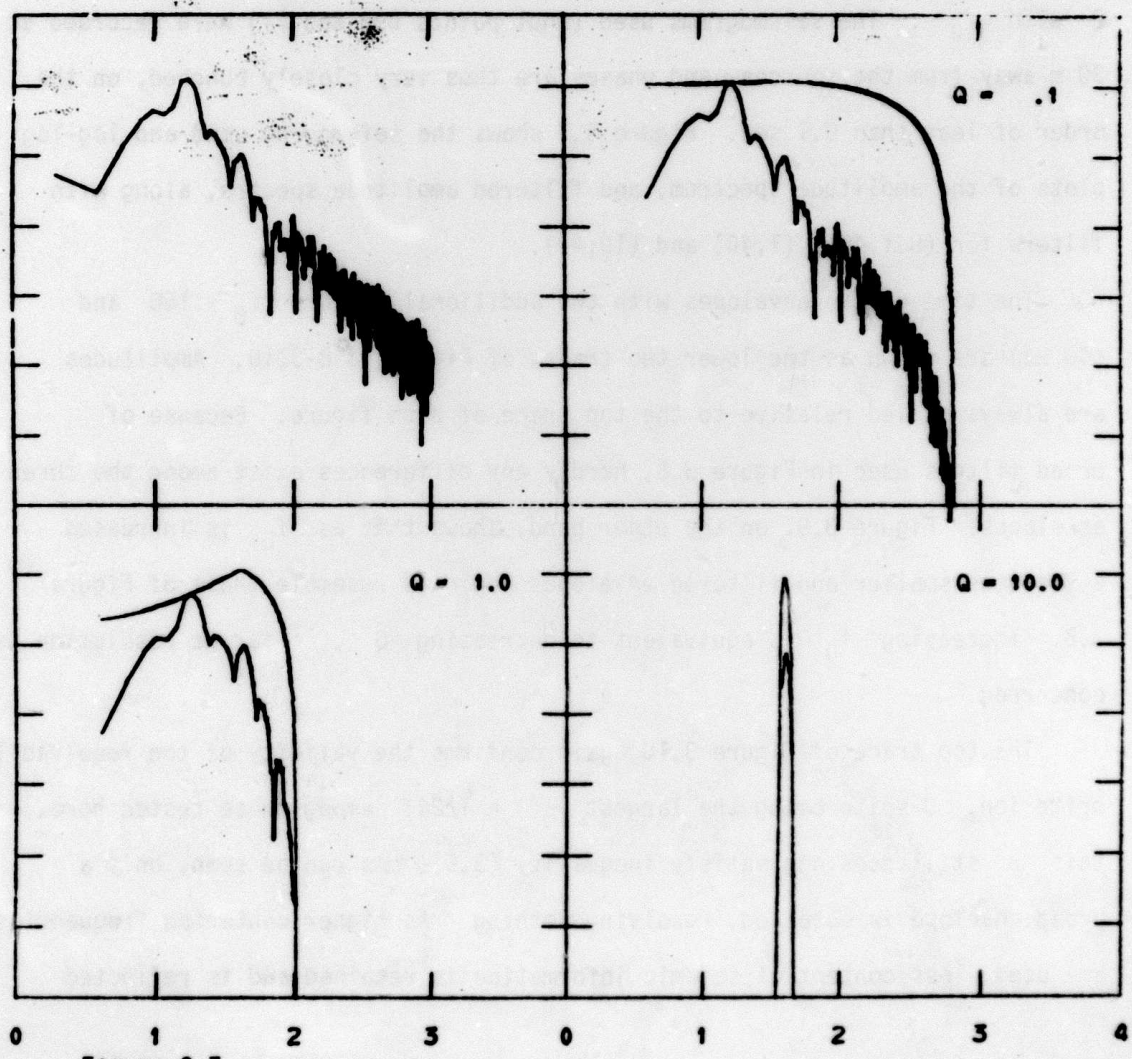


Figure 3.7

Figure 3.7: The top is a seismogram from shot point 69B,  $t = 0$  corresponds to  $t = 0$  in Figures 3.8-3.10. Four log-log plots illustrate instrumentally deconvolved spectrum at top left and three filtered spectra with  $f_0 = 40$  along with respective cusp-shaped filters. Amplitudes are in arbitrary units while abscissa is log frequency.

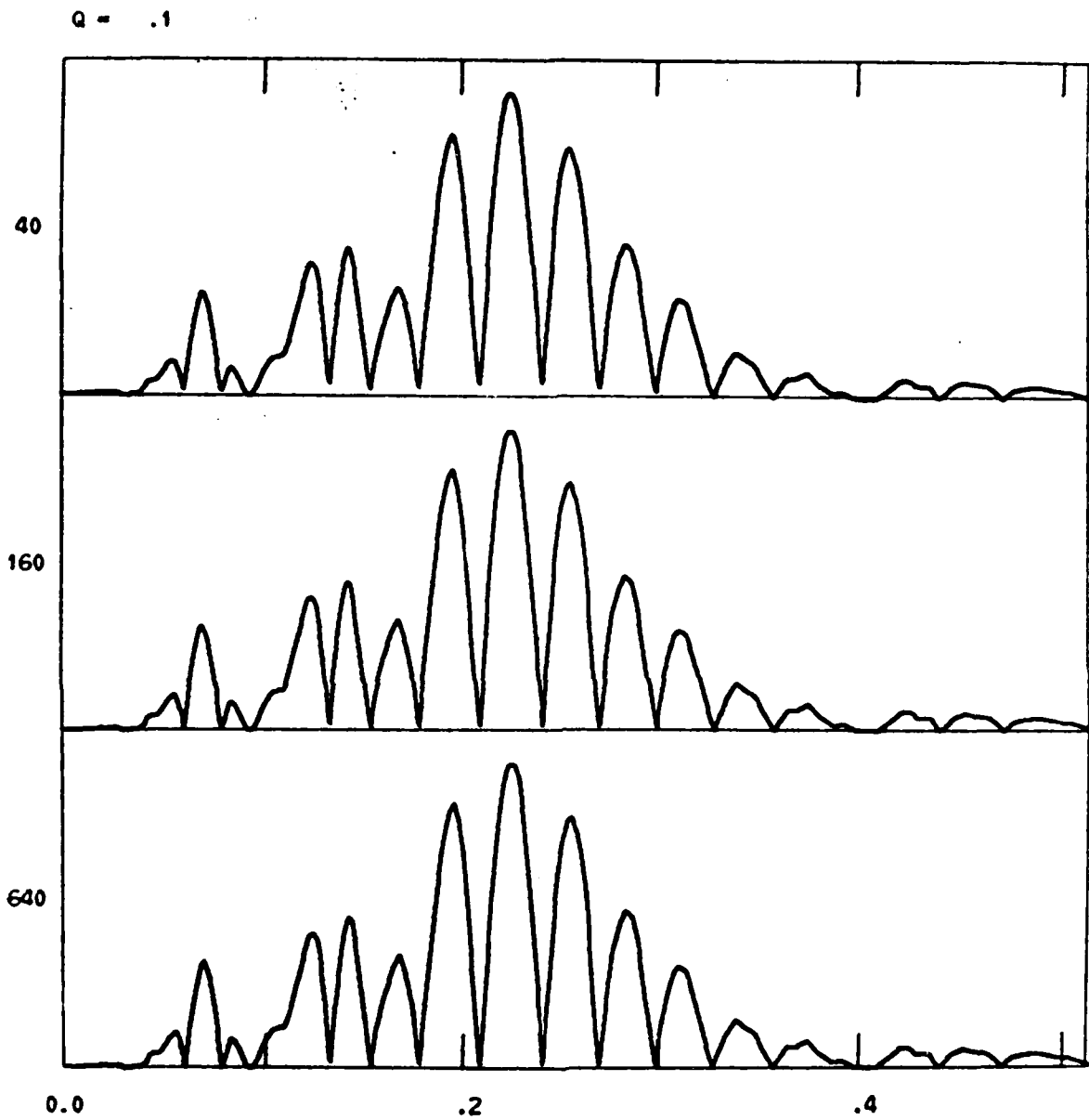


Figure 3.8: Filtered envelopes using  $(Q, f_0) = (0.1, 40)$ ,  $(0.1, 160)$  and  $(0.1, 640)$  for the record in Figure 3.7.

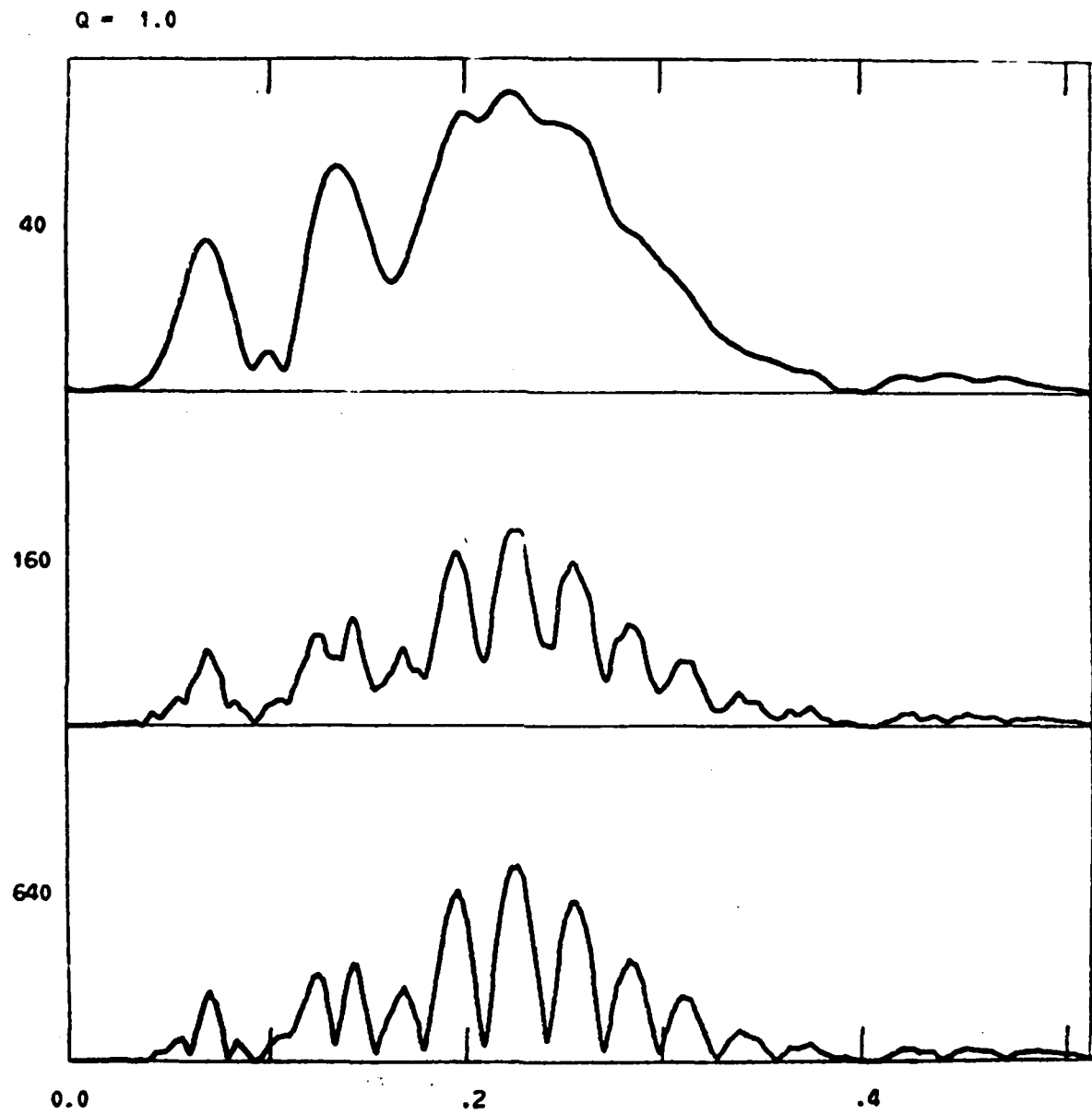


Figure 3.9: Same as Figure 3.8 except for  $(Q, f_0) = (1, 40)$ ,  $(1, 160)$  and  $(1, 640)$ .

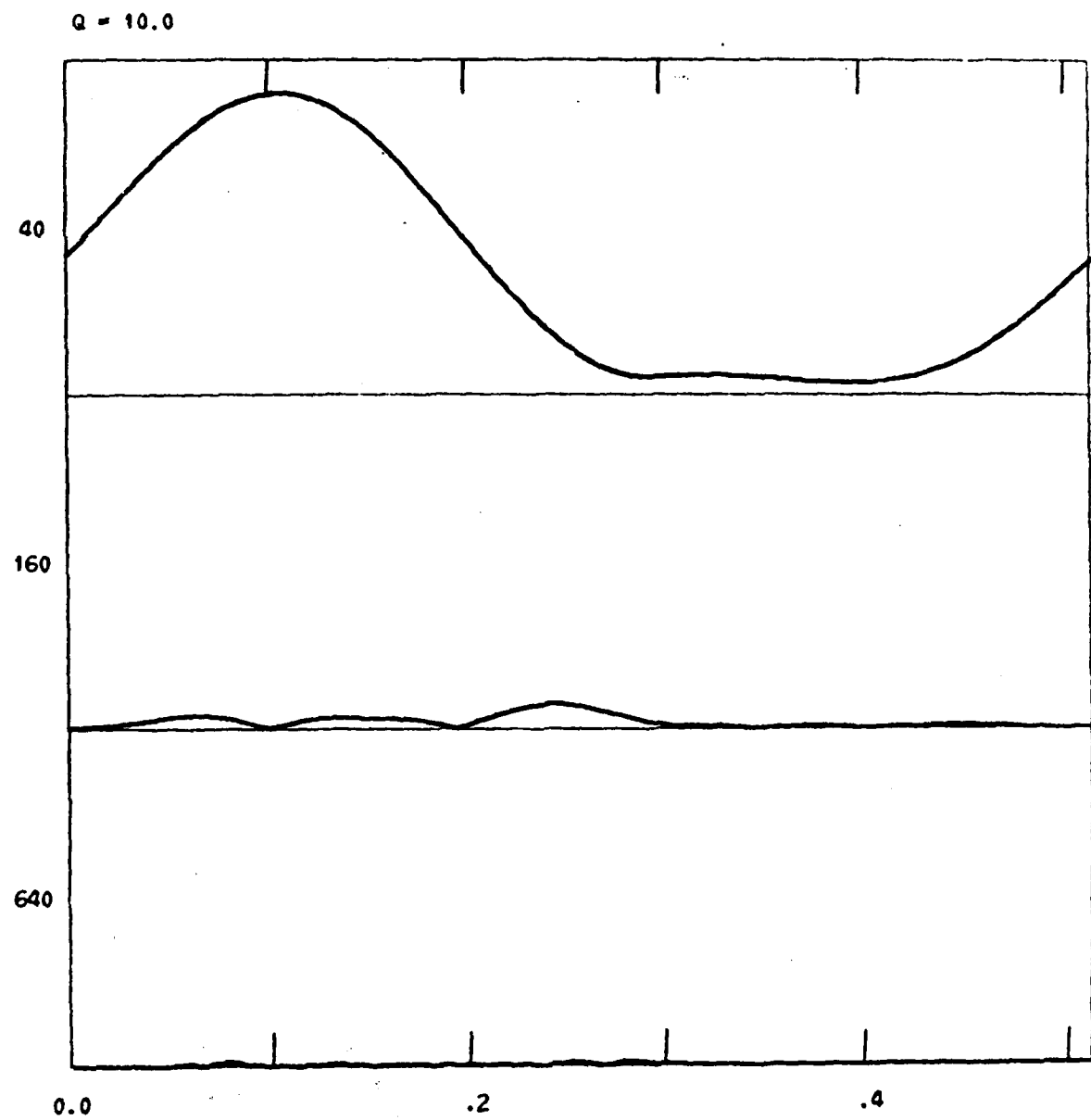


Figure 3.10: Same as Figure 3.8 except for  $(Q, f_0) = (10, 40)$ ,  $(10, 160)$  and  $(10, 640)$ .

by a steady decrease in amplitudes on lower traces of Figure 3.10. Incidentally the bottom plot actually has the the same features as that of Figure 3.8, though these cannot be seen on the scale used here for plotting.

It should be noted that Figures 3.8-3.10 in spite of small  $\beta$ 's being used, do not show complexity in envelopes similar to that on lower plots of Figures 3.4-3.6. This is because seismic record itself is composed of nicely rounded waves, so essentially what has been accomplished with small  $\beta$  here is an enhancement of troughs and peaks of seismogram.

Although it looks as though some phases can be assigned to top trace of Figure 3.9, such identifications cannot be readily substantiated. A simple calculation of reflected and refracted wave arrivals based on seismic-velocity model given by Kisslinger et al. (1963) shows, in fact, many phases must be present about the times of those relative maxima. Thus, although the envelope shapes look enticing for phase identifications, those relative maxima must be due to superposition of a number of phases and cannot be associated with any single phase.

Because peaks and troughs can be greatly enhanced by using broad filters provided seismograms themselves are not spiky, Figure 3.12 illustrate how one can enhance the seismic records of Figure 3.11.

The waveforms of Figure 3.11, were generated by two explosions fired approximately 0.016 sec apart, the first one being fired, as shown in Figure 3.12, at southern dot, 1.5 m from the center of the circle of 30 m radius. Symmetry about the line of shots (shots from South to North) is reflected in Figure 3.12, although the records seem to indicate that actual line of shots might be slightly oriented toward west rather than exact northward direction.

The results shown in Figure 3.12 are not encouraging as far as demonstrating a method of discriminating the two component detonations. Figure 3.12 provides



Figure 3.11: Complete seismogram records for shot point 71. Two explosions are fired with time separation of 0.016 sec.

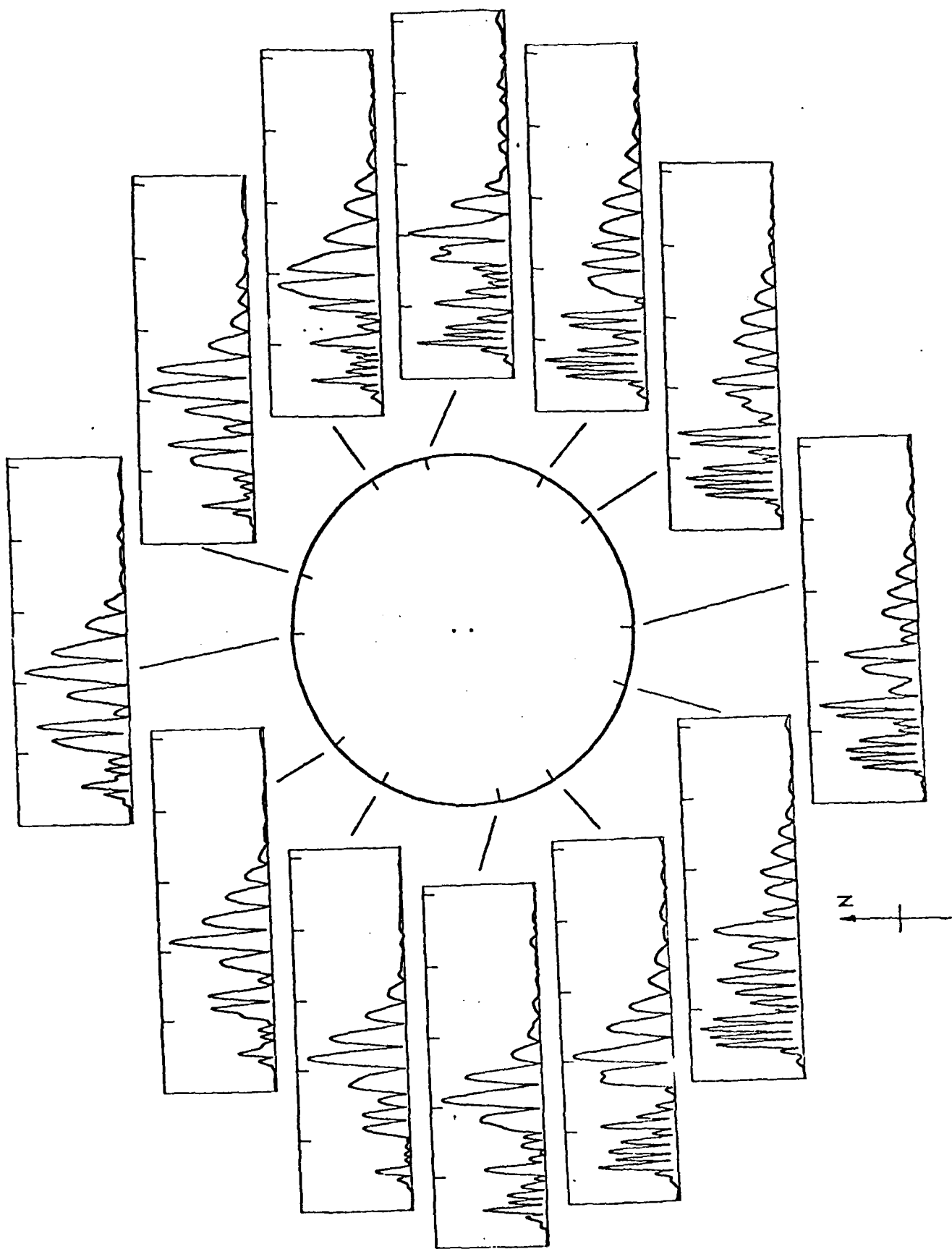


Figure 3.12: Filtered envelopes using  $(Q, f_0) = (0.1, 40)$  for records in Figure 3.11. Two dots near the center of circle (actual radius 30 m) represent source positions (1.5 m) from the actual center. Firing was done in northward direction.

hardly any hint of two shots except for a small step-function rise at the onset of some P phases. Some other methods, like cross correlation with a single shot record, might be more effective because band-limited filtration, as demonstrated in this report, has its limitation when applied alone. It may be possible to apply band-limited filtration in conjunction with a polarization filtration for improved results, but it remains to be seen whether such a scheme would apply to multiple events or phases of very short separation.

Finally, it should be pointed out again that a minimum radius exists within which phase identifications will be hampered when applying band-limited filtration for analysis. Although analytic attention is focused mainly on non-dispersive signals, the resolvability criterion should be applicable to dispersive signals as well.

References

Archambeau, C. B. and E. A. Flinn (1965). Automated analysis of seismic radiation for source characteristics, Proc. I.E.E.E., 53, 1876-1884.

Jeffereys, H. and K. E. Bullen (1948). Seismological Tables, Neill & Co. Ltd., Edinburgh.

Kisslinger, C., E. J. Mateker, and T. V. McEvilly (1963). Seismic waves generated by chemical explosions, AFCRL-63-701, Final Report, Contract No. AF19(604)-7402, St. Louis University.

Savino, J. M., T. C. Bache, J. T. Cherry, K. G. Hamilton, D. G. Lambert, and J. F. Masso (1975). Application of advanced methods for identification and detection of nuclear explosions from the Asian continent, Semi-Annual Technical Report, Systems, Science and Software, La Jolla, California.

4. Determination of Focal Depth and Focal Mechanism by Synthetic Seismograms

W. Gawthrop and T. Hewitt

Faulting parameters for six shallow earthquakes in the range  $m_b$  5.5-6.5 have been determined by best-fitting long-period P-wave synthetics to observed seismograms (Herrmann, 1976). P-waves were digitized from the long period vertical component of WWSSN stations in the distance range of 30°-80° for each event, with a wide range of azimuths. Focal depth and fault plane orientation of an equivalent quadrupole point source were varied to best match the synthetics to the observed seismograms at the recording stations by maximizing the correlation coefficient between the two time series. By varying each parameter by incremental values from the "best" solution, an indication of how well each parameter is determined can be obtained by visual inspection of the observed and calculated traces. Preliminary results indicate that focal mechanisms of strike-slip events are strongly determined utilizing few stations, whereas dip-slip mechanism are poorly determined by use of P-wave synthesis alone. Focal depth resolution is slightly better for thrust and dip-slip events than for strike slip events, both of order 1 to 3 km. The absolute accuracy depends on the accuracy of the assumed source crustal structure. The correlation technique currently used needs revision to resolve the slight variations in waveform caused by small changes in faulting parameters.

The synthetics calculated for comparison are computed assuming a point source quadrupole of arbitrary orientation, moment, and source-time forcing function located somewhere in the crust. Reflections of P and S waves in the source crust originating at the point source are added to obtain the approximate time and amplitude history of P waves entering the mantle. Amplitude of each phase is a function of the quadrupole orientation and the reflection coefficients, whereas the time lag of each pulse is a function of the source depth and the

crustal velocity structure. A non-causal Q filter and a geometrical spreading term are applied to the mantle P wave before its incidence at the receiver crust. Reflections of P and S waves resulting from the incident mantle P wave are again summed and the final ground motion is convolved with the system response of the 15-100 WWSSN seismograph. Simplifications in the assumed crustal structures and the point source assumption along with normal digitization errors cause the best correlation coefficient between the synthetic and observed seismograms always to be less than 1.

#### 4.1 Procedure.

Film chips from WWSSN stations in the proper distance range were viewed to select up to twenty stations with high signal-to-noise ratios and good azimuthal coverage of the earthquake. One or more minutes of the long period vertical component of each selected station was digitized. The peak magnification of the seismograph is entered with the digitized data. The program incorporates the response curve of the seismograph as a subroutine, in this application the standard response of the 15-100 WWSSN system. An approximate fault plane solution was assumed from either first motion data or knowledge of the general tectonics of the region. A triangular shaped source-time forcing function was assumed with duration approximately determined by inspection of either a deconvolution of the seismograph response from the observed seismogram or simply from the seismogram itself, the former being a more accurate method. Source and receiver crusts, if unknown, are arbitrarily assumed from the type of region involved, e.g., continental shield.

P waves are synthesized using the above information for sources at several depths within the crust separated by a few kilometers. The first 12 seconds of the synthetic are correlated with the digitized seismograms, and the depth

yielding the highest correlation coefficient (usually around 0.9 for the initial pass) is selected as the most probable. Corrections to the focal mechanism at the selected depth can then be determined automatically for the earthquake by an iterative method of maximizing the correlation coefficient. Several further steps of refining the source parameters are made by repeating the last two steps with possible alteration of the slope of the source time forcing function. The area of the source time forcing function required to match the observed data is equivalent to seismic moment of the point source quadrupole.

Without detailed knowledge of the crustal structures in the vicinity of the earthquake and each receiver site, only the first several seconds of the seismogram can be accurately modeled. 12 seconds after the onset of the P wave is usually adequate to include the direct P, the pP, and the sP waves, which are usually the strongest and the least dependent on crustal structure. Since both up-going and down-going rays are modeled, each P-wave seismogram samples two distinct parts of the focal sphere, allowing good focal mechanism determination from a small number of stations. The time difference of the surface reflected waves from the direct P wave very accurately determines the focal depth if the velocities of the upper crust are known reasonably well. The focal mechanism determination by the amplitude of each pulse and the focal depth determination by the time lag between pulses are two discretely determined sources of information which are not utilized separately using the correlation coefficient technique. A technique should be developed to distinguish better between time-space and amplitude-space for increasing the ease and accuracy of the source parameter determinations.

#### 4.2 An Example.

The Nov. 5, 1969 Santa Lucia Bank earthquake ( $m_b = 5.8$ ), offshore of

central California, is used to illustrate the value of the body wave synthesizing technique for determining source parameters. Aftershocks of this earthquake indicate a short rupture (about 10 km) along a northwest trending fault (Gawthrop and Engdahl, 1975). Offshore seismic profiling in the region has defined several fault traces with Holocene vertical displacement trending between N30°W and N60°W (Eli Silver, personal communication, 1975). All first motion data are from a single compressional quadrant of the focal sphere, allowing only a poor determination of the focal mechanism to be made by conventional means. Since the earthquake was well recorded at over 250 well-distributed stations, a very precise epicentral location ( $\pm 5$  km at the 95% confidence level) was made. Focal depth from the teleseismic location is poorly determined, making this earthquake a prime candidate for study by means of body wave synthesis.

Four stations, College, Alaska; Godhavn, Greenland; State College, Pennsylvania; and Arequipa, Peru, were selected for P-wave analysis, covering an azimuthal range of about 170° on the focal sphere. A source crustal velocity structure of 6.0 km/sec down to 20 km and 8.0 km/sec below 20 km was assumed. An isosceles triangular shaped source time forcing function with a four second duration and a seismic moment of  $10^{25}$  dyne cm fit the data quite well. The focal depth is indicated to be at 8 km assuming the 6 km/sec crust. The near-surface velocities may actually be slower near the surface, suggesting a somewhat smaller focal depth. The focal mechanism determined is consistent with both the world-wide first motion data and the available field evidence. The mechanism is shown in Figure 4.1, with the observed seismograms plotted with the best-fitting synthetics for the four stations.

An indication of the resolution of the focal depth and focal mechanism is shown in Figure 4.2, where the effects of varying each parameter individually

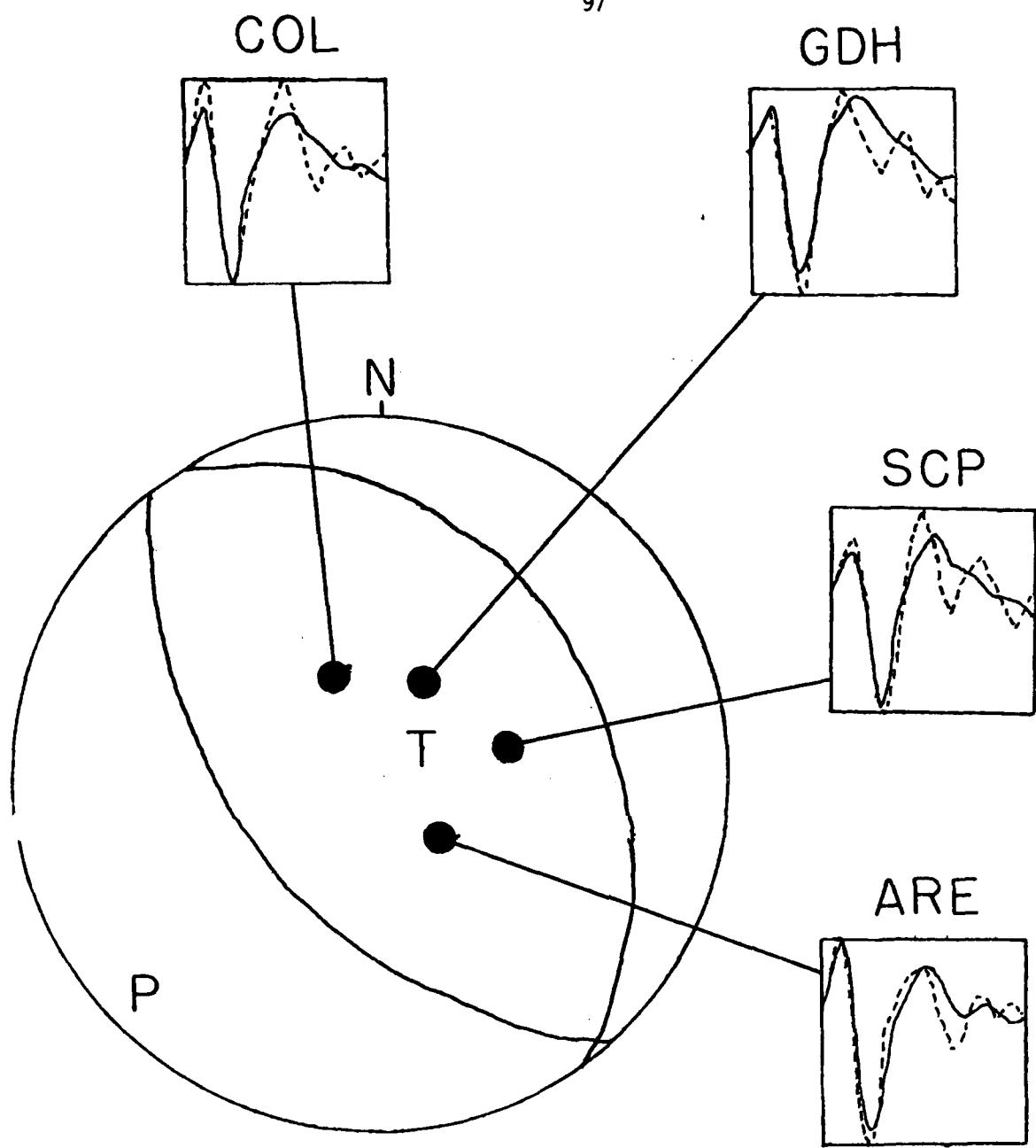


Figure 4.1: Focal mechanism which give maximum correlation between observed seismograms (dashed line) and the synthetics (solid line) for all four stations. Black dot is point of departure through the focal sphere on a stereonet plot.

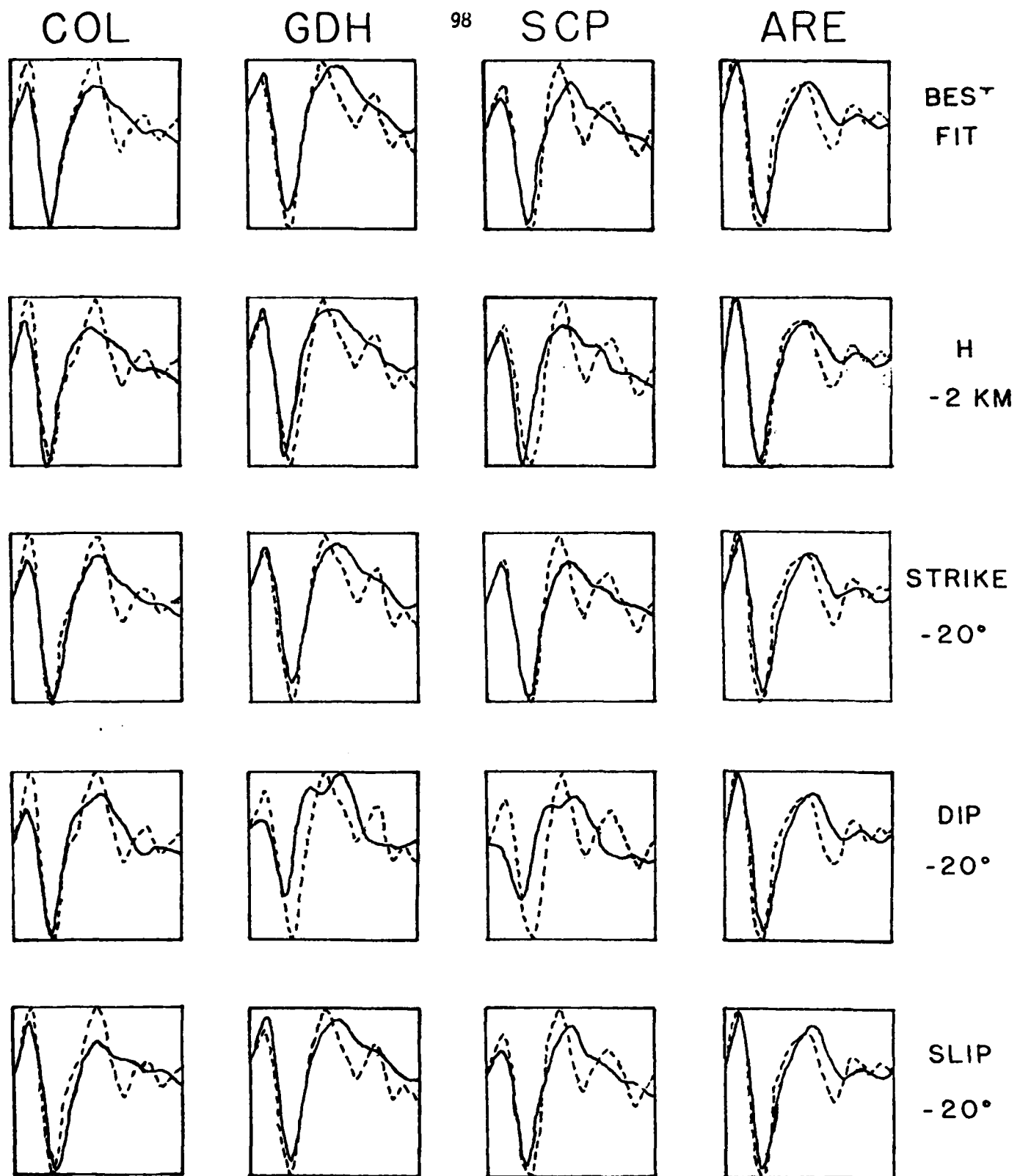


Figure 4.2: Observed (dashed line) versus calculated (solid line) seismograms of all four stations for the best focal mechanism and depth and for variations in  $H$ (depth) and the parameters of the focal mechanism.

are shown. The change in waveform with varying focal mechanism parameters is very slight, indicating that these parameters are not well-fixed. Focal depth, however, can be resolved to better than 2 km for this event on the basis of peaks and troughs.

#### 4.3 Approaches to Improving the Method.

In view of these promising results, as well as the deficiencies brought out in the examples, it was decided to seek improvements by modification of our long-period body wave analysis. Modifications that have been or are currently being made include:

- (1) Techniques for detecting and correcting digitization glitches;
- (2) The addition of SH waves to improve the determination of local mechanics of thrust type events;
- (3) Generalization of the method for applications to subcrustal and oceanic events;
- (4) Allow source and receiver crustal velocities to be varied;
- (5) Inclusion of all possible rays with not more than two reflections off the Mohorovicic discontinuity;
- (6) Assignment of individual weights to stations;
- (7) Estimation of error of fit due to instrumental noise.

These improvements are being implemented through a two-step approach. In the first step digitized vertical- and transverse-component seismograms will be plotted and compared with the WWSSN data so that one can find and remove data glitches.

Synthesis of seismograms and fitting will then be accomplished as follows:

- (1) Fit a short time duration of seismogram for source depth and focal mechanism to assumed crustal velocities, thicknesses, and source time functions;

- (2) Fit best source time function leaving other parameters fixed and find time shifts due to starting digitization at the wrong time;
- (3) Increase the time over which we are fitting to 30 sec and find the best fit of crustal velocities and structure, leaving other parameters fixed;
- (4) Decrease the time we are fitting to 20 sec and obtain the best fit to depth and focal mechanism;
- (5) Plot the final results.

SH wave character analysis is a much simpler problem than that of P and/or SV wave analysis, since boundary reflections and transmissions yield SH waves. For this reason we feel that the observed SH character will be easier to synthesize than the observed SV character. The source crustal response will consist of only seven rays, three which initially travel up and are reflected down to the free surface, and four which initially travel to the Mohorovicic discontinuity and are either transmitted into the mantle or reflected back up to the crust. The receiver crust is similarly simplified with only four major rays involved. Calculation of SH reflection and transmission coefficients has been done.

New source crustal response subroutines which take into account all rays not more than two reflections off the Mohorovicic discontinuity have been written with the aid of a computer program which constructs all possible rays and groups all rays which have the same time delay into one. This approach enables not only more accurate synthetic wave forms to be produced, but has reduced the necessary computer time, a reduction which is of importance for the inverse calculation. It has also enabled the quick and accurate production of modifications such as the extension to upper mantle earthquakes, and the inclusion of the effect of an overlying layer of water, which strongly affects the waveforms of all oceanic events.

Because of the extremely large number of rays which would be needed if one were to trace all important rays which travel in the water layer, a different technique for handling this was devised. This technique treats a ray which reflects back into the crust from the water-rock interface as we have done previously, but combines all rays arising from one which enters the water layer as one "ray" whose wave form must now be convolved with the water layer response. We can have "rays" which enter the water layer as often as three times, so we must also calculate the effect of double and triple convolutions with the water layer. The convolution of a wave form with the water layer  $N$  times is given by

$$W_N(+) = \sum_{i=0, \infty} (-WW)^i \cdot (-1) \cdot F_N(i) \cdot S(t-(i+1) \cdot \Delta t)$$

where  $W_N(+)$  is the new wave form,  $S(t)$  is the old wave form,  $WW$  is the reflection coefficient of a P wave at the water-rock interface,  $\Delta t$  is the delay added to a ray which traverses the water layer twice, and  $F_N(i)$  is 1 if  $N = 1$ ,  $i$  if  $N = 2$ , and  $i(i-1)/2$  if  $N = 3$ .

References

Gawthrop, W. H. and E. R. Engdahl (1975). The 1927 Lompoc earthquake and the 1969 Santa Lucia Bank earthquake sequence, a comparative study, EOS, 56, 12, 1028.

Herrmann, R. (1976). Focal depth determination from the signal character of long period P waves, Bull. Seism. Soc. Am., in press.

## 5. Classification of Seismic Events.

G. Lundquist

The purpose of this investigation is to determine whether different spectral classes of earthquakes occur within central Asia and whether particular spectral classes may be related to seismic source parameters, focal mechanisms, or special features of regional or local tectonics. Toward this end, a review has been undertaken to put spectral parameterization and the physical interpretation of these parameters in a proper perspective. Particular emphasis has been put on the inherent properties of spectra, the energy balance during an earthquake, the time history of parameters such as stress drop, and the effect of finiteness on the source. The result is that few source parameters will be estimated from the spectrum for classification purposes, while others will be avoided in place of a classification by spectral properties alone. The interpretation of these controversial properties need not affect a classification scheme, but they will affect the attempt to understand the causes of earthquakes of different kinds. We demonstrated early in this project (Semi-Annual Report No. 2, 1974) that earthquakes with various types of spectra are observed, so the relationships between spectral properties and source parameters is of current importance.

Spectra have inherent properties simply by virtue of being Fourier transforms, and displacement amplitude spectra have further properties due to the general constraint of conservation of energy. We will only note these properties here, with appropriate references. For purposes of discussion, we will consider the spectrum to have three regions: (I) frequencies lower than the peak frequency or lowest corner frequency in the case that the spectrum is flat or decreasing toward  $\omega = 0$ ; (II) intermediate frequencies; and (III) frequencies higher than the highest corner frequency. Observed spectra generally

have zero or positive slopes in region I, slopes of  $\omega^{-2}$  to  $\omega^{-3}$  in region III, and behavior in region II which may be approximated by two or fewer line segments on a log-log plot.

For the total radiated energy to be finite, the spectrum must lie under a line of slope  $-3/2$  on a log-log plot. In terms of Fourier transform theory, this result is obtained from the inverse proportionality of signal duration to bandwidth. That is, the observed corner frequencies imply that an earthquake cannot radiate its energy over a vanishingly small time. Thus, though some seismic source models have point force equivalents in space (Burridge and Knopoff, 1964), conservation of energy specifically prohibits  $\delta(t)$  behavior in time. By this analysis, every constraint on the motion or energy release adds to the delta-like character of the time signal and contributes to extending the bandwidth.

The final high-frequency asymptotic decay rate of the spectrum is determined by the smoothness of the source-time function. If the  $k^{\text{th}}$  derivative of the displacement becomes impulsive, then

$$\lim_{\omega \rightarrow \infty} \Omega(\omega) = \theta(\omega^{-\gamma}) \quad (5.1)$$

where  $\gamma \geq k$  (Bracewell, 1965). Thus a region III slope of  $-2$  implies that the acceleration is infinite (impulsive). The concept of infinite accelerations is not pleasing, but very high accelerations have been measured in the near-field of some earthquakes. If the displacement,  $u(\xi, t)$  (where  $\xi$  describes location on the source) has at least two continuous derivatives, and a rise time of  $\delta t$ , then frequencies above  $(\delta t)^{-1}$  Hz would recognize the smoothness of  $u(t)$  and decay at least as fast as  $\omega^{-3}$ . But frequencies below  $(\delta t)^{-1}$  Hz will sense a discontinuous velocity and decay as  $\omega^{-2}$ . The fact that behavior

appropriate to a continuous function ultimately sets in may not be of practical concern, since only components of period shorter than the shortest time constant will exhibit continuous behavior, and they may be out of the passband. Spectral shape is thus very likely different for spectra of different fault size or energy level, though the true high frequency decay may well be masked by the anelastic attenuation (see Appendix 5A).

The long-period behavior (region I) is representative of gross average behavior at the source, and the far-field displacement depends upon particle velocity on the fault (Haskell, 1964). If  $u(\xi, t)$  is unipolar (all positive or all negative) on the fault, then  $u(r, t)$  has a transform which is maximum at  $\omega = 0$  in the far field. The derivate theorem of Fourier transform theory also assures us that the spectrum will have zero slope at  $\omega = 0$  for any real function with sufficient continuity conditions and finite area. Thus estimates of fault motion which give unipolar  $u(\xi, t)$  require the spectrum to be both flat and maximum at  $\omega = 0$ .

A sufficient condition for a peaked spectrum is that the average source velocity function change sign. As modeled by Husseini (personal communication), allowing the fault to overshoot the static equilibrium and then oscillate about equilibrium causes a peak in the spectrum of only 15% of the  $\omega = 0$  value. Archambeau (1975) argues that irregularities in prestress, displacement or particle velocity could sum in an average to give a peaked spectrum. However, the spectrum of a relaxation source is peaked even when smooth conditions are modeled (Minster, 1974). Thus the difference between dislocation models and relaxation models would seem to lie elsewhere in the treatment. We note, in particular, that Minster solves for a complete multipole expansion, with all source properties specified before obtaining a far-field approximation, while Haskell (1964) and his successors (Aki, 1967; Savage, 1972; Brune, 1970) all

make a far-field approximation before specifying the source-time function.

Robinson (1967) notes that radiation by a continuous surface radiator (antenna) may take place at all frequencies, but that the relative contribution is insignificant until the size of the radiator (fault) is comparable to a wavelength. Wavelengths larger than the largest dimension of the fault are transmitted as evanescent waves which die out rapidly away from the plane of the radiator (Champeney, 1973). Thus antenna and diffraction theories say that wavelengths longer than the source cannot be radiated to the far-field. The question of the existence of peaked spectra is still open (Randall, 1973), and may be solved by paying fuller attention to source finiteness effects on the specified source-time function. In any case, the computation of seismic moment can be made from either the flat level or the peak level (Minster, 1974).

The behavior of intermediate or region II frequencies depends upon the dynamics of the rupture and displacement processes. Some of the parameters which describe these processes may be interrelated by the first law of thermodynamics:

$$E_T = E'_T + E_f = E_Q + E_\gamma + E_f + E_R \quad (5.2)$$

where  $E_T$  is the total energy release,  $E_Q$  is the internal energy change,  $E_f$  is the energy required to accomplish displacement against friction or other energy sinks (plastic flow, shear melting, etc.),  $E'_T$  is the specific surface energy required to fracture the rock (corresponding to Archambeau and Minster's (1976) latent heat of transition), and  $E_R$  is the energy radiated away, which is all we can observe teleseismically.  $E'_T$  is the total energy in the case  $E_f = 0$ .

The partitioning of various energies is best understood if we first work the reverse problem (Randall, 1972; Husseini, preprint). That is, consider an

unbounded, unstressed, uniform linear medium in which we make a cut upon which we force a displacement. If  $u(\xi, t)$  is a complicated function, then the required stresses,  $\sigma(\xi, t)$ , will also be complex, but they will be exactly equivalent to the stress drop obtained by relaxing stress in the usual problem. That is, the applied stress in the reverse problem will be the stress which must be applied to cancel the existing stress to obtain zero (or frictional) stress across the fault.

If the cut completely decouples the two sides over the fault area  $A(t)$ , then the total work done is

$$E_T' = \overline{\sigma_1} \overline{u} da = \int_t \int_{A(t)} \sigma_1(\xi, t) \dot{u}(\xi, t) d\xi dt \quad (5.3)$$

where the overbar indicates an average on both time and space of the form

$$\overline{\sigma} = \frac{1}{AT} \int_t \int_{A(t)} \sigma(\xi, t) d\xi dt \quad (5.4)$$

where  $T$  is the duration of the event. The second form in (5.3) is from Love (1944, p. 93), who argues that we must be concerned with the rate of work before we can integrate to get total work.  $\sigma_1$  is generally defined to be the average stress before nucleation, but in this paper,  $\sigma_1$  will be generalized to be the tectonic stress adjacent to the fault. If friction opposes the motion, we must add  $\overline{\sigma}_f$  to account for heat loss:

$$E_T = \int_A (\overline{\sigma}_1 + \overline{\sigma}_f) \overline{u} da \quad (5.5)$$

We may obtain expressions for  $E_Q$  and  $E_R$  by rewriting (5.2) in terms of kinetic energy  $E_K$  and potential energy  $E_p$ . Following Eshelby (1957),

$$E_Q = 1/2 E_T = 1/2 \int_A (\bar{\sigma}_1 + \bar{\sigma}_f) \bar{u} da \quad (5.6)$$

$$E_R = 1/2 \int_V \rho (\bar{u} \bar{u} - \bar{\bar{u}} \bar{u}) dv \quad (5.7)$$

Now, in the normal problem, the only energy that may be drawn from the medium is  $E_Q$  :

$$E_Q = E_R + E_\gamma + E_f \quad (5.8)$$

Substitution of known quantities gives the available energy after friction as

$$\Delta E = E_Q - E_f = E_R + E_\gamma = 1/2 \int_A (\bar{\sigma}_1 - \bar{\sigma}_f) \bar{u} da \quad (5.9)$$

That is, the energy we see in radiation is some function of  $(\bar{\sigma}_1 - \bar{\sigma}_f)$ , which we will define here as the dynamic stress drop.

There are theoretical (Husseini et al., 1976) and laboratory (Brady, 1974; Johnson and Scholz, 1976) justifications for this partitioning of energy. Since the sum is always controlled by (5.8), we may define efficiencies to relate the various energy forms. For instance,

$$\Delta E = E_Q - E_f = n_f E_Q$$

Where  $n_f = \frac{\bar{\sigma}_1 - \bar{\sigma}_f}{\bar{\sigma}_1 + \bar{\sigma}_f}$  is the frictional efficiency. The partitioning of  $\Delta E$

into  $E_\gamma$  and  $E_R$  is a function of the strength of the rock, with rupture velocity  $v_R$  as a parameter. If  $\Delta E = E_\gamma$ , the rupture proceeds quasistatically

as creep, with no energy for radiation. As the ratio  $\Delta E/E_Y$  increases,  $v_R$  also increases up to the limit of shear wave velocity for antiplane extension or Rayleigh wave velocity for inplane extension. This may be written in terms of the radiation efficiency,  $\eta_R = E_R/\Delta E$ . Though  $\eta_R$  may be estimated (Husseini and Randall, 1976),  $\eta_f$  is unknown and we cannot calculate  $E_Q$  from  $E_R$  unless  $\bar{\sigma}_f = 0$  throughout rupture.

The equivalent seismic moment was defined by Aki (1966) in terms of fault parameters and the moment of one couple of a double-couple point source with the same radiation as a dislocation source (or natural event). Thus  $M_0$  is proportional to  $E_R$  or  $E_Q$  according to

$$E_R = \eta_R \eta_f E_Q \quad (5.10)$$

$$= \eta_R \eta_f A \bar{u} \left[ \frac{\bar{\sigma}_1 + \bar{\sigma}_f}{2} \right] \quad (5.11)$$

$$= \eta_R \frac{M_0}{2\mu} \Delta \bar{\sigma}_0 \quad (5.12)$$

where (5.11) is obtained similarly to (5.5). Note that (5.11) is the standard relation between  $E_s$  or seismic energy and seismic moment (Kanamori and Anderson, 1975), and (5.12) corresponds to Randall's (1972) statement that energy must correspond to stress drop. What Randall failed to see was that his relationship depends upon a different efficiency.

Obviously  $E_Q$  is an independent parameter of rupture, and  $\eta_f$  and either  $\eta_R$  or  $v_R$  are also independent. In keeping with standard practice, we will define  $\eta = \eta_f \eta_R$  as the seismic efficiency, and keep  $\eta$ ,  $v_R(\xi, t)$ , and  $M_0$  as independent parameters.

We must consider the relationship between the various stress parameters.

We have defined the dynamic stress drop  $\Delta\bar{\sigma}_0 = (\bar{\sigma}_1 - \bar{\sigma}_f)$ , which corresponds exactly to Brune's (1970) effective stress. Brune also defined the static stress drop  $\Delta\sigma_s = \langle\sigma_1\rangle - \langle\sigma_2\rangle$  where the brackets indicate spatial averages;  $\langle\sigma_1\rangle$  is average stress prior to nucleation and  $\langle\sigma_2\rangle$  is average stress after static equilibrium is again achieved. To make comparisons easier, we shall remove all averages and consider only behavior at a point on the rupture surface. Then  $\sigma_1(t)$  will be the stress in the medium adjacent to the fault surface at the point of observation; that is,  $\sigma_1(t)$  is the Huyghen's principle superposition of energies radiated from the relaxation of a prestress volume.  $\sigma_1(t)$  starts at the static parameter,  $\sigma_1$ , and decays at a rate governed by the shape and intensity of the prestress, duration and velocity of rupture, elastic constants of the fault zone (or inclusion), constants of the host medium, stress release rate for a given disturbance and the mechanism by which radiated energy from the prestress is converted to displacement and fracture energy at the fault surface.  $\sigma_f(t)$  will be the stress which opposes motion after the failure front passes, and thus will be generalized to include all forms of energy sink during displacement. If a partial melt occurs in the inclusion (fault), then  $\sigma_f(t)$  drops to zero until rupture is arrested, either by geologic constraint or energy deficiency in the prestress. Note that, if a restricting constraint acts, displacement may cease, even though the medium is still radiating energy, and stress may build up again to a value  $\sigma_2 > \sigma_f$  across the fault if motion ceases without exhausting the prestress. At any moment, the stress must drop from  $\sigma_1(t)$  to  $\sigma_f(t)$  as the energy propagates the last increment of distance toward the point of observation. That is,  $\lim_{x \rightarrow 0}(\sigma_1(x)) = \sigma_f(\xi)$  where  $x$  measures distance from the fault. The dynamic stress drop thus represents the energy release as a function of time in the neighborhood of the point of observation.

These relationships are diagrammed in Figure 5.1, where the shapes of the curves are not intended to represent an actual model. Note that an incomplete dynamic stress drop implies an inefficient use of the available energy, while an incomplete static stress drop implies an incomplete use of the energy in the relaxation volume. The stress buildup just before the rupture passes at time  $t_0$  is a universal feature of crack theory (Fossum and Freund, 1975), in which stress has a square root singularity at the crack tip. The singularity results from reducing the crack tip to a point for mathematical simplicity and does not occur in nature. However, we know that fracture energies are quite high, even for pre-existing cracks, so the stress concentration about the tip of the inclusion, as observed by Brady (1974), is a mechanism with which to force the required energies into the crack tip. The drop of stress to zero just after  $t_0$  is also a feature of Brady's observations, and is not postulated by theory. The amount of energy implied is very small, and this feature is not important.

Figure 5.2 schematically shows that the displacement cannot jump concurrently with the stress drop, but must begin at the initial stress drop and increase to a final value over a small but finite time. The initial displacements reflect stored stress energy near the fault, while later displacements represent energy propagating from farther away. In the absence of constraints, the displacement at nucleation would have the greatest value, and the displacement would taper to zero at all static fault edges. Going the other way, the initial stress drop across the fault must happen on a time scale related to rupture propagation, while the time scale of stress equilibrium must be related to particle velocities of the displacement that maintains the dynamic stress drop.

We have demonstrated the complexity of the failure process well enough to show that interpretation of spectral properties in terms of source parameters is difficult at best. We can, however, relate certain parameters to certain

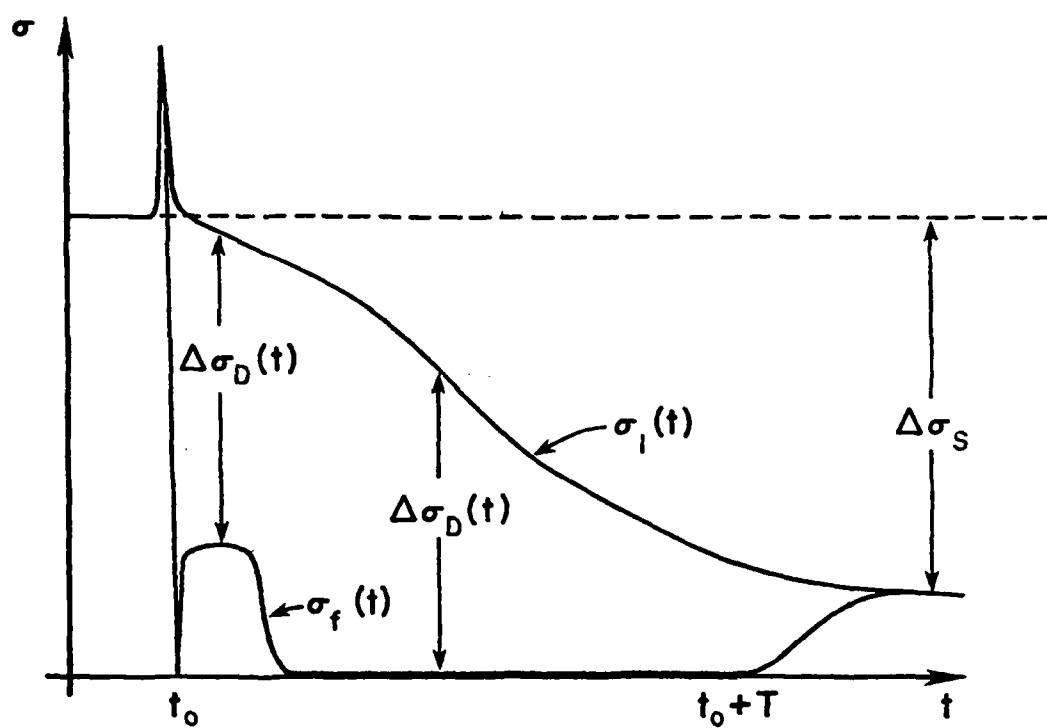


Figure 5.1:

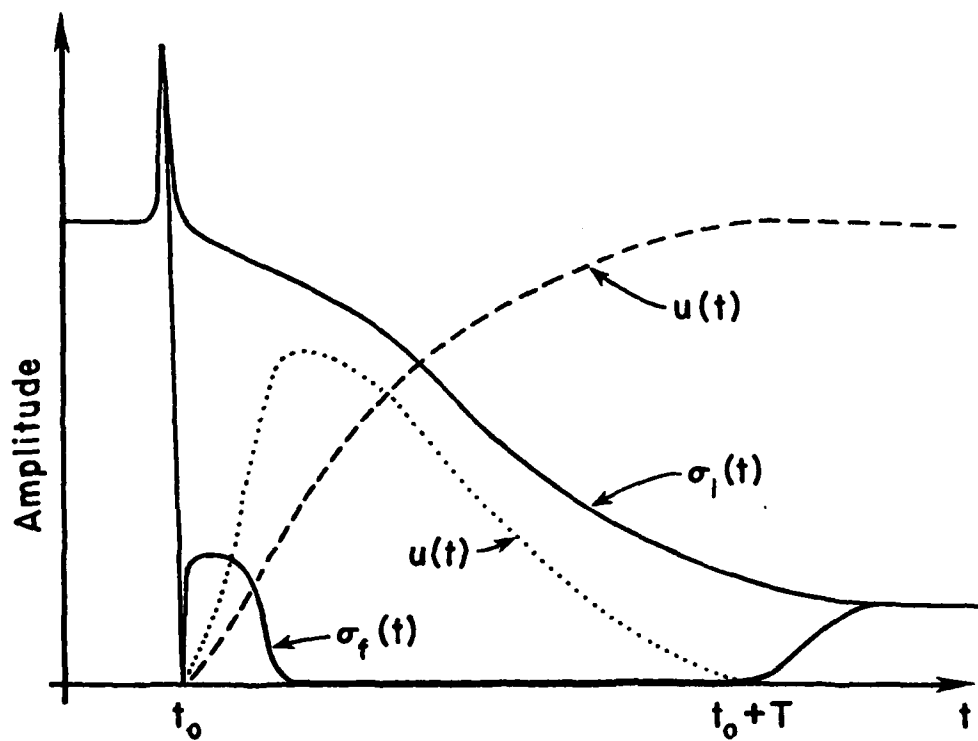


Figure 5.2:

frequency bands. The low frequencies will be controlled by total energy or seismic moment for level and by source finiteness for slope. That is, the longest dimension in the direction of slip will physically control the longest wavelengths efficiently generated. Note that this dimension will correspond to a prestress dimension, rather than to fault length. The intermediate frequencies will be controlled by the dynamics of source propagation and slip, with rupture velocity, increasing source volume with time and dynamic stress drop as particularly important parameters. This time of rapid motions and meeting of constraints on motion is the time when interference of radiation from different parts of the source takes place, generating corner frequencies. The final high frequency decay is determined by the shortest time constant of rupture, which is always less than or equal to the rise time. Undoubtedly irregularities in the stress release or rupture growth (stick-slip) control the final decay rate.

We see also that certain source parameters are not diagnostic of spectral properties. In particular, the static stress drop  $\Delta\sigma_s$  only relates to the endform of a complicated stress history. Likewise the often used average parameters  $A$  and  $\bar{u}$  can be misleading unless the form of the average is understood, and it is not clear that linear averages instead of time dependent integral averages are sufficient.

In terms of a classification scheme for earthquakes according to spectral properties, this study shows that relatively few source parameters may be used. Indeed, it will be far better to achieve a classification based upon the abstract spectra themselves, with emphasis on tools such as the  $\Omega_0 - f_0$  diagram (Hanks and Thatcher, 1972). In particular, attempts to provide baselines and absolute values to source parameters is best left to interpretive discussion, since most parameters relate to a tradeoff between dynamic source properties.

5A. Appendix.

We noted briefly that the high frequency asymptotes of the displacement amplitude spectrum are distorted by anelastic attenuation. In the previous semi-annual report we showed that the distortion could be altered either by changing the T/Q ratio or by applying a frequency-dependent modulation. We demonstrated the effect of a single relaxation phenomenon, and we observed that modeling attenuation with one relaxation peak is probably insufficient. This concept has been amply verified by the work of Liu et al. (1976), who model anelastic attenuation by a broadband spectrum of relaxation peaks. Their model gives constant Q over essentially the entire low frequency range, followed by decreasing  $Q^{-1}$  above a high frequency limit  $\tau_2$ .

We tested two separate models, one given by Liu et al. (LAK), and a modified Solomon (MS) model. The modulation functions are;

$$R_{LAK} = \frac{2}{\pi} \tan^{-1} \left\{ \frac{\omega(\tau_2 - \tau_1)}{1 + \omega^2 \tau_1 \tau_2} \right\}$$

$$R_{MS} = \begin{cases} 1, & \omega \leq 1/\tau \\ \frac{\omega\tau}{1 + (\omega\tau)^2}, & \omega > 1/\tau \end{cases}$$

where the modulator is used in: Total anelastic attenuation ( $\omega$ ) =  $e^{-\frac{\omega T}{2Q_{eff}} R}$ .

Figure 5.A.1 shows the frequency dependence of the models as functions of their respective high frequency parameters. ( $\tau_1$  in the LAK model was kept constant at 2000 sec.) Note that the MS model is smoother than the model previously tested, but not as smooth as the LAK model. The LAK model is not characterized by a tangency point, as is our interpretation of a Solomon

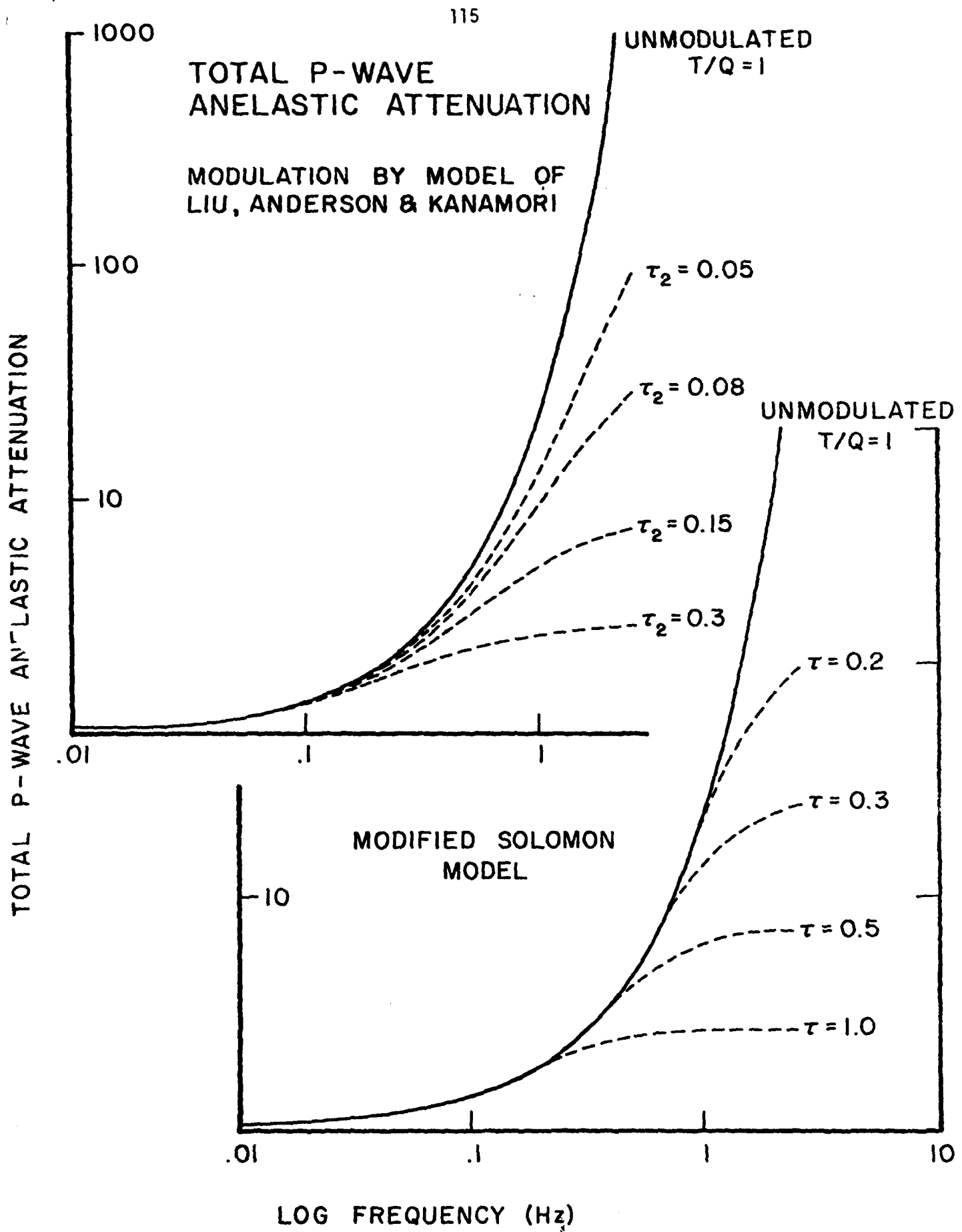
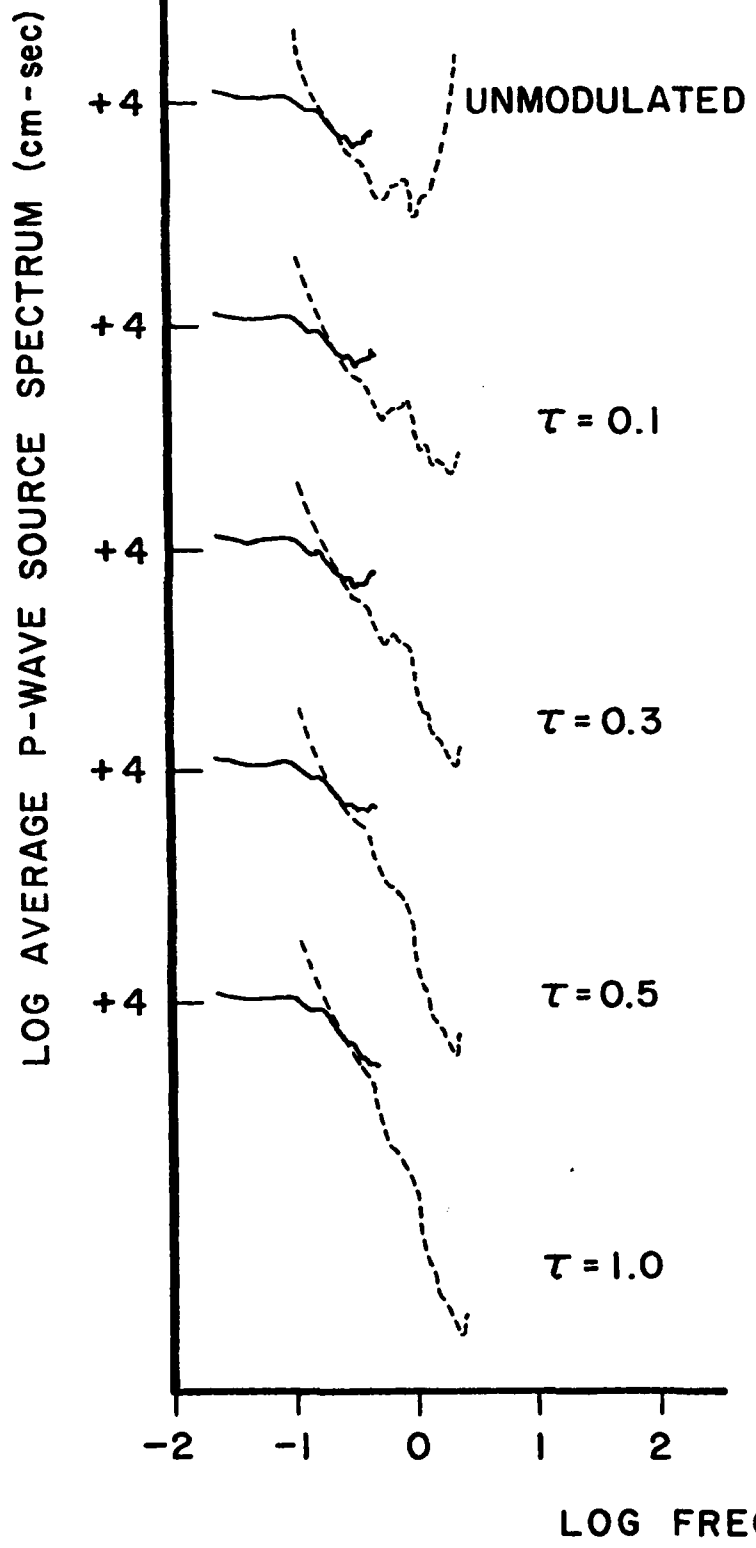


Figure 5A.1: Total P-wave anelastic attenuation. Upper curves from Q model of Liu, Anderson and Kanamori. Lower set represents a modified single relaxation peak model.

model.

The average P-wave source spectrum of the Tien Shan event of February 2, 1969, was processed through attenuation filters of both types. The results are shown in Figure 5.A.2, where approximately equivalent attenuations are paired. Careful examination shows essentially equivalent behavior for both the MS and the smoother LAK model. Thus the corner frequencies "exposed" by this frequency-dependent technique is a property of the spectrum, and not an artifact of the processing. We will stay with the MS model, with  $\tau = 0.3$ . The preference over the LAK model is due to computational simplicity and the better behavior at the highest frequencies.

## MODIFIED SOLOMON MODEL



## LIU, ANDERSON AND KANAMORI MODEL

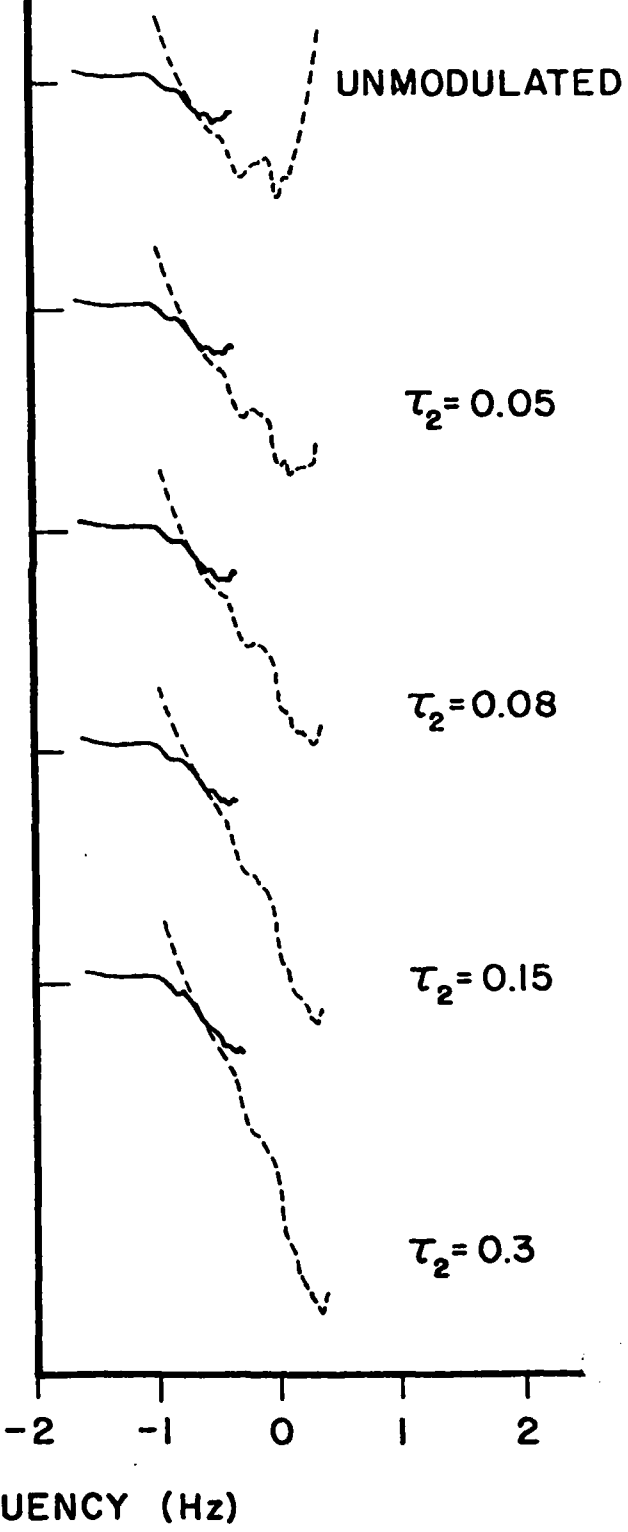


Figure 5A.2: P-wave source spectra for Tien Shan event of February 2, 1969. Upper curves corrected by an unmodulated constant  $T/Q$  anelastic attenuation model. Lower curves corrected by relaxation models with the indicated parameters.

## REFERENCES

Aki, K., Generation and propagation of G waves from the Niigata Earthquake, Bull. Earthq. Res. Inst., Tokyo U., 44, 73-88, 1966.

Aki, K., Sealing Law of Seismic Spectrums, J. Geophys. Res., 72, 1217-1231, 1967.

Archambeau, C. B., and Minster, J. B., Dynamics in prestressed media with moving phase boundaries: A continuum theory of failure in solids, preprint, 1976.

Archambeau, C. B., Developments on Seismic source theory, Rev. Geophys., 13, 304-308, 1975.

Bracewell, R., The Fourier Transform and its Applications, New York: McGraw Hill, 1965, 381 pp.

Brady, B. T., Theory of earthquakes I, A scale independent theory of rock failure, Pure Appl. Geophys., 112, 701-725, 1974.

Brune, J. N., Tectonic stress and the spectra of seismic shear waves from earthquakes, J. Geophys. Res., 75, 4997-5009, 1970.

Burridge, R. and Knopoff, L., Body force equivalents for seismic dislocations, Bull. Seism. Soc. Am., 54, 1875-1888, 1964.

Champeney, D., Fourier Transforms and their Physical Applications, New York: Academic Press, 1973, 256 pp.

Eshelby, J. D., The determination of the elastic field of an ellipsoidal inclusion, Proc. Roy. Soc. Lond. A., 241, 376, 1957.

Fossum, A. F., and Freund, L. B., Nonuniformly moving shear crack model of a shallow focus earthquake mechanism, J. Geophys. Res., 80, 3343-3347, 1975.

Hanks, T. C., and Thatcher, W., A graphical representation of seismic source parameters, J. Geophys. Res., 77, 4393-4405, 1972.

Haskell, N., Total energy and energy spectral density of elastic wave radiation from propagating faults, Bull. Seism. Soc. Am., 54, 1811-1842, 1964.

Husseini, M. I., Jovanovich, D. B., Randall, M. J. and Freund, L. B., The  
Fracture energy of earthquakes, Geophys. J. Roy. Astr. Soc., 43, 367-385, 1976.

Husseini, M. I., and Randall, M. J., Rupture velocity and radiation efficiency  
preprint, 1976a.

Johnson, T. L., and Scholz, C. H., Dynamic properties of stick-slip friction  
of rock, J. Geophys. Res., 81, 881-888, 1976.

Kanamori, H., and Anderson, D. L., Theoretical Basis of some empirical relations  
in seismology, Bull. Seism. Soc. Am., 65, 1073-1095, 1975.

Liu, H. P., Anderson, D. L., and Kanamori, H., Velocity dispersion due to  
anelastivity; Implication for seismology and mantle composition, personal  
communication, 1976.

Love, A. E. H., The Mathematical Theory of Elasticity, Dover 1944.

Minster, J. B., Elastodynamics of Failure in a Continuum, PhD. Thesis,  
California Institute of Technology, 1974.

Randall, M. J., The spectral theory of seismic sources, Bull. Seism. Soc. Am.,  
63, 1133-1144, 1973.

Randall, M. J., Stress drop and the ratio of seismic energy to moment, J. Geophys.  
Res., 77, 969-970, 1972.

Savage, J. C., Relation of corner frequency to fault dimensions, J. Geophys.  
Res., 77, 3788-3795, 1972.

Solomon, S. C., Seismic Wave Attenuation and the State of the Upper Mantle,  
PhD. Thesis, Massachusetts Institute of Technology, 1971.